Ion Doped Metal Oxide and its Power Conversion Efficiency Influence on Perovskite Solar Cells

Dwayne Jensen Reddy

20416564

A dissertation submitted to

Durban University of Technology,

Faculty of Applied Sciences,

in fulfilment of the requirements for the degree of

Doctor of Applied Sciences

Supervisor: Professor Ian Lazarus

Department of Physics,

Durban University of Technology

February 2024

I, Dwayne Jensen Reddy , declare that:

(i) The research reported in this dissertation, except where otherwise indicated, is my original research.

(ii) This dissertation has not been submitted for any degree or examination at any other university.

(iii) This dissertation does not contain other persons' data, pictures, graphs or other information, unless specifically acknowledged as being sourced from other persons.

(iv) This dissertation does not contain other persons' writing, unless specifically acknowledged as being sourced from other researchers. Where other written sources have been quoted, then:

a) their words have been re-written but the general information attributed to them has been referenced:

b) where their exact words have been used, their writing has been placed inside quotation marks, and referenced.

(v) This dissertation does not contain text, graphics or tables copied and pasted from the Internet, unless specifically acknowledged, and the source being detailed in the dissertation/thesis and in the References sections.

Candidate: Dwayne Jensen Reddy

Signature: _____

As the candidate's supervisor I agree to the submission of this dissertation for examination.

Supervisor: Professor Ian Lazarus

Signature: _____

ABSTRACT

Ion Doped Metal Oxide and its Influence on the Power Conversion Efficiency of Perovskite Solar Cells

Dwayne Jensen Reddy
Doctor of Applied Sciences

This study focuses on the fabrication and characterization of Zinc-doped Titanium dioxide (Zn-TiO_2) as an Electron Transport Layer (ETL) in $CH_3NH_3PbI_3$-based perovskite solar cells (PSCs). A one-step spin coating technique under controlled ambient conditions (relative humidity < 65%, room temperature $\sim 20^oC$) for the development of PSC was applied to investigate the effects of Zn-ion doping on the structural, morphological, optical, and photovoltaic properties. Numerical simulations using SCAPS 1D were additionally performed to further investigate the influence of ion doping on the power conversion efficiency (PCE) of PSCs.

Zn-doped TiO_2 was successfully incorporated into the TiO_2 crystal structure using the sol-gel technique. Characterization through X-ray diffraction (XRD) and Energy Dispersive X-ray Spectroscopy (EDX) confirmed the incorporation of Zn ions. The crystallite size ranged from 19.99 to 7.1 nm, depending on the Zn ion doping concentration. XRD results also indicate the formation of a highly crystalline tetragonal perovskite ($CH_3NH_3PbI_3$) phase. Fourier Transform Infrared (FTIR) spectroscopy verified the presence of the anatase phase of Zn-doped TiO_2, while the formation of the adduct of Pb_2 with dimethyl sulfoxide (DMSO) and methylammonium iodide (MAI) was confirmed at 1015 cm^{-1}. Scanning Electron Microscope (SEM) images exhibited fairly smooth and uniform surface coverage for the Zn-doped TiO_2 layers. The Root Mean Square (R_q) values for surface roughness showed a decrease from 26.85 nm for undoped TiO_2 to 23.4 nm for the 5 mol% Zn-doped TiO_2 layer. UV-Vis spectroscopy demonstrated low light transmission loss characteristics from 300 to 790 nm, with the 2 mol% Zn-doped TiO_2 showing slightly improved light transmission between 550 and 800 nm. The bandgap energy of undoped and Zn-doped TiO_2 ranged from 3.53 to 3.38 eV, while the perovskite layer exhibited a bandgap energy of 2.06 eV.

Experimentally, an optimum PCE of 5.67% was achieved with a 2 mol% dopant concentration. However, increasing the Zn dopant to 5 mol% led to a slight deterioration in the PCE. Numerical simulations revealed that increasing the donor doping concentration in the ETL improved the conduction band alignment at the ETL and perovskite interface, resulting in a PCE of 6.17%. Optimizing the absorber acceptor doping concentration and band gap improved the PCE to 10.79%, however, created a pronounced conduction band offset at the ETL/perovskite interface. This was mitigated by introducing an interfacial layer of Cubic Silicon Carbide (3C-SiC) between the absorber and ETL to minimize the conduction band offset, ultimately achieving a PCE of 12.09%.

Keywords: Perovskite, Titanium dioxide, Zinc ions, Doping, Power Conversion Efficiency

List of Abbreviations

1. Acceptor doping density (N_d)
2. Aluminum oxide (AlO_3)
3. Aluminium Zinc Oxide (AZO)
4. Bandgap (E_g)
5. Bromide (Br_3)
6. Chloride (Cl_3)
7. Conduction Band (CB)
8. Conduction Band Offset (CBO)
9. Conduction Band Minimum (CBM)
10. Cubic Silicon Carbide (3C-SiC)
11. Dark saturation current ((I_o)
12. Diffusion current (I_{dif})
13. Dimethylformamide (DMF)
14. Dimethyl-sulfoxide (DMSO)
15. Diode saturation current (I_D)
16. Donor doping density (N_d)
17. Drift current (I_{dr})
18. Dye-Sensitized Solar Cells (DSSCs)
19. Electron Transport Layer (ETL)
20. Electron Transport Material (ETM)
21. Energy-Dispersive X-Ray Spectroscopy (EDX)
22. Fill Factor (FF)
23. Fluorine Doped Tin Oxide (FTO)
24. Fourier Transform Infrared Spectroscopy (FTIR)
25. Gallium Arsenide (GaAs)
26. Highest Occupied Molecular Orbital (HOMO)
27. Hydrochloric Acid (HCL)
28. Hole Transport Layer (HTL)
29. Hole Transport Material (HTM)
30. Indium Oxide (In_2O_3)
31. Indium (III) Sulfide (In_2S_3)
32. Initial Energy State (E_i)
33. Iodide (I_3)
34. Fermi Energy Level (E_{fn})
35. Flat band potential (V_{FB})
36. Final Energy State (E_h)
37. Formamidinium (FA)
38. Lithium Bis (LiTFSI)
39. Lowest unoccupied molecular orbital (LUMO)
40. Methyl Ammonium Lead Iodide ($CH_3NH_3PbI_3$)

41. Methyl Ammonium Lead Iodide ($MAPbI_3$)
42. Methyl Ammonium Lead Bromide ($MAPbBr_3$)
43. Methyl Ammonium (MA)
44. Methyl Ammonium Iodide (MAI)
45. Open-Circuit Voltage (V_{OC})
46. Perovskite Solar Cells (PSCs)
47. Photoluminescence (PL)
48. Photovoltaic (PV)
49. Photon energy (E_{ph})
50. Power Conversion Efficiency (PCE)
51. Scanning Electron Microscopy (SEM)
52. Series Resistance (R_s)
53. Shunt Resistance (R_{sh})
54. Short-Circuit Current Density (J_{SC})
55. Short-Circuit Current (I_{SC})
56. Tin Oxide (SnO_2)
57. Titanium Dioxide (TiO_2)
58. Titanium Isopropoxide (TTIP)
59. Transparent Conductive Oxide (TCO)
60. Transparent Conductive Materials (TCMs)
61. Transmission Electron Microscope (TEM)
62. Ultra Violet Ozone (UVO)
63. UV-Visible Spectroscopy (UV-Vis)
64. Valence Band (VB)
65. Valence Band Maximum (VBM)
66. X-Ray Diffraction (XRD)
67. Zinc-doped Titanium Dioxide (Zn-TiO_2)
68. Zinc Chloride ($ZnCl_2$)
69. Zinc Oxide (ZnO)
70. Zinc Sulfide (ZnS)
71. 4-Tert-Butylpryridine (TBP)

PUBLICATIONS ARISING

Ion Doped Metal Oxide and its Influence on the Power Conversion Efficiency of Perovskite Solar Cells

Dwayne Jensen Reddy
Doctor of Applied Sciences

Publication

1. D. J. Reddy, I.J. Lazarus, 'Fabrication and Characterization of Methyl Ammonium Lead Iodide based Perovskite Solar Cells under Ambient Conditions', Indonesian Journal of Electrical Engineering and Computer Science
2. D. J. Reddy, I.J. Lazarus, 'Effects of Zn doped TiO_2 on the Performance of Perovskite Solar Cells', International Journal of Electrical Engineering and Applied Sciences

Publication under preparation

1. Performance enhancement of experimentally developed Zn doped TiO_2 as the electron transport layer in Perovskite Solar Cells using SCAPS 1D

Presentation

1. Fabrication and Characterization of Methyl Ammonium Lead Iodide based Perovskite Solar Cells under Ambient Conditions, 2021, Durban University of Technology 2021
2. Ion doped metal oxide and its influence on the Power Conversion Efficiency of Perovskite Solar Cells, 2022, South African Technology Network, Durban Elangeni Hotel, South Africa
3. Zinc doped TiO_2 and its effect on the Power Conversion Efficiency of Perovskite Solar Cells, 2022, Durban University of Technology 2022

ACKNOWLEDGMENTS

In no particular order, I wish to express my sincere gratitude to the following who enabled this document to be completed successfully:

- The South African National Research Thuthuka Funding (NRF) and Eskom Tertiary Education Support Programme (TESP) Funding for all the support in purchasing equipment, consumables, and characterization testing required for this research.
- Professor Ian Lazarus and the South African Technology Network (SATN) for their mentorship, support, and encouragement throughout this research.
- The Durban University of Technology, Faculty of Engineering and Applied Science staff, whose commitment to excellence and dedication to pursuing knowledge created an inspiring academic environment.
- Laboratory staff at the Engineering and Applied Sciences Laboratory at the Durban University of Technology for their assistance in performing FTIR and UV-Vis characterization.
- Professor Moodley, and his team at the University of Kwa-Zulu Natal (UKZN) for assistance with photoluminescence characterization
- The Council for Scientific and Industrial Research and Dr Motaung for assistance with XRD characterization.
- I would like to express my deepest gratitude to my family and friends, whose unwavering love, support, and encouragement have been the cornerstone of my journey towards pursuing a Doctorate degree. Their belief in me and constant presence during this challenging yet rewarding endeavor have made all the difference.

Contents

List of Figures

List of Tables

Chapter 1

INTRODUCTION

This thesis studies the role of metal oxide electron-transporting material properties in perovskite solar cells. The central research question is how ion doping of metal oxide semiconductors influences the power conversion efficiency of perovskite solar cells. This chapter provides the context, thesis chapter outline, aims, objectives, justification, and hypotheses

1.1 Background

The introduction that follows describes pertinent background information that gives the research perspective. This study focuses on designing, synthesizing, and studying novel materials with potential uses in recent development of perovskite solar cells.

The current state of energy generation is still highly dependent on fossil fuels and nuclear energy, which supplies/contributes to nearly 45.2% of the total global energy usage according to the

latest distribution of global energy generation [1]. The carbon dioxide and greenhouse gases emitted using this technology play's a significant role in climate change, and many reported premature deaths [2]. Furthermore, fossil fuel sources are available in limited supply and are expected to deplete within the next 100 years [3]. Nuclear energy is an unappealing choice due to the generation of radioactive waste and the long-term storage of this waste which remains dangerous to human health for thousands of years [4].

Renewable energy generation (solar, wind, biomass, hydropower, and geothermal) contributes only 27.2% of the total global energy usage [1]. The installed renewable energy capacity increased from 754 GW in 2000 to 2799 GW in 2020 [5, 6]. Solar photovoltaic has exhibited the fastest growth rate due to the huge solar source of solar energy (i.e., the sun), with nearly 885 million TWh available annually, compared to the annual energy consumption of 176 TWh in 2021, which is enough to exceed the global energy requirements for years to come [7]. Due to an increased population, urbanization, and the fourth industrial revolution, energy consumption is expected to increase to 327 TWh by 2050 [7]. Although the cost of energy generated by solar cells has reduced since its inception nearly forty years ago, it still remains significantly more expensive than energy generated by fossil fuels [8]. This is primarily due to the high manufacturing costs which require high vacuum and high temperature processes which require high energy consumption for production [9].

As the world transitions to more sustainable forms of energy generation, the development of more efficient and cost-effective semiconductor materials has become increasingly important. Perovskite solar cells (PSC) have attracted much interest recently due to their low production costs and high efficiency. PSCs can be fabricated using low-temperature solution processing techniques and have unique properties such as high light absorption coefficient, long charge diffusion lengths, mechanical flexibility, and lightweight [10]. This allows for further applications on building facades

and curve surfaces in urban areas with limited space for onsite energy generation. Additionally, PSCs have tunable bandgaps, enabling them to be integrated with other solar technologies to develop tandem cells and reach efficiencies beyond the Shockley Quiseer limit (30% at 1.1 eV) [11]. PSCs are crucial in developing photovoltaic (PV) technology and reducing carbon dioxide emissions. However, challenges regarding lifetime, stability, and efficiency remain the impediments to commercialization.

1.2 Research Question

The central research question is based on how ion doping of metal oxide semiconductors influence the Power Conversion Efficiency (PCE) of Perovskite Solar Cells.

1.3 Hypothesis

It is hypothesized that doping TiO_2 using varying molar percentages of Zn ions will introduce new bandgap states into the TiO_2 lattice structure, improving the ETL layer's fundamental properties and the overall PCE of Perovskite Solar Cells.

1.4 Justification

Due to their polycrystalline or semi-crystalline structure, ETL materials have restricted electron-transporting properties (electron mobility and conductivity). Notably, the electrical characteristics

of TiO_2 ETL materials fabricated at temperatures below 550°C have poorer electrical properties. In this context, it becomes necessary to incorporate dopants into the TiO_2 lattice structure to match the electrical properties of hybrid organic–inorganic perovskite absorber materials to improve the PSC performance.

1.5 Aim of the Thesis

The research aims to assess the potential to improve the power conversion efficiency of the perovskite solar cell by doping TiO_2 with Zn ions at molar concentration percentages of 0.5%, 1%, 2%, and 5%.

1.6 Objectives of the Thesis

- To develop each layer of the perovskite solar cell using affordable and simple processing techniques.
- To synthesize TiO_2 and Zn-doped TiO_2 nanoparticles using sol-gel chemistry.
- To characterize (SEM, XRD, EDX, TEM, FTIR, Photoluminescence, and UV-Vis) the TiO_2 and Zn-doped TiO_2 electron transport layer of the PSC to explore the morphological, structural, and optical properties.
- To determine the experimental performance characteristics of the TiO_2 and Zn-doped TiO_2 PSCs developed.

- To develop a reference model on SCAPS 1D using experimentally obtained data for numerical analysis into the influence of ion doping of the electron transport layer.

1.7 Contributions

The contributions in this thesis can be highlighted as follows:

- Ion doping of the electron transport layer in Perovskite Solar Cells is critical in improving fundamental material properties and minimizing the conduction band offset at the ETL/ Perovskite interface to improve the PCE.
- A numerical analysis guide is proposed to enhance the Power Conversion Efficiency of experimentally developed Perovskite Solar Cell.
- The developed and simulated Perovskite Solar Cell provides a clear understanding of the limitations and performance enhancement methods for implementation in various Perovskite Solar Cell architectures.

1.8 Scope of Study

In this study, the electron transport layer was limited to 0.22 M titanium dioxide with a Zn ion doping molar percentage of 0, 0.5, 1, 2, 5. The perovskite absorber layer was based on methylammonium lead iodide's organic-inorganic metal halide composition.

1.9 Thesis Structure

The thesis is structured as follows:

Chapter 2 initiates a concise literature review, delving into the core concepts of semiconductors and the fundamental principles of solar cells.

Chapter 3 explores the architecture of Perovskite Solar Cells (PSC), elaborating on the unique properties of the materials employed in constructing these devices.

Chapter 4 encompasses the methodologies used in this thesis, including the fabrication process, experimental and numerical characterization techniques. The impact of Zn-doping on the morphological and structural properties of TiO_2 is examined through electron microscopy (SEM, TEM) and X-ray diffraction. Meanwhile, the optical properties of Zn-doped TiO_2 are investigated using UV-Vis and photoluminescence. Additionally, FTIR analysis is employed to identify the functional groups within the methyl ammonium lead iodide-based perovskite layer and the anatase phase of Zn-doped TiO_2. To quantify the elemental composition of each layer, EDX spectroscopy is employed.

Chapters 5 and 6 discusses and analyses the experimental and simulation results.

Finally, Chapter 7 provides the conclusion of the thesis, along with recommendations that have arisen from the research conducted.

Chapter 2

SEMICONDUCTOR and SOLAR CELL THEORY

This chapter provides a concise overview of semiconductor properties, particularly the band gap, and its significance in solar cells. It discusses the role of semiconductors in solar cells, explaining the absorption of photons and the creation of electron-hole pairs. The Shockley-Queisser limit is introduced as a benchmark for solar cell efficiency. The fundamentals of solar cells, including charge generation, separation, and recombination losses, are discussed. The chapter also covers semiconductor hetero-junctions and presents an equivalent circuit model for solar cells. Finally, it explores photovoltaic parameters such as current-voltage characteristics, short-circuit current density, open-circuit voltage, fill factor, and power conversion efficiency.

2.1 Semiconductor

The band gap of a semiconductor shown in Figure 2.1 is a fundamental property that determines its electronic conductivity and usefulness in electronic devices. It refers to the energy difference between the highest occupied molecular orbital (HOMO) energy level, termed the valence band (VB), and the lowest unoccupied molecular orbital (LUMO) energy level, termed the conduction band (CB), in the semiconductor material. When the valence band is full of electrons, they cannot contribute towards conduction unless they absorb enough energy to overcome the material's bandgap and get excited into the conduction band. The CB and VB in conductors overlap, meaning they have no bandgap, thus allowing electrons to move freely through the material to conduct. This is because conductors have a large number of free electrons that are not confined to specific energy levels or bands within the material. The Fermi level is the energy level at which the probability of finding an electron lies within this continuum of energy levels. The large number of free electrons in conductors means that the Fermi level is typically very close to the conduction band, making it easy for electrons to move through the material and conduct electricity [12–14]. For insulators, the large bandgap prevents electrons from being excited from the VB to CB. The valence band is completely filled with electrons, while the conduction band is completely empty. The energy required to excite an electron from the valence band to the conduction band is very high due to the large band gap. As a result, insulators do not conduct electricity under normal conditions [15, 16].

Semiconductor material, however, has a small band gap, implying that electrons can be excited from the VB to CB. When a photon of energy greater than the band gap is absorbed by a semiconductor, it can excite an electron from the valence band to the conduction band, creating an electron-hole pair. The photon's energy must be greater than the band gap because the electron needs to overcome the energy difference between the two bands. The absorption of photons by a semiconductor is an essential property of solar cells. A semiconductor with a small band gap is

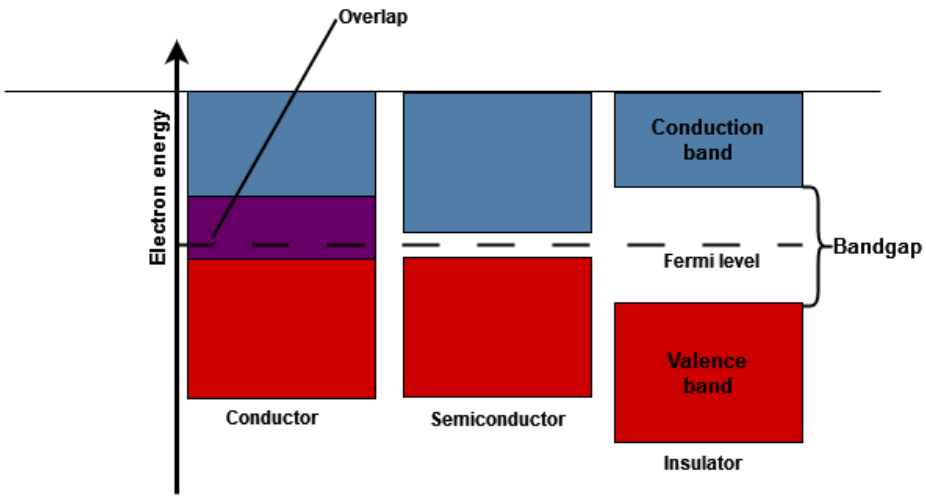

Figure 2.1 Band structure of metal, semiconductor, insulator

more effective at absorbing photons with lower energies, such as those in the infrared region of the spectrum. In contrast, a semiconductor with a more significant band gap is more effective at absorbing higher energy photons, such as those in the visible and ultraviolet regions of the spectrum. William Shockley and Hans-Joachim Quiesser determined that at a wavelength of 925 nm corresponding to the ideal bandgap of 1.34 eV shown in Figure 2.2 can convert 33.7% of the sun's energy into electricity [17].

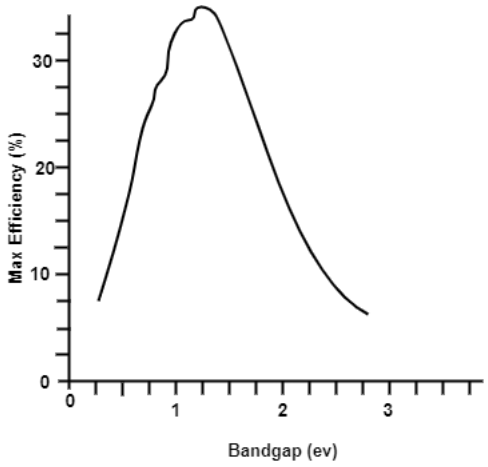

Figure 2.2 The Shockley-Queisser limit for the efficiency of a solar cell [18]

2.2 Fundamentals of Solar Cells

A solar cell, also known as a photovoltaic cell, is an energy conversion device that generates charge carriers by absorbing the incoming photons from sunlight. For electrons to be emitted from a semiconductor material, the incoming photon energy (E_{ph}) must be higher than the material's bandgap (E_g) energy [19]. The photon energy is given in Equation (2.1).

$$E = \frac{hc}{\lambda} \tag{2.1}$$

Where:

h stands for Plank's constant (h = 6.626 x 10^{-34}Js),

c for the speed of light within a vacuum (c = 3 x 10^{8} m/s), and

λ is the wavelength of the photon [20].

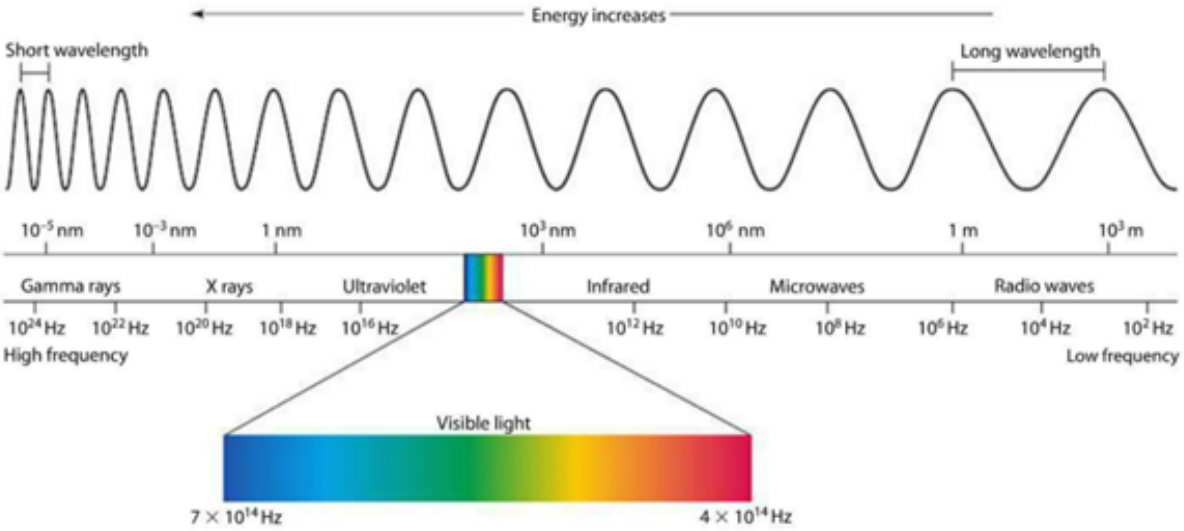

Figure 2.3 The electromagnetic spectrum illustrating photon energy increase with decreasing wavelength [21]

The electromagnetic spectrum shown in Figure 2.3 encompasses a broad range of frequencies

and wavelengths, ranging from gamma rays with very high frequencies and short wavelengths to radio waves with very low frequencies and long wavelengths. Solar cells are designed to convert a specific part of the electromagnetic spectrum, known as the visible light spectrum, into electricity. This part of the electromagnetic spectrum includes all the rainbow colors and has wavelengths ranging from about 400 nm (violet) to 700 nm (red).

2.2.1 Charge Generation

Charge generation in photovoltaics occurs when electrons in the valence band of a semiconductor absorb the energy of the photons and are excited from their initial energy state (E_i) into their final energy state (E_h) in the conduction band, as shown in Figure 2.4. A void is created in the valence band when electrons are excited from E_i to E_h; this void is referred to as a hole. Hence, electron-hole pairs are generated by photon absorption in the semiconductor material when $E_{ph}>E_g$.

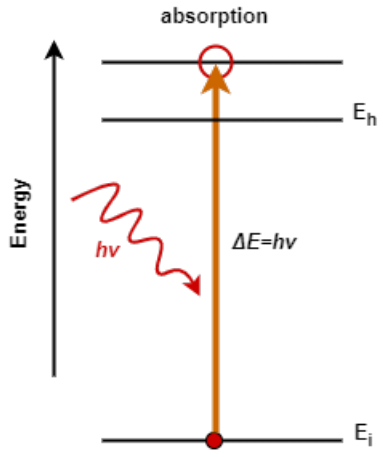

Figure 2.4 Absorption of photon energy

2.2.2 Charge Separation

A p-n junction is used in photovoltaics to separate charges. When a p-type and an n-type semiconductor join, a p-n junction is formed. Because the n-type material has a higher electron concentration and the p-type material has a higher hole concentration, electrons diffuse from the n-side to the p-side. Holes diffuse from the p-type side to the n-type side, as shown in Figure 2.5(a), resulting in a diffusion current I_{dif} [22–26]. As a result of this diffusion, the p-side of the junction becomes negatively charged, and the n-side becomes positively charged, resulting in a 'built-in' voltage. The built-in voltage causes holes on the n-side to migrate to the p-side and electrons on the p-side to migrate to the n-side, resulting in charge separation and drift current I_{dr}. Because any charge carriers present are quickly swept away, the region is known as a depletion region. The diffusion and drift currents have the same amplitude in opposite directions at equilibrium, and the dark saturation current I_0 is equal, as illustrated in Figure 2.5(b). $I_{dif} = I_{dr} = I_0$

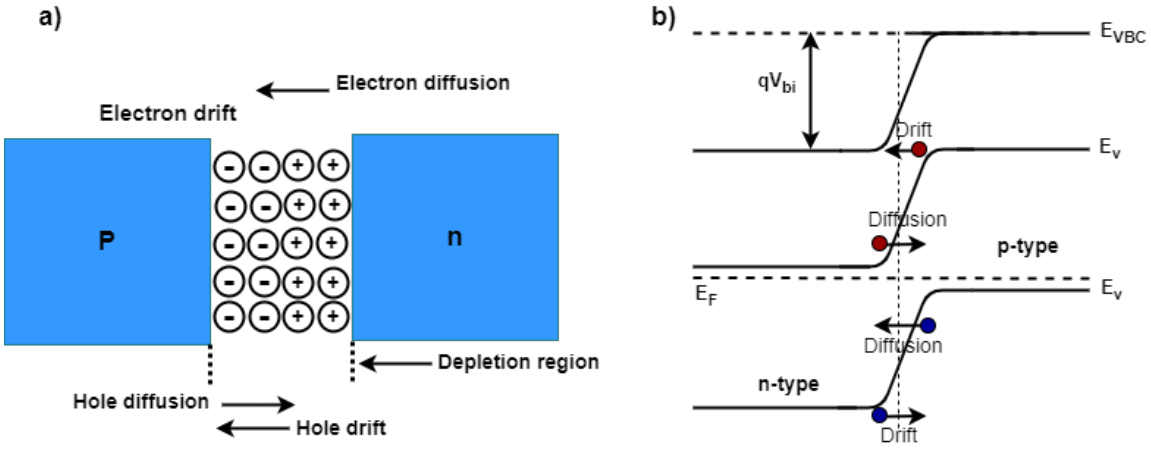

Figure 2.5 p-n junction formation process [27]

The solar cell efficiency is dependent on a number of factors, including the quality of the semiconductor material fabricated, the p-n junction design, and the film thickness of each layer of the cell. The semiconductor absorber material must have a bandgap that allows for the broad

absorption of the electromagnetic spectrum, and the p-n junction must be designed to maximize the separation of charges and minimize the recombination of electron-hole pairs [28, 29].

2.2.3 Recombination Loss

In a solar cell, an incident photon produces an electron-hole pair known as charge carriers. These newly formed charge carriers must first separate before recombining and emitting energy. This recombination of charge carriers in a solar cell results in the loss of photon-generated carriers, which reduces the solar cell's power conversion efficiency. As carriers are created in different regions of a solar cell, recombination occurs at distinct locations.

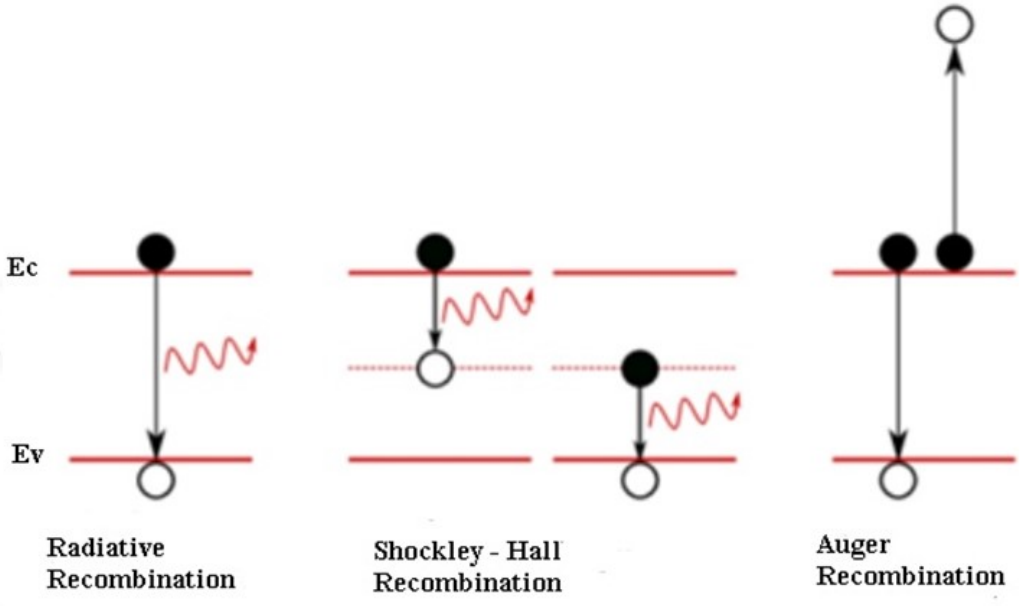

Figure 2.6 Types of recombination in solar cells [30]

Carriers formed in the depletion zone are separated by the depletion region's electric field whereas carriers generated at the front, bulk, and far end of the solar cell have a low chance of separation. Thus, carriers created in these locations will recombine with absorbed energy emission

and will not contribute to the photovoltaic process. The three significant types of recombination losses are shown in Figure 2.6 [31]:

- Radiative (band to band) recombination, this occurs when an electron from the conduction band combines with a hole in the valence band and emits a photon
- Auger recombination, occurs at high charge carrier concentrations caused by excessive doping limiting the electron-hole pair lifetime and efficiency
- Defect assisted recombination, previously referred to as the Shockley-Read-Hall recombination. This type of recombination occurs when an electron or hole gets trapped in an energy state in the forbidden region due to defects in the crystal lattice.

2.2.4 Semiconductor Hetero-junctions in Solar Cells

The p-n junction formed with the same semiconductor material is referred to as homo-junction. Additionally the p-n junction formed with different semiconductor materials with different bandgaps is referred to as a hetero-junction. The properties of semiconductor hetero-junctions are determined by the band alignment at the interface between the two semiconductors. Hetero-junctions can be classified into two types depending on the band alignment at the interface between the two semiconductors: type-I and type-II, as shown in Figure 2.7.

In type-I hetero-junctions, the conduction band minimum (CBM) and valence band maximum (VBM) of both semiconductors are aligned at the interface. This causes electrons and holes to be confined to the same region, resulting in high charge carrier concentrations and recombination. In type-II hetero-junctions, the CBM and VBM of the two semiconductors are staggered, resulting

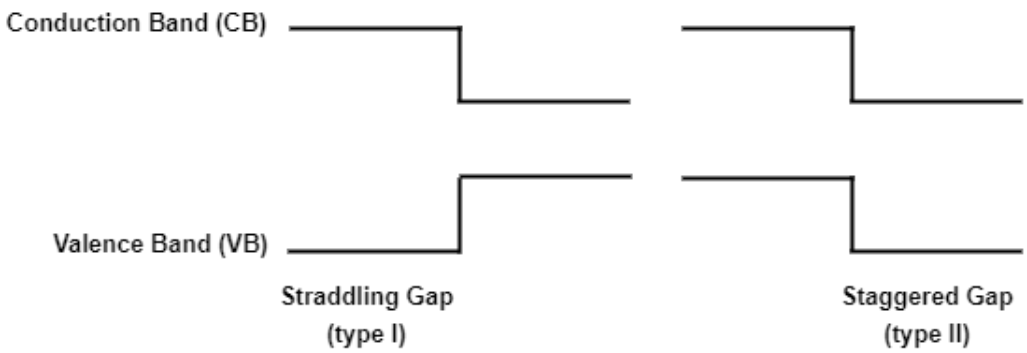

Figure 2.7 Type 1 and 2 hetero-junctions [32]

in a spatial separation of electrons and holes across the interface leading to a longer charge carrier lifetime and lower recombination rates [33].

At the interface of a type-II hetero-junction, photo-generated electrons and holes are spatially separated due to the staggered band alignment. Electrons are confined to the conduction band of one semiconductor, while holes are confined to the valence band of the other semiconductor. This separation results in a longer carrier lifetime and lower recombination rates, which can significantly improve the power conversion efficiency of solar cells [32, 33].

2.3 The Equivalent Circuit Model

The equivalent circuit of a solar cell shown in Figure 2.8 can be modeled as a current source in parallel with a diode and a resistor (R_{sh}), connected in series with another resistor (R_s).

The photocurrent (I_{sc}) represents the current generated by the solar cell due to light absorption. It is represented as a current source in the equivalent circuit and is proportional to the intensity of the incident light. The diode saturation current (I_d) represents the current that flows through

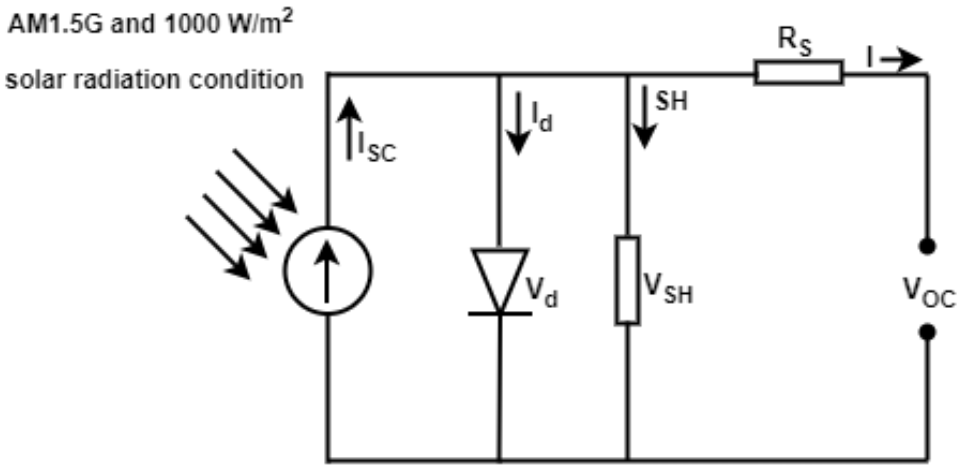

Figure 2.8 A single diode model demonstrating the origin of PV parameters [34]

the diode when it is reverse-biased and measures the recombination losses in the device [35, 36]. The series resistance (R_s) represents the electrical resistance of the metal contacts, the device's material, and the internal connections of the solar cell. The shunt resistance (R_{sh}) is represented as a resistor in parallel with the diode, I_{SH} refers to the leakage current that flows through the solar cell due to defects or non-uniformities in the material [37, 38]. An ideal diode's series resistance is zero, and the shunt resistance is infinitely high around a few MΩ. Equation (2.2) represents the net current output [39].

$$\mathrm{I} = \mathrm{I}_{sc} - \mathrm{I}_{\mathrm{o}} \left\{ e^{\left(\frac{q(V_{oc}+IR_s)}{aKT} \right)} - 1 \right\} - \frac{V_{oc} + IR_s}{R_{SH}} \tag{2.2}$$

Where

I_o = dark saturation current or diode leakage current when there is no light

I_{sc}= short circuit current

q = electronic charge (1.6 x 10^{-19} C)

V_{oc} = open circuit voltage

K = Boltzmann's constant = 1.38 x 10^{-23}J/K

T = temperature in Kelvin

a = diode quality factor

2.4 Photovoltaic Parameters

The current-voltage (I-V) scan shown in Figure 2.9 is widely used to assess how well a solar cell performs. This is performed under illumination, where the voltage is scanned while the current response is recorded. The fundamental parameters that govern the PCE of a solar cell are the open circuit voltage, short circuit current density, and fill factor.

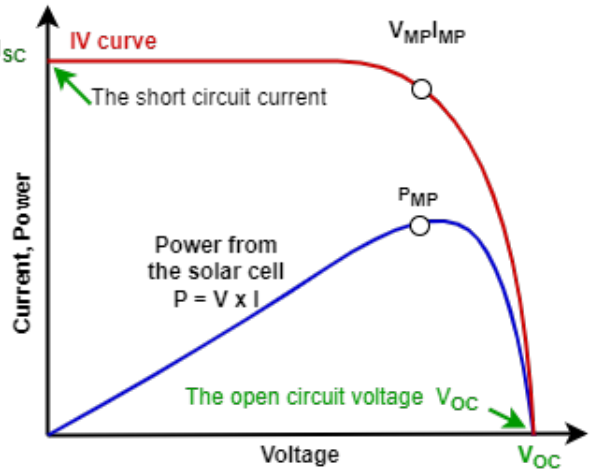

Figure 2.9 The I-V and power characteristic curve of a solar cell [55]

The short circuit current density (J_{SC}) is the maximum current a device can produce when short-circuited in the dark or under the illumination of 1000 W/m^2. The J_{SC} is measured in units of A/m^2 or mA/ cm^2. At J_{SC}, the voltage across the device will be zero. Short-circuit currents occur due to the generation and collection of light-generated carriers. It is primarily determined by the number

of incident photons, as well as its spectrum, optical characteristics, collection probability, and solar cell area. The open circuit voltage refers to the maximum voltage the solar cell develops when no load is connected. This primarily depends on the energy difference between the conduction band of the ETL and the valence band of the HTL. This open circuit or applied voltage cancels out the cell's built-in voltage, preventing the extraction of charge carriers from the device. The fill factor (FF) of a solar cell describes the ability of the device to convert the incident light into electrical power. The fill factor is the ratio of the maximum power that can be extracted from the solar cell to the product of the open circuit voltage (V_{OC}) and the short circuit current density (J_{SC}). A high fill factor indicates that the solar cell operates efficiently and can convert a large portion of the incident light into usable electrical power. In contrast, a low fill factor suggests that the solar cell is not operating efficiently and is wasting a significant portion of the incident light. The FF is also dependent on the series and shunt resistances of the device; a low series and high shunt resistance are required to minimize energy losses and maximize the device's power output [40].

A solar cell's power conversion efficiency (PCE) is a measure of its ability to convert incident light into usable electrical power. It is defined as the ratio of the electrical power output of the solar cell to the incident optical power of the incoming light and is typically expressed as a percentage. The PCE of a solar cell depends on several factors, including the efficiency of the light absorption, charge separation, and charge collection processes within the device. It can be calculated using the following equation:

$$\mathrm{PCE} = (\mathrm{J_{SC}} \times \mathrm{V_{OC}} \times \mathrm{FF})/\mathrm{P_{in}} \tag{2.3}$$

where P_{in} is the input power into the solar cell (1000 W/ m^2 at standard temperature conditions) The PCE of a solar cell can be improved by optimizing the design and materials of the device, such as by increasing the light absorption efficiency, improving the charge separation and collection processes, and reducing resistive and recombination losses. Additionally, the PCE can be affected

by external factors such as temperature and illumination intensity.

Chapter 3

PEROVSKITE SOLAR CELLS

This chapter presents the perovskite solar cell history, architecture, working principles, and material properties of the critical layers. Because this thesis focuses on the ETL of the PSC, the properties of TiO_2 and doping TiO_2 will be discussed in more detail.

3.1 History of Perovskite Solar Cells

Gustav Rose discovered the first perovskite mineral, calcium titanium oxide, in 1839 and named it after the Russian mineralogist Lev Perovski [41]. In 1926, Victor Goldschmidt analyzed and characterized the crystal structure of this family of minerals [42]. Figure 3.1 depicts the crystal structure of perovskite as ABX_3, where A is a cation, B is a metal cation, and X is an anion. The perovskite material is made up of organic elements such as methyl ammonium (MA) or formamidinium (FA) as (A), metal elements such as lead (Pb) or tin (Sn) as (B), and halides such as bromide (Br_3), iodide (I_3), or chloride (Cl_3) as (X_3). Christian Moller discovered a cesium lead

halide perovskite structure with the chemical formula $CsPbX_3$ in 1958 [43]. D Weber synthesized the first organic-inorganic compound in 1978 by substituting methyl ammonium (CH_3NH_3) for cesium [44].

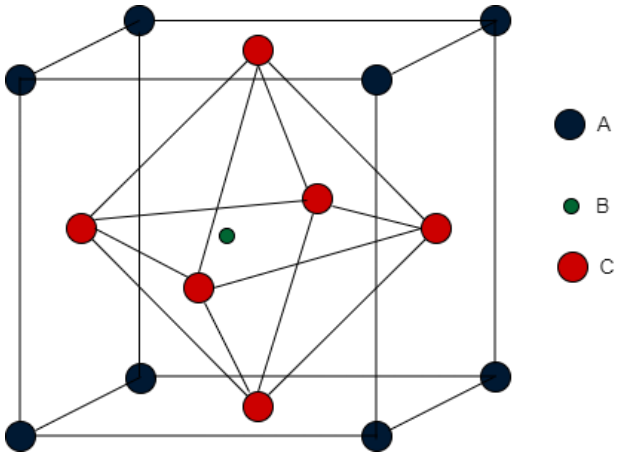

Figure 3.1 Organic- inorganic halide perovskite unit cell [45]

Weber discovered that this particular subclass of perovskite materials could possess photoactive properties. In 2009, Kojima et al. [46] constructed the first hybrid organic-inorganic perovskite solar cell using $MAPbI_3$ as the photo absorber. This first organic-inorganic PSC was created by imitating the architecture of conventional DSSCs. A liquid electrolyte was used for hole transport, and a TiO_2 working electrode was coated with $MAPbI_3$ and $MAPbBr_3$. In 2009, Kojima et al and his research group at Toin University of Yokohama reported the first use of perovskite materials as a sensitizer in dye-sensitized solar cells [46]. They used a methyl ammonium lead iodide perovskite material to replace the traditional organic dyes in the dye-sensitized solar cells. The perovskite solar cells exhibited a much higher efficiency than the conventional dye-sensitized solar cells, which sparked interest in the research community. However, according to Im et al. in 2011, the stability of the solar cells was poor because the perovskite material dissolved in the liquid electrolyte, causing the PSC to lose 80% of their initial PCE after 10 minutes of sustained light exposure [47]. In 2012, Lee et al., in collaboration with Henry Snaith and his group at the

University of Oxford, reported a perovskite solar cell with a power conversion efficiency (PCE) of 10.9% was a significant improvement over the previous record for perovskite solar cells [48]. Around the same time, in 2012, Kim et al. also published the first solid-state PSCs with PCEs of 9.7% [49]. In both instances, the solar cell was modeled after the layers of a solid-state DSSC, in which the photo-absorbing material is deposited in a mesoporous layer of TiO_2 nanoparticles and covered by a layer of the organic hole transport material (HTM) Spiro-OMeTAD. Fluorine-doped tin-oxide (FTO), a transparent conductive oxide, was used as the front contact, and metallic gold or silver as the rear contact.

Since then, a multitude of various layer architectures for PSCs have been published, but the world record PSCs, which have produced a PCE of 22.7%, continue to use an architecture based on TiO_2 and Spiro-OMeTAD [50]. However, recent findings also indicate that the TiO_2 layer can be further enhanced through elemental modification to improve solar cell PCE [51, 52].

3.2 Architecture of Perovskite Solar Cells

In PV technology, the device configuration and architecture are crucial factors in obtaining high power conversion efficiencies [53]. PSC's architectures shown in Figure 3.2 can be classified as regular (n-i-p) or (p-i-n) depending on the properties of the material (ETM or HTM) light is transmitted through first. These two architectures can be either planar or mesoscopic. The mesoscopic structure incorporates a mesoporous layer, adding additional manufacturing costs and generally requiring high-temperature sintering processes that require thermal stability [54–56]. Planar structures consist of all planar layers, low-temperature processing, and high power conversion efficiencies of up to 25.2% [57]. However, this is not limited to a specific device structure. For this study, the regular n-i-p planar device architecture was used.

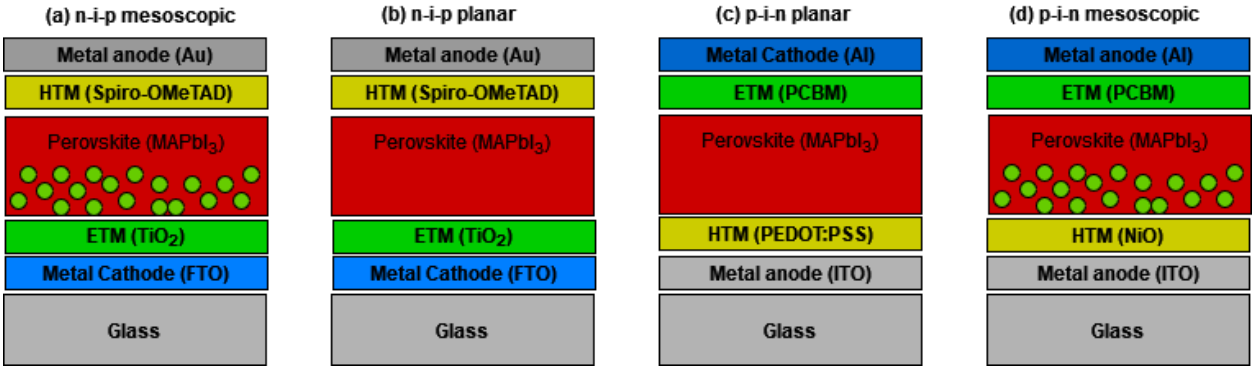

Figure 3.2 Schematic of various PSC's structures (a) n-i-p mesoscopic (b) n-i-p planar (c) p-i-n planar (d) p-i-n mesoscopic [57]

The following materials are commonly used in the development of PSCs [58]:

- A glass or quartz substrate with a front transparent conducting oxide (TCO) contact. TCOs commonly utilized are fluorine-doped tin oxide (FTO) and indium tin oxide (ITO), allowing light transmission and electron collecting in the PSC.
- Deposition of electron transporting material (ETM) on top of the TCO. The most popular ETM is TiO_2, which accepts electrons generated by the perovskite layer and transports them to the front TCO contact. Additional metal oxides explored are aluminum oxide (AlO_3), tin oxide (SnO_2), and zinc oxide (ZnO).
- The ETM layer is covered with a perovskite layer. This layer absorbs photons and produces electrons and holes.
- A layer of hole transport material is placed on top of the perovskite layer to transport holes to the back contact.
- Back contact is often made with a metal such as gold, silver, or platinum; however, carbon has recently been employed [59].

PSCs have a high absorption coefficient, requiring ∼500 nm thick films to absorb most incident photons [60]. In comparison, silicon solar cells require a thick absorbent layer of tens to hundreds of micrometers, signaling the necessity for a far purer and, hence, less expensive material [61]. Excitons in perovskites have low binding energy, making it easier to separate holes and electrons. An efficient charge transport for electrons and holes was reported within perovskites, with carrier diffusion lengths reaching 1 μm [62] which enables the development of incredibly thin devices.

3.3 Operating Principle of Perovskite Solar Cells

Light is transmitted through the FTO and electron transport layer (TiO_2) and absorbed by the perovskite layer to create charge separation, as seen in Figure 3.3(a). This procedure introduces an electron into the conduction band and a hole (positive charge) into the valence band, creating electron-hole pairs. While the electrons are injected into the electron-transport layer and the holes into the hole-transport layer (Spiro-OMeTAD), the electrons fill the positive holes in the cathode layer after passing through an external circuit. A closed circuit cell is formed by connecting the transparent FTO electrode with the back contact metal electrode [63, 64]. To achieve high efficiencies, the ETM's conduction band (CB) must be aligned with the CB of the perovskite as shown in the energy level diagram in Figure 3.3(b) measured from vacuum level, to ensure the potential difference and electric field build-up at the interface are large enough for electron injection while keeping the difference between the ETM's CB and the VB of the HTM as large as possible to maximize V_{OC} [65].

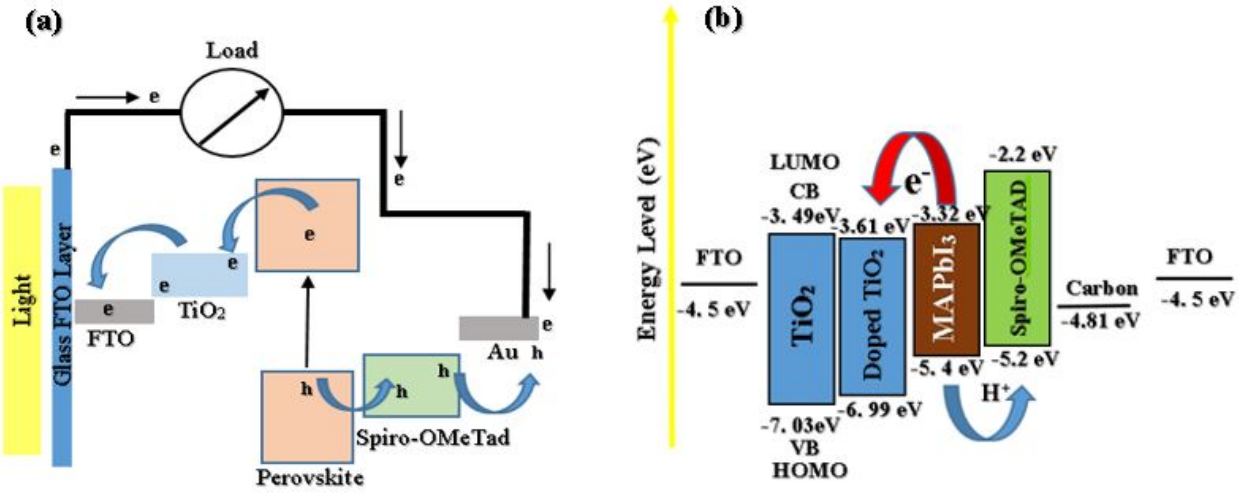

Figure 3.3 (a) Operating principle of perovskite solar cell (b) Energy level diagram of perovskite solar cell [19]

3.4 Material Properties

This section will expand on the material properties of each layer in PSCs used in this study, which include transparent electrodes, perovskite absorber layer, titanium dioxide, Spiro-OMetaD and carbon electrode.

3.4.1 Transparent Electrodes

The front contact, or current-collecting electrode, of most thin film solar cells and PSCs is made of transparent conductive materials (TCMs), predominantly transparent conductive oxides (TCOs). They are part of a material class that simultaneously displays optical transmission and electrical conductivity. TCOs are primarily n- and p-type semiconductors with band gaps more significant

than 3 eV to be transparent in the visible range. Extrinsic doping of the oxides is frequently used to get high conductivity. The three most important n-type TCOs at the moment are indium oxide (In_2O_3), ZnO, and SnO_2 [66].

Tin oxide doped with Florine atoms (FTO) was the first TCO to be widely used, especially for high optical transmission up to 90%, low absorption, high-temperature resistance, mechanical hardness, wide bandgap from 3.2 to 4.6 eV and low-emissivity coatings on glass [67, 68]. They have a resistivity that is greater than TCO based on aluminum zinc oxide (AZO), in the range of 3-4 x 10^{-5} Ω.cm [69]. In contrast to In_2O_3 and ZnO, which are both manufactured using more expensive vacuum-based sputtering processes, SnO_2 can be made using less expensive chemical procedures such as spray pyrolysis with inexpensive basic ingredients like tin chlorides [70]. Thus, transparent electrodes made of SnO_2 are often used in perovskite solar cells. This study used FTO substrates with a sheet resistance of 8.3 Ω / square and a film thickness of 100 nm substrates to fabricate PSCs.

3.4.2 Perovskite Absorber Layer

Halide perovskites constitute a new class of optoelectronic materials with interesting optical and electronic properties. Most halide perovskites are direct-bandgap semiconductors with a bandgap spanning the entire visible spectrum [71]. This is significant because charge carriers in perovskite layers can be generated efficiently in a photovoltaic device. The bandgap of methylammonium lead iodide ($CH_3NH_3PbI_3$) is $\sim$ 1.5 eV, corresponding to an absorption edge of $\sim$ 830 nm for visible light. The Pb and I orbitals are used to construct the valence and conduction bands of the $CH_3NH_3PbI_3$ compound, indicating that the optical properties can be altered by varying the cation or halogen content [72–75]. The bandgap's tunability enables device applications requir-

ing a specific bandgap and distinguishes perovskites from other semiconductor photon absorber materials.

There exist three different phases of $MAPbI_3$ at different temperatures: orthorhombic below 162 K, tetragonal between 162 – 372 K, and cubic above 327 K [76]. The tetragonal phase of methylammonium lead iodide ($MAPbI_3$) is a perovskite crystal structure in which the methylammonium cation (CH_3NH_3+) occupies the A-site of the perovskite structure, and the lead and iodine ions occupy the B-site. The orientation of the methylammonium cation in the tetragonal phase of $MAPbI_3$ is one of the fascinating properties, as opposed to the cubic phase where the cation is isotropically oriented. This orientation has been shown to affect the optical and electronic properties of the material, prompting extensive research into the effect of cation orientation on photovoltaic device performance [77, 78]. The $MAPbI_3$ tetragonal phase has been demonstrated to have numerous desirable photovoltaic features, including strong carrier mobility, long carrier lifetimes, and low recombination rates [77, 79, 80]. These characteristics are attributable to the material's unusual crystal structure, which provides a highly ordered and defect-free environment for charge carriers to transport through. In this study, the $CH_3NH_3PbI_3$ precursor solution was deposited via the one-step spin coating technique and annealed to form a highly crystalline tetragonal phase of $CH_3NH_3PbI_3$ developed confirmed by X-ray diffraction characterization in section 5.1.

3.4.3 Titanium dioxide

The electron transport layer (ETL) is crucial in many types of solar cells and other optoelectronic devices. The primary function of solar cell applications is to improve the extraction of electrons from the light-absorbing material (perovskite). Titanium dioxide (TiO_2) is commonly used as a low-cost material for ETLs due to its large bandgap, chemical stability under ultraviolet light, low

toxicity, photo corrosion resistance, and suitable band edge position with the perovskite material [81–83]. TiO_2 is an n-type semiconductor material that has a bandgap of about ∼3.3 eV in the anatase phase, resistivity is $10^{15}\Omega$.cm [84], and mobility <1 $cm^2\ V^{-1}S^{-1}$ [85]. This means that it has relatively low electron mobility, is transparent to visible light, and absorbs mainly in the ultra-violet region of the electromagnetic spectrum. Titanium dioxide (TiO_2) occurs in nature in three different crystalline forms: anatase (tetragonal), rutile (tetragonal), and brookite (orthorhombic) [86, 87]. Table 3.1 shows the crystal structure properties of the three phases of TiO_2.

Table 3.1 Crystal structure properties of TiO_2 [88]

Properties	**Rutile**	**Anatase**	**Brookite**
Crystal structure	Tetragonal	Tetragonal	Orthorhombic
Ti-O bond length (*A*)	1.937(4) 1.965(2)	1.949(4) 1.980(2)	1.87-2.04
O-Ti-O bond angle	77.7^o 92.6^o	81.2^o 90^o	77^o-105^o
Latice constant (*A*)	a= 3.784 c= 9.515	a= 4.5936 c= 2.9587	a= 9.184 b= 5.447 c= 5.154
Space group	$I4_1/amd$	$P4_2/mm$	Pbca
Molecule	2	2	4
Density (gcm^{-3})	3.79	4.13	3.99
Volume/molecule (A^3)	34.061	31.2160	32.172

Because of its superior charge transport capabilities, anatase is the phase that is most commonly used in PSC applications [89–91]. The anatase crystal structure of TiO_2 is a tetragonal crystal structure with lattice parameters a = b = 4.5936 Å and c = 2.9587 Å [88]. Figure 3.4 shows the

tetragonal anatase structure which consists of a chain of distorted TiO_6 octahedrons, resulting in a unit cell that contains four Ti atoms in positions [0, 0, 0]. [½, ½, ½], [0, ½, ¼] and [½, 0, ¾] and six O atoms [92–94]. The oxygen atoms are arranged in a distorted octahedron around the titanium atom, with two oxygen atoms forming a Ti-O-Ti bond angle of 145° and the other four forming a bond angle of 90°. This arrangement results in the formation of a three-dimensional network of octahedrons that are interconnected through the sharing of corners.

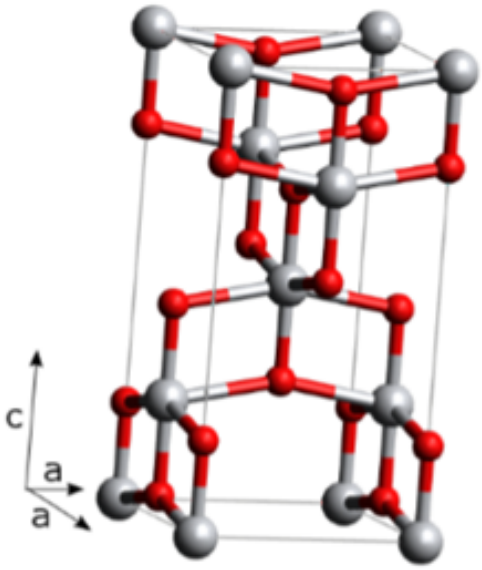

Figure 3.4 The TiO_2 anatase unit cell; titanium atoms are grey and oxygen atoms are red. Six oxygen atoms form a distorted octahedron with a titanium atom at the center, which is clearly illustrated for the central titanium atom [95]

Additionally, TiO_2 formed by sol-gel processes is amorphous. As a result, it must be annealed at high temperatures of 550°C to achieve the desired anatase crystal structure as confirmed by XRD and FTIR in this study. When the anatase-rutile transition occurs, the crystallization temperature may be limited. Given that rutile is the most thermodynamically stable polymorph of TiO_2 at all temperatures, the temperature at which anatase transforms to rutile is highly reliant on the conditions under which it was generated in [96]. Due to their unique band topologies, combined anatase

and rutile phases frequently trap charge carriers and promote recombination processes when they are present in conjunction with other elements [97]. The majority of research has discovered that rutile nanoparticles are harmful to the performance of TiO_2 electrodes; nevertheless, other studies have found that a small amount of rutile nanoparticles can increase device performance [98, 99]. Devices employing rutile TiO_2 generally have a lower CB energy as compared to devices utilizing anatase, leading to a drop in V_{OC}, reducing J_{SC} and FF. Therefore rutile phase is not recommended to be used in PSCs.

In this study, a planar layer of anatase phase TiO_2 consisting of a precursor solution of titanium isopropoxide, ethanol and hydrochloric acid was deposited onto the FTO layer via spin coating and used as the reference ETL material.

Electron Trapping and De-Trapping in Titanium dioxide

The lower conduction band edge of TiO_2 is composed of empty Ti^{4+} 3d bands, whereas the upper edge of the VB is composed of filled O^{2-} 2p bands [100]. Bulk oxygen vacancies, titanium interstitials, and reduced crystal surfaces generate shallow electron traps that can increase the conductivity of TiO_2. The Ti^{3+} species, which form a band of ~ 0.5 eV below the TiO_2 CB, are of particular significance in this case [101, 102]. These defects function as n-type dopants, increasing the number of unbound electrons in TiO_2 and, consequently, its conductivity and current. These defects may also act as charge traps and are recombination centers, resulting in a degraded device performance [103].

Trapping typically occurs at surface and bulk abnormalities produced by lattice defects [104]. Based on the energy connected with the trapping sites, it is classified as shallow or deep trapping. Shallow trapping spots can be found slightly below or above the CBM. The energy associated

with these trapping sites is similar to thermal excitations. Thermal excitation at room temperature causes charge carrier de-trapping (the release of trapped carriers) in shallow sites. Surface states are one type of shallow trapping site that occurs naturally due to dangling bonds at the surface. There are bulk trapping sites in the bandgap, and the energy associated with them about the CBM or the VBM is frequently more than thermal excitation at a given temperature [105]. Trapping sites are confined, and preparatory methods heavily influence their occurrence. When TiO_2 is reduced or annealed in a vacuum, oxygen vacancies or localized Ti^{3+} sites form at the surface [106–108]. In TiO_2 thin films, these oxygen vacancies serve as the primary trapping sites for electrons. These surface trapping sites substantially impact the performance of TiO_2 under various situations, particularly when the surface is entirely bound with or blocked by organic molecules.

TiO_2's electron transport is complex and challenging to study due to its numerous defects and the resultant sub-bandgap states shown in Figure 3.5(a). This is especially challenging in the case of devices because parameters about a single device property cannot be investigated separately without significantly altering other material properties. Figure 3.5(a) also depicts significant experimental and theoretical evidence indicating that charge transport in TiO_2 occurs by de-trapping from sub-bandgap states. These states are located deep in the density of states (DOS, number of available states at a given energy), shown in Figure 3.5(b), where electrons can be de-trapped into the CB. The film's conductivity is dictated by the probability of electrons being in the CB, which increases as the quasi-Fermi level approaches the CB. Therefore, any change that eliminates deep trap states will increase the conductivity of the film [109].

These factors result in a complex situation in which shallow traps are necessary for charge transport and can even improve conductivity. In contrast, deep traps lower the quasi-Fermi level, making it more challenging to detrap electrons, thereby reducing conductivity and increasing recombination. The V_{OC} of the device, which is dependent on the energy difference between the CB

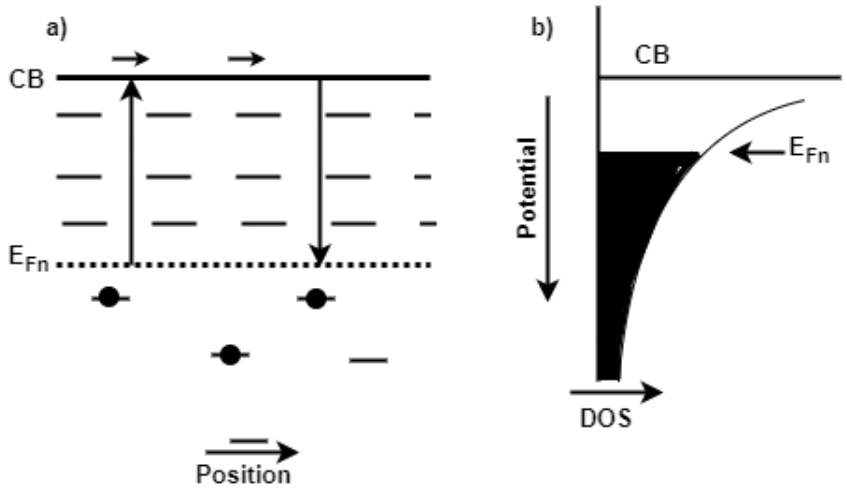

Figure 3.5 (a) Trapping and de-trapping process occurring in TiO_2. The Fermi energy level (E_{Fn}) is represented by the dotted line; the longer dash lines represent vacant sub–bandgap sites, the circles represent the electrons, with the vertical arrow representing trapping and de-trapping and horizontal arrows representing transport. (b) Density of states (DOS) distribution in thin films [109].

of TiO_2 and the VB of the HTM, is also affected by the trap states, with shallower traps leading to a greater V_{OC}. In addition, traps can serve as electron and hole recombination sites [110], reducing current and voltage.

Due to forming a space charge region at the interface between TiO_2 and perovskite, band bending occurs, indicating that the CB in bulk and at the surface have different energies. The space charge region produces an electric field separating electrons and holes. An external voltage can counteract band bending and reduce the space charge region. This particular voltage is known as the flat band potential (V_{FB}) [111]. Because trap states are predominantly located on the TiO_2 surface, they significantly impact V_{FB} and, by extension, the electron-hole separation efficiency. When V_{FB} is negatively shifted (indicating an upward shift of the CB and the Fermi level), electron injection from the perovskite into TiO_2 becomes less efficient, resulting in a current loss. Some defects increase injection efficiency by positively shifting V_{FB}, resulting in a downward displace-

ment of the CB and Fermi levels. Given the interconnectedness of so many processes, it is evident that devising a method to enhance the electronic properties of TiO_2 is not simple.

Doping Electron Transport Layer

Doping the electron transport layer (ETL) of titanium dioxide (TiO_2) is a common technique used to improve the performance of perovskite solar cells. This can be achieved by the purposeful introduction of impurities into the TiO_2 lattice by sol-gel, hydrothermal, solvothermal methods, etc., which have been shown to alter the electrical, morphological, and optical characteristics of titanium dioxide [112–114].

Doping of titanium dioxide (TiO_{2-}) can be achieved by either substitution of Ti^{4+} cation (n-type doping) or O^{2-} anion (p-type doping) with dopant ions. Both methods have advantages and disadvantages, and the choice of doping method depends on the type of dopant and the desired doping concentration. The Ti^{4+} cation substitution method involves the substitution of Ti^{4+} cations with dopant ions in the TiO_2 lattice. The dopant ions can be of lower valence than Ti^{4+} (e.g., Fe^{2+}, Zn^{2+}, Cu^{2+}, Ni^{2+}) or of higher valence than Ti^{4+} (e.g., Nb^{5+}, Ta^{5+}, Zr^{4+}) [115]. Because the ion sizes of Ti^{4+} and Zn^{2+} are comparable [116, 117], lattice deformation is minimal when Zn^{2+} is introduced into the TiO_2 lattice, as demonstrated by XRD in this study with the weight percentage composition quantified by EDX.

The O^{2-} anion substitution method involves the substitution of O^{2-} anions with dopant ions in the TiO_2 lattice. The dopant ions can be of lower valence than O^{2-} (e.g., N^{3-}, S^{2-}, F^{-}) or of higher valence than O^{2-} (e.g., Zr^{4+}, Nb^{2-}) [118]. The VB upper edge comprises O^{2-} 2p bands, which can be replaced by different anions. This method has also been shown to modify the energy levels of TiO_2, reduce the energy barriers for electron transport and injection, and improve the charge

transport properties.

The color red in Figure 3.6 shows the doping-induced states. In pristine TiO_2 shown in Figure 3.6(a), electrons are transferred from one shallow trap to another until they reach the electrode by 'hopping' from shallow trap to shallow trap. As a result, the shallow trap density will affect the electron transport rate and the J_{SC}. Deep traps have the potential to permanently capture electrons and operate as recombination sites, which can have an impact on V_{OC}. As previously stated, another crucial component affecting V_{OC} is E_F because V_{OC} is defined as the difference between the E_F of TiO_2 and the HTM.

Doping can reduce the deep trap density, resulting in an upward shift of the E_F as shown by the n-type doping in Figure 3.6(b), resulting in an improvement in V_{OC} produced. Removing deep traps causes recombination to be delayed even more, increasing the value of V_{OC} produced. A drop in driving force for electron injection is achieved via shifting the CB to a position closer to the LUMO of the absorber. This, in combination with a decrease in trap density and the resulting electron transport, results in a fall in J_{SC}.

As a result of the creation of deep traps due to p-type doping shown in Figure 3.6(c), the conduction band and E_F are lowered. In conjunction with increased recombination via the deep trap states, the amount of V_{OC} produced reduces. Since the CB and absorber LUMO are located farther apart, electron injection is better, and the greater trap density increases electron transport, leading to an improved J_{SC}.

TiO_2 doped with Mg, Nb, Y, Al, and Zr has previously been used in perovskite solar cells. Mg-doped ETL has improved V_{OC} because of its strong conduction band and low recombination [119]. Nb doping boosted electron injection and transport, resulting in greater J_{SC} [120], and Y doping improved performance due to increased perovskite loading, resulting in significant increases in J_{SC}

and marginally reduced recombination [121]. It has been found that Al-doping reduces the number of oxygen vacancies and the associated deep trap states, lowering recombination and increasing film conductivity. As a result, J_{SC} increased overall [122]. Doping TiO_2 with Zr^{4+} reduced hysteresis while pushing the CB upward and reducing recombination, increasing V_{OC} [123]. However, reports on the effect of Zn doping of TiO_2 have been inconsistent. It was reported to negatively shift the flat band potential in some [124, 125] but to positively shift V_{FB} in others [126].

In this study, varying molar percentages (0-5 mol%) of Zn ions as a dopant for TiO_2 thin film were investigated to assess the effects on the morphology, structural and optical properties, and performance of the perovskite solar cells.

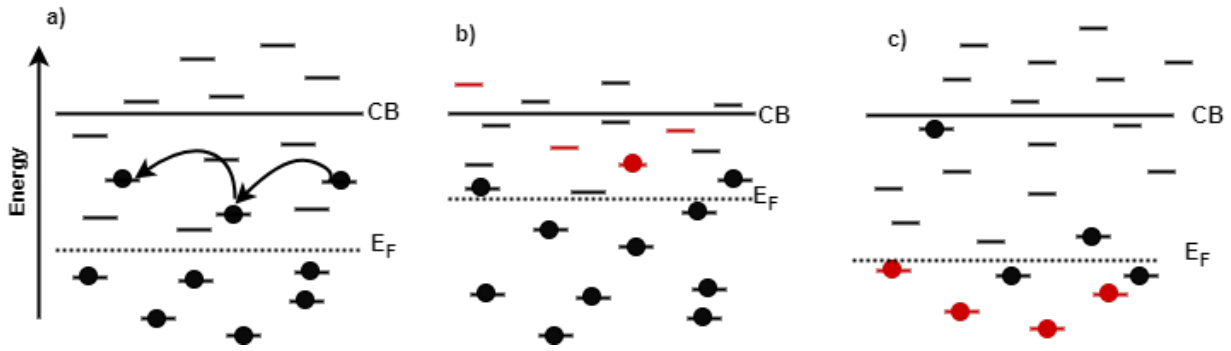

Figure 3.6 The effect of TiO_2 doping on the CB and E_F [127]

3.5 Hole Transport Layer

Spiro-OMeTAD has been the most commonly used and state-of-the-art material for perovskite hole transport layers (HTLs). It consists of a spirobifluorene core and is a highly efficient hole transport material due to its bandgap of ∼2.99 eV, excellent charge transport properties, high melting point, appropriate energy level alignment with the perovskite layer ($CH_3NH_3PbI_3$) and high hole mobility of $\sim 10^{-4}$ $cm^2V^{-1}S^{-1}$ [128, 129]. Lithium and 4 tert-butyl pyridine doping of Spiro-

OMeTAD is employed to efficiently extract the photogenerated holes in the perovskite layer and transport them to the back electrode and block electrons [130, 131]. Spiro-OMeTAD has been found to significantly improve PSC device performance, with power conversion efficiencies of up to 25.7% reported in some of the best-performing devices. Spiro-OMeTAD does, however, have some drawbacks, including cost, efficiency, temperature- and additive-related deterioration, long-term stability, film quality, additive dependence, and hysteresis. Therefore, it appears that the development of alternative HTMs without these fundamental disadvantages is required to commercialize PSCs [132].

3.6 Back Metal Contact

A back contact is fundamental to complete the internal circuit and serves as an electrode supplying current and voltage for the external electrical work. The work function is an important property that refers to the minimum amount of energy required to remove an electron from the surface of a metal and move it to a point just outside the metal. Metals (Ag, Au, Al, Cu, Ni, Pt, etc.), transparent conductive oxides (FTO; fluorine-doped tin oxide), (ITO; Indium tin oxide), (IZO; indium zinc oxide), (AZO; aluminum zinc oxide) are some of the most frequently used back electrodes. Among the back contacts mentioned, devices with Au/Ag have demonstrated excellent performance, but both have drawbacks. Au is expensive and deposited by thermal evaporation at higher temperatures, increasing the sample temperature [133], which could lead to defects and affect the PSC device performance, while Ag is chemically unstable. Recent research by Chang et al. on cost variables in perovskite modules revealed that using a Au electrode accounts for more than 70% of the module's expense [134]. In PSCs, the back electrode should have appropriate energy levels, a high work function typically between 5 - 5.7 eV, high electrical conductivity, excellent chemical

resistance, and environmental stability, and be cost-effective [135]. Carbon materials with a work function of approximately 5 eV have demonstrated to be appropriate alternatives to Au back electrodes having a work function of 5.1 eV, enabling decreased expense and use of expensive thermal evaporation equipment for the deposition of metal contacts[136]. Carbon-based back electrodes can be applied by simple deposition techniques, such as doctor blading, screen-printing, and drop-casting [137, 138]. In this study, activated carbon black with an FTO layer was placed on top of the HTL and used as the back contact. Using activated carbon as the back contact has shown promising results, and further research is required to fully understand its benefits and limitations.

Chapter 4

METHODOLOGY

This chapter will provide an overview of the synthesis procedure for the Zn-doped TiO_2 nanoparticles, device fabrication using the spin coating depostion technique, experimental characterization methods and describe it's working principles. In addition, the numerical analysis method used for the fabricated PSCs is briefly explained within the context of the results presented in this thesis.

4.1 Sol-Gel Technique for Nanometal Oxide Synthesis

The sol-gel method uses a liquid precursor solution known as sol which is converted into a solid gel through a series of chemical reactions, making it a versatile and widely used method for synthesizing nanometal oxides. Typically, the sol-gel process begins with preparing an alcohol solution of a metal alkoxide precursor solution (M-OR), such as titanium isopropoxide or aluminum isopropoxide. Water is added to the alkoxide precursor solution, and a catalyst is added, such as hydrochloric acid or acetic acid, to hydrolyze it, as shown below in the hydrolysis reaction. The hydrolysis re-

action breaks metal-alkoxide bonds, forming a metal hydroxide solution. This metal hydroxide colloidal solution is allowed to age, which then undergoes a condensation reaction between two metal hydroxyl/alkoxy leading to M-O-M (metal-oxygen-metal) bonds with the release of H_2O/ R-OH [139]. The condensation continues, resulting in a sol-gel transition, an interconnected, rigid, and porous inorganic network in the liquid phase. This liquid phase can be dried under ambient conditions to produce a xerogel. The gel can be dried by removing the liquid solvent under hyper-critical conditions without destroying the gel network to form an aerogel. Finally, the gel can be sintered at a high temperature (800° C) to collapse the gel network into a powder [140, 141].
The reactions involved in the sol-gel process are shown below:

- Hydrolysis Reaction

  M-OR + H_2O (Metal alkoxide) $\rightarrow$ M-OH + ROH (Metal Hydroxide)

- Condensation Reaction

  M-OR + H O-M $\rightarrow$ M-O-M + R-OH

By modifying the precursor concentration, solvent, pH, and use of an acid for the hydrolysis reaction, the size and properties of the resulting metal oxide nanoparticles can be altered [142].

4.2 Spin-Coating Method

Spin coating is currently the standard laboratory solution deposition technique for thin film formation on substrates due to relatively low costs, high repeatability, film uniformity, and simplicity of the process. It involves depositing the precursor solution onto a static or spinning substrate at speeds around 500 – 5000 rpm. The rotation of the substrate throws off a large portion of the

solution and spreads the remaining solution due to the centrifugal force into a thin, uniform film that dries via evaporation and adheres to the substrate surface typically over a period of 5- 60 s. The film thickness t is determined primarily by the solution concentration (c), viscosity (η), and the speed of the substrate rotation (ω) according to the relation [143].

$$t \propto \frac{c\eta}{\sqrt{\omega}} \tag{4.1}$$

By adjusting the spin speed and concentration of the precursor solution, it is possible to control the film's thickness. Based on the precursor solution's composition, morphology, and structure, the resultant thin film may display various properties. For instance, the thickness and texture of a film can influence its optical, electrical, and mechanical properties [144]. When considering the industrialization and commercialization of solution-processed solar cells, it is essential to consider alternative deposition techniques due to the high solution loss, requirement for flat and smooth substrate surfaces, and inherent batch-to-batch nature of the process. Nonetheless, spin coating continues to be a valuable and extensively employed method for depositing high-quality thin films with precise control over their thickness, morphology, and properties.

4.3 Device Fabrication

The following chemicals were used to fabricate Zn-doped TiO_2 perovskite solar cells. Methyl ammonium iodide (MAI, 99%), lead (II) iodide (PbI_2, 99.9%), titanium isopropoxide (TTIP), 2, 2', 7, 7'-Tetrakis (N, N-di-p-methoxyphenylamino)-9, 9'- Spirobifluorene (Spiro- OMeTAD powder), 4- tert – butylpyridine (TBP, 96%), bis (triflouromethane sulfonimide lithium salt (LiTFSI), ethanol (EtOH, super dehydrated), chlorobenzene, dimethylformamide (DMF, super hydrated), dimethyl-

sulfoxide (DMSO, super hydrated), hydrochloric acid (HCL), di-ethyl ether, zinc chloride, were purchased from Sigma-Aldrich Co. The fabrication steps in the development of undoped and Zn-doped TiO_2 perovskite solar cells are shown in Figure 4.1d.

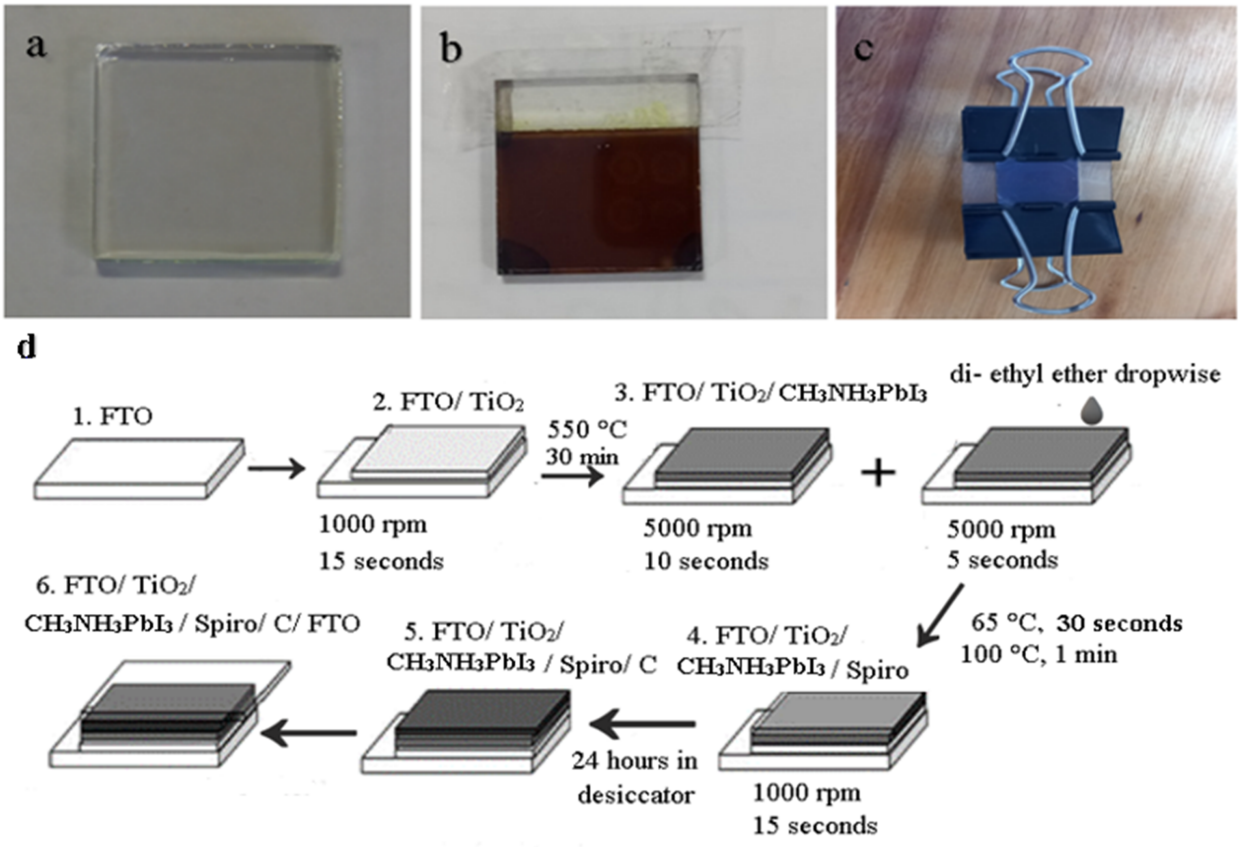

Figure 4.1 (a) TiO_2 spin-coated on FTO glass substrate (b) Methyl ammonium lead iodide spin-coated and annealed on TiO_2 layer (c) Completed PSC (d) Fabrication steps of PSC

4.3.1 Substrate Preparation

Fluorine-doped tin oxide (FTO) coated glass substrates of 25 mm x 25 mm with a thin film thickness of 100 nm and sheet resistance of 8.3 Ω/ square were cleaned in a beaker containing detergent and deionized water. Each substrate was then rinsed in an acetone before being placed in the ultra-

sonic cleaner. The substrates were then immersed for 20 minutes at 80°C in the ultrasonic cleaner containing ethanol. The substrates were removed and put into a beaker containing deionized water before being placed on a hotplate at 60°C for 10 minutes or until totally dry. The substrates were then placed for 20 minutes in an Ultra Violet Ozone (UVO) cleaner to break down organic surface impurities and provide an ultra-clean surface for the deposition of the ETL layer.

4.3.2 Zn – doped TiO_2 Preparation and Deposition

In a volumetric flask, 40 ml deionized water was combined with 7.29 ml HCL and mixed for 3 minutes before adding additional de-ionized water up to 100 ml to obtain a 2M HCL stock solution. To prepare the 0.22 M TiO_2 precursor solution with Zn doping of 0.5, 1, 2, 5 mol%, the required amount of zinc chloride was added to 14.29 ml ethanol and stirred vigorously at 6000 rpm for 30 minutes, then 0.28 ml of the 2M HCL stock solution was slowly added and stirred vigorously at 6000 rpm for an additional 30 minutes, after which 1 ml of TTIP was slowly added and stirred for 2 hours. The resulting solution was then filtered using a 0.45 micrometer Teflon filter before spin coating to ensure the removal of small particles to obtain a smooth and uniform surface coverage. The FTO substrates were then pre-heated to 60°C before dynamically spin coating 300 µL of the Zn–doped TiO_2 precursor solution at 1000 rpm for 15 seconds and annealed on a ceramic digital hotplate at 550°C for 30 minutes to form the clear and transparent Zn-doped TiO_2 thin film layer shown in Figure 4.1a. This layer was then UVO treated for 15 minutes before the methyl ammonium lead iodide precursor solution deposition.

4.3.3 Perovskite Layer Preparation and Deposition

To prepare the perovskite precursor solution, 0.16 g of methyl ammonium iodide and 0.46 g of lead iodide were added to 0.08 ml of dimethyl sulfoxide (DMSO) and 0.6 ml of dimethylformamide (DMF) and magnetically stirred at 3000 rpm for 24 hours. After filtering the perovskite precursor solution using a 0.45 micrometer Teflon filter, 250 µL was statically spin-coated at 5000 rpm for 15 seconds, with 350 µL of di-ethyl ether slowly dripped from a distance of about 2 cm from the revolving substrate during the final 5 seconds. To develop the dark brown and semitransparent perovskite layer shown in Figure 4.1b, the coated surface was placed on a digital hotplate at 65 °C for 30 seconds, then slowly ramped up to 100°C and annealed for approximately 1 minute. This was placed in a vacuum desiccator for 3 hours before the deposition of the hole transport layer to minimize exposure to oxygen and humidity.

4.3.4 HTL Preparation and Deposition

The hole transport layer was prepared by dissolving 0.52 g of LiTFSI in 1 ml acetonitrile and stirring vigorously for 10 minutes to form the LiTFSI stock solution. Then 0.07 g of Spiro-OMeTAD powder was added to 1 ml chlorobenzene and stirred vigorously for 10 minutes to form the Spiro-OMeTAD solution. After which, 0.03 ml of TBP and 0.02 ml of the LiTFSI solution were added to the Spiro-OMeTAD solution and stirred for 30 minutes. After that the Spiro-OMeTAD solution was filtered using 0.45 micrometer Teflon filter, 200 µL was dynamically spin-coated at 1000 rpm for 15 seconds and placed in a vacuum desiccator overnight before applying $\sim$8 mg of activated carbon powder and FTO and held together using binder clips to form the back conductive electrode shown in Figure 4.1c.

4.3.5 Synthesis Zn-doped TiO_2 Nanoparticles

To synthesize the Zn-doped TiO_2 nanoparticles, the Zn-doped ETL precursor solution was aged 72 days to form a clear and transparent gel. The gel was then dried for 12 hours at 80°C in a hot air dryer to obtain dry TiO_2 powder. After drying, the TiO_2 powder is heated for 30 minutes at 550°C in a furnace to produce anatase TiO_2 nanoparticles for FTIR, XRD, and TEM investigation.

The PSC fabrication and nanoparticle synthesis equipment setup is shown in Figure 4.2. The POLOS 200 advanced single substrate spin processor was used for spin coating of the ETL, perovskite, and HTL thin film layers.

Figure 4.2 The thin film research PSC laboratory fabrication setup

4.4 Characterization Techniques

This section provides an overview of the characterization techniques including a concise description of the working principles of some of the less straightforward techniques.

4.4.1 Scanning Electron Microscope

Scanning Electron Microscopy (SEM) is an effective method for microscopic surface imaging of samples and is an effective characterization tool. Nanomaterial surface structure research benefits greatly from SEM analysis. Images are created by scanning a material with a beam of electrons. Electrons collide with sample atoms, creating a variety of signals that can be utilized to reconstruct an image of the sample's topography and composition [145]. In this study, secondary electrons serve as the relevant signal. These electrons are emitted from the sample and captured by a detector seen in Figure 4.3 as a result of inelastic beam scattering interactions with beam electrons. High-resolution pictures of surface features as small as 0.5 to 5 nm can be recovered by connecting the number of secondary electrons with the beam position [146, 147]. A Zeiss SEM operating at 40 kV and 40 mA was used for the SEM analysis of the ETL and perovskite surface layers. ImageJ's version 1.48 image processing software was used for image measurements.

4.4.2 Energy-Dispersive X-Ray Spectroscopy

Scanning electron microscopy's incorporation of X-ray or photon radiations is the foundation of Energy-Dispersive X-ray spectroscopy (EDX). In tandem with SEM, the characterization instrument EDX allows for qualitative and quantitative investigation of constituents inside a sample.

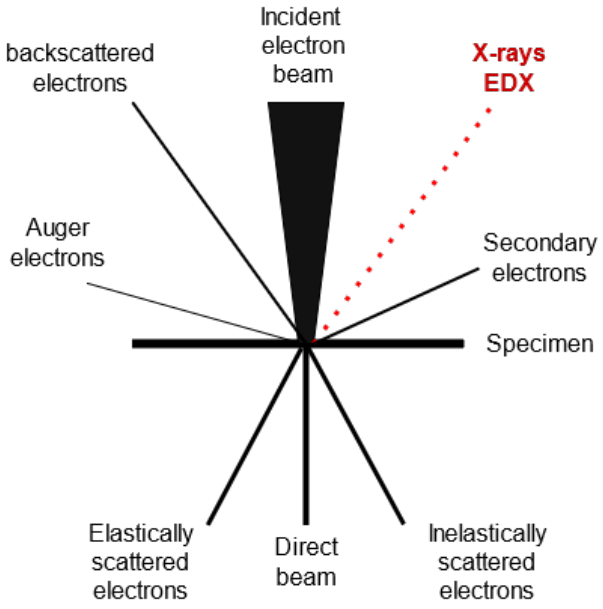

Figure 4.3 Electron-matter interactions resulting from the impact of an electron beam on a sample [148]

Emissions of X-rays occur when atoms in a substance undergo electronic transitions from higher to lower shells. The K, L, and M shell electrons of the atoms that make up the sample shown in Figure 4.4 are excited by the high-energy incident electron beam in EDX, leaving behind holes. X-rays are produced as electrons from the upper shells of the atom move into empty shells lower down the atomic structure. Each element in the sample leaves a unique fingerprint at each transition. Each chemical element in a sample can be identified and quantified with the help of an X-ray spectrum [149, 150]. This allowed us to quantify the weight percentage contribution of each element present in the FTO, ETL and perovskite layers.

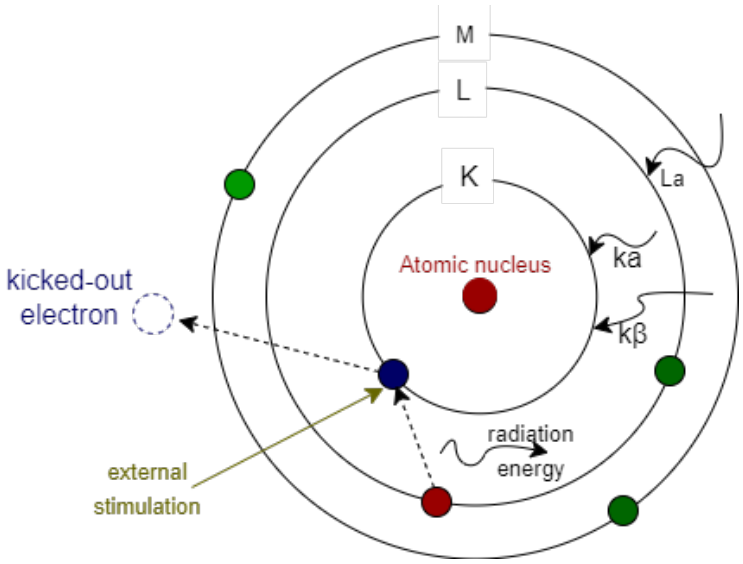

Figure 4.4 Illustration principle of EDX [151]

4.4.3 Fourier Transform Infrared Spectroscopy

Fourier transform infrared spectroscopy (FTIR) utilizes infrared radiation to determine the chemical bonds and functional groups present in organic and inorganic molecules. Infrared radiation has longer wavelengths than visible light and is absorbed by molecules vibrating at particular frequencies. When infrared radiation is transmitted through a sample, the energy absorbed by the sample causes the molecules to vibrate, resulting in a distinct spectral pattern [152]. Mirrors and lenses direct IR radiation to a sample during sample analysis, as shown in Figure 4.5. The sample emits an IR spectrum between 4000 and 400 cm^{-1} in wavelength. The FTIR spectrum reveals the sample's characteristic peak positions corresponding to specific functional groups and chemical bonds. These peaks can be used to determine the sample's structure and composition. The peaks' position and shape reveals the categories of bonds present and their vibrational modes. Figure 4.5 represents the FTIR instrumental arrangement. The functional groups present in the ETL and perovskite layers were determined using an Agilent Cary 630 ATR-FTIR with a diamond crystal operating between 400 and 4000 cm^{-1}.

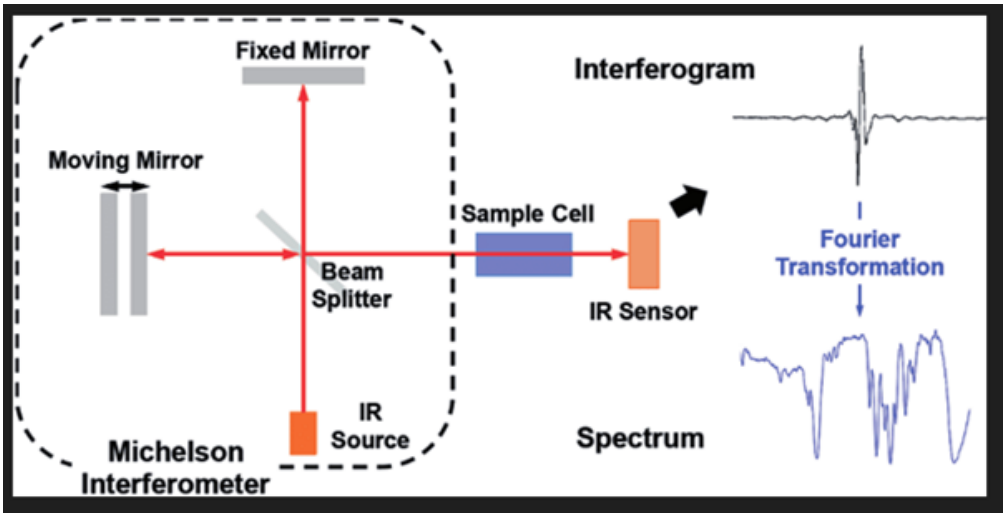

Figure 4.5 Typical FTIR instrument setup [153]

4.4.4 Transmission Electron Microscope

Transmission Electron Microscopy (TEM) is a technique used for imaging the internal structure of materials at a very high resolution, typically in the range of a few angstroms (Å). TEM works by directing a beam of electrons through a thin sample and analyzing the interactions between the electrons and the atoms in the material [154]. The TEM consists of an electron source, a condenser system, a series of electromagnetic lenses, and a detector shown in Figure 4.6. The electron source produces a beam of electrons that is focused onto the sample using the lenses (objective, aperture, and projective). The electrons are accelerated to high energies, typically 100-300 kV, to achieve high-resolution imaging [155]. As the electron beam passes through the sample, it interacts with the atoms in the material. Some electrons are scattered or absorbed, while others pass through the sample and are collected by the detector. The collected electrons produce an image on a fluorescent screen or a detector that can be analyzed to determine the material's particle size and morphology. The TiO_2 and Zn-doped TiO_2 nanoparticles were dispersed in ethanol to form a colloidal solution and placed on the TEM grid for imaging. The TEM images were captured using

the JEOL 1010 Transmission Electron Microscope which allowed for the analysis of the size, shape and distribution of TiO_2 and Zn-doped TiO_2 nanoparticles.

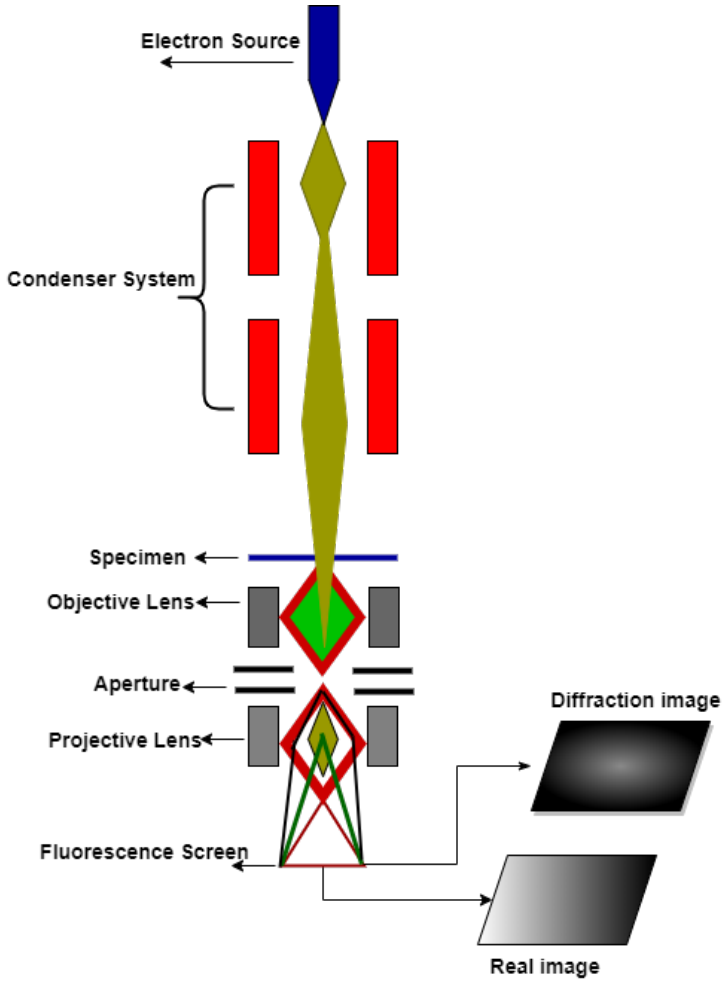

Figure 4.6 Schematic of TEM setup [156]

4.4.5 X-Ray Diffraction

X-ray diffraction (XRD) is a material characterization technique to identify the crystal structure. XRD works by projecting an X-ray beam onto a material and measuring the scattered X-rays. The crystal structure of a material can be identified by analyzing the pattern of scattered X-rays.

The Rietveld refinement approach provides for a deep study of the XRD-generated spectra by approximating the measured diffractogram with a least-squares fitting algorithm [157]. The Scherrer formula [158, 159] can be used to calculate the average crystallite size D in this manner. The Scherrer formula is as (4.2):

$$D = \frac{K\lambda}{B\cos\theta} \tag{4.2}$$

where D is the size of the crystalline particle, K is a dimensionless shape factor that depends on the shape of the particle (typically between 0.89 and 1), λ is the wavelength of the X-ray radiation used, B is the diffraction peak's full width at half maximum (FWHM) in radians, θ and is the Bragg angle. From the angle of diffraction and the wavelength of the X-rays employed in the experiment, Bragg's law [160] can be used to calculate the interplanar distance, d, between the lattice planes of a crystal.

Bragg's law is expressed as:

$$d = \frac{n\lambda}{2sin\theta} \tag{4.3}$$

where n is the diffraction peak order, λ is the X-ray wavelength, d is the interplanar spacing, and θ the diffraction angle. For the first-order diffraction peak, n is commonly assumed to be 1. Once the value of d is determined, it can be utilized to determine the material's crystal structure. Different crystal forms with different interplanar spacings exist in different materials. The material's crystal structure can be recognized by comparing the computed value of d to known interplanar spacings for different crystal structures [161]. In this investigation, XRD was performed using a type D8 Advanc produced by M/s Bruker AXS, Germany, to identify and evaluate the crystal structure and orientation of Zn-doped- TiO_2 and $CH_3NH_3PbI_3$ layers.

4.4.6 UV-Vis Spectroscopy

UV-vis spectroscopy is a non-destructive quantitative characterization technique used to evaluate a sample's optical properties, such as absorption, transmittance, and reflectance. UV/Vis spectroscopy determines a semiconductor material's absorbance and bandgap. The intensity of light flowing through a sample (I) is compared to the intensity of light before it goes through the sample (I_0) in UV/Vis spectroscopy. The transmittance (T) is defined as I/I_0, and the absorbance (A) is defined as:

$$A = -log(T) \tag{4.4}$$

Absorbance is often displayed against the wavelength of the entering light, indicating which portion of the spectrum is absorbed by the substance [162]. The bandgap energy of semiconductors can be calculated from the absorption onset or Tauc plot presented below. The absorption properties were measured using an Agilent Cary 60 UV-Vis-NIR spectrophotometer.

Tauc Plot

The Tauc plot is a popular technique for determining the optical bandgap of thin films from absorbance spectra. The Tauc plot is based on the idea that a material's absorption coefficient at its absorption edge can be expressed as (4.5):

$$(\alpha hv)^n = A\,(hv - E_g) \tag{4.5}$$

where:

α is the absorption coefficient

hv is the incident light's photon energy

A is a constant related to the material's qualities,

E_g is the bandgap energy, and

n is a constant that varies depending on the type of transition (n=2 for direct transitions, and n=1/2 or 3/2 for indirect transitions). Plotting $(\alpha hv)^2$ vs hv yields a straight line with a slope of 2 and an intercept of $A(Eg)^{\mathrm{n}}$ [163]. The intercept of the linear fit can be used to calculate the bandgap energy. To determine the Tauc plot of thin films the absorbance spectra is required to be measured using techniques such as UV-Vis spectroscopy. The Tauc plot of the TiO_2, Zn-doped TiO_2 and perovskite layers were determined by measuring the absorbtion spectrum across a range of photon energies and plotting $(\alpha\mathrm{hv})^2$ or $(\alpha hv)^{1/2}$ against hv. The bandgap energy of TiO_2, Zn-doped TiO_2 and perovskite layers were determined from the intercept of the tangent line on the x-axis from the linear region of the Tauc plot using Origin software.

4.4.7 Photoluminescence

Photoluminescence spectroscopy (PL) is a non-destructive characterization technique used to investigate materials' electronic structure, particularly in semiconductor physics. Material parameters such as bandgap energy, impurity levels, defect states, and recombination pathways are determined using the acquired PL spectrum [164]. As shown in Figure 4.7, a light source is used to illuminate a sample and provide the excitation photons. The sample material absorbs photons with appropriate energy from the light source. The absorbed photon energy moves electrons from the valence band to the conduction band. Photoexcited electrons typically lose extra energy by occupying the lowest energy level in the conduction band. These electrons eventually return to the valence band's maximum energy level. The energy produced during inter-band transitions from the conduction band to the valence band is directly related to the material's bandgap energy, also known as the forbidden gap, resulting in the emission of luminescence photons from the sample [165]. As a result, photoluminescence refers to photoexcitation and emission in a sample. The

photoluminescence intensity measurements were carried out using the Perkin Elmer Lambda 35 spectrometer. This allowed for the identification of the peak position, intensity and bandwidth to provide insight into recombination dynamics and analysis of the photoluminescence spectrum of Zn-doped TiO_2/ perovskite layers.

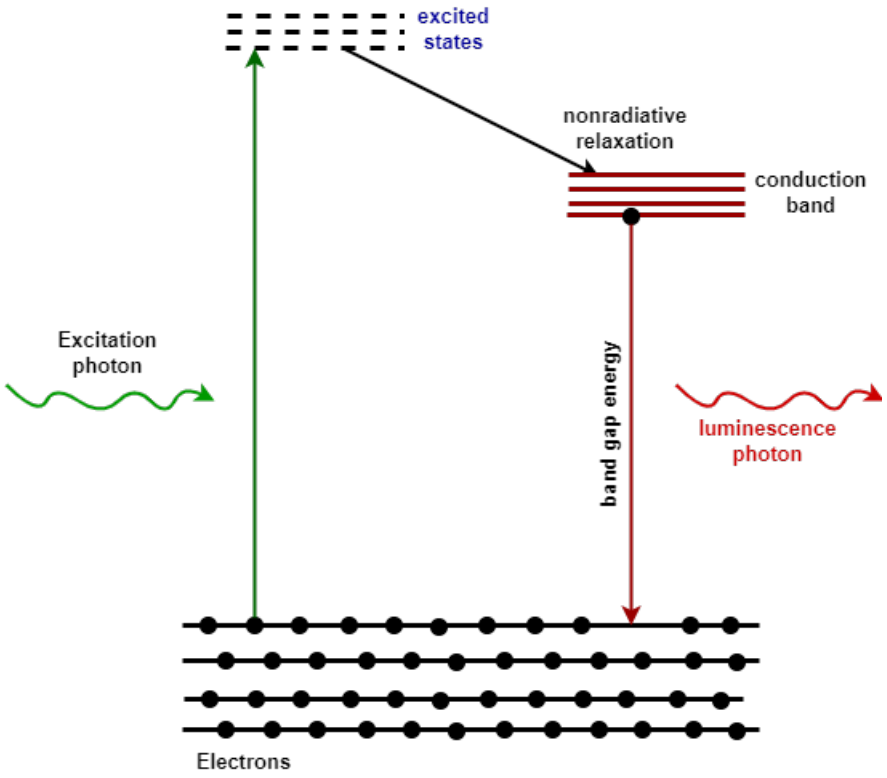

Figure 4.7 Photoexcitation and emission in a sample

4.5 Performance Testing Setup

The solar simulator is a research tool used to characterize the performance of solar cells. The illumination spectrum and intensity should approximate that of the sun. In this study, an Ossilla solar simulator equipped with an LED light source of 1000 W/ m^2 coupled with an AM 1.5 filter and

Keithley 2460 source measuring unit was used to determine the J-V characteristics on cells with an active area of 0.1 cm^2 defined by a masked aperture. The devices were measured immediately after fabrication under ambient conditions of a controlled temperature of ∼20°C with the relative humidity maintained at < 65%

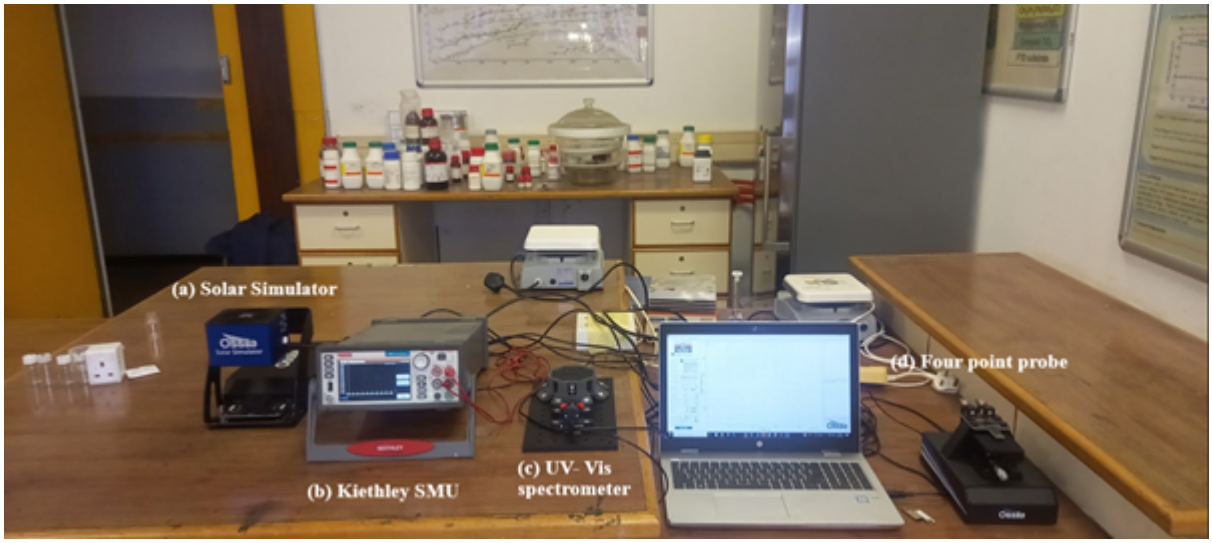

Figure 4.8 Performance testing setup

4.6 Numerical Method

Numerical simulations save time and cost and optimize experimental design problems without implementation in an experimental laboratory environment. These are the main reasons computer-based learning is emphasized in universities worldwide. To analyze solar cells numerically, the software must be capable of solving three coupled differential equations namely, Equation (4.6) Poison's equation, (4.7) continuity equation for holes and (4.8) continuity equation for electrons as follows:

$$\frac{d}{dx}\left(r(x)\frac{d\Psi}{dx}\right) = q\left[p(x) - \pi(x) + N_D^+(x) - N_A^-(x) + p_l(x) - n_t(x)\right] \tag{4.6}$$

$$\frac{1 d j_p}{dx} + R_p(x) - G(x) = 0 \tag{4.7}$$

$$-\frac{1}{\int}\frac{d}{dx} + R_n(x) - G(x) = 0 \tag{4.8}$$

Where:

q = electron charge

Ψ = electrostatic potential

n_t = electron concentration

p_t = free hole concentration

$N_D{}^+$ = ionized donor like doping

$N_A{}^-$ = ionized acceptor like doping

R_n *(x)* and R_P *(x)* = electron and hole recombination rate

G(x) is the generation rate

J_N and J_P = electron and hole current densities.

Numerical analysis of solar cells is an imperative tool for improvement in design and to assess the practicability of the proposed physical structure and its performance. In this section, the SCAPS 1D simulation tool that was used to fit experimental data to develop a reference model will be presented. This allowed for further investigation into the effects doping has on the PCE of PSCs and improved the performance of the experimentally developed PSC.

4.6.1 SCAPS 1D

The Department of Electronics and Information Systems (ELIS) at the University of Gent in Belgium developed SCAPS (a Solar Cell Capacitance Simulator), a one-dimensional solar cell modeling tool. It is an open-source tool with various functions for assessing and enhancing solar cell performance. SCAPS diverse set of properties makes it an excellent choice for modeling perovskite solar cells [166]:

1. Structure of the solar cell: Perovskite solar cells often feature complicated multilayer structures of various materials. SCAPS 1D allows users to simulate and model the layered structure of perovskite solar cells precisely. This enables the variable definition of the numerous layers, thicknesses, and material properties.

2. Electrical simulation: SCAPS 1D uses complex electrical and optical models to forecast the behavior of perovskite solar cells. Charge carrier generation, recombination, and mobility inside the device can all be precisely reproduced. The solar cell's optical performance can also be investigated, with several optical characteristics, such as light absorption and reflection, taken into account.

3. Interface and contact effects: Interfaces and contacts significantly impact the performance of perovskite solar cells. By modeling such interactions, SCAPS 1D users can examine how the interfaces between different levels affect carrier recombination and transport. This also enables the simulation of the electrical characteristics of various contact materials.

4. Parameter extraction and optimization: Users can use SCAPS 1D parameter extraction and optimization tools to discover the material qualities and device attributes that best suit experimental data. This feature is extremely valuable for fine-tuning the simulation model to

accurately depict the behavior of perovskite solar cells in real-world applications.

5. User-friendly interface: SCAPS 1D user-friendly interface allows researchers, engineers, and anybody interested in solar cell technology to use it. It is not necessary to have prior experience with other simulation tools. The software's graphical user interface (GUI) simplifies simulation setup, device parameter definition, and simulation result viewing operations.

4.6.2 SCAPS 1D Front Interface

The simulation software's user interface is critical for users to engage with a tool and properly utilize its capabilities. Even though SCAPS 1D is largely accessed via a command-line interface, users can benefit from the program's powerful modeling and simulation capabilities, notably those for perovskite solar cells. It is easier to set up, execute, and analyze simulations with the help of SCAPS 1D various capabilities, giving researchers and engineers insightful data about the operation and performance of their products. In this section, the SCAPS 1D interface panel, also known as the action is depicted in Figure 4.9.

Section 1- This section of the action panel allows for the definition of the problem. This option was selected which defined the solar cell structure and material characteristics parameters, as illustrated in Figure 4.10. This part of the action panel also allows access to the simulation results selected from Section 2.

Section 2- The measurements to be simulated are selected in this section. The current voltage for direct current analaysis and the external quantum spectral response measurements was selected. The voltage (V_1) is set to zero, while the voltage (V_2) is set to two volts. The option to stop at

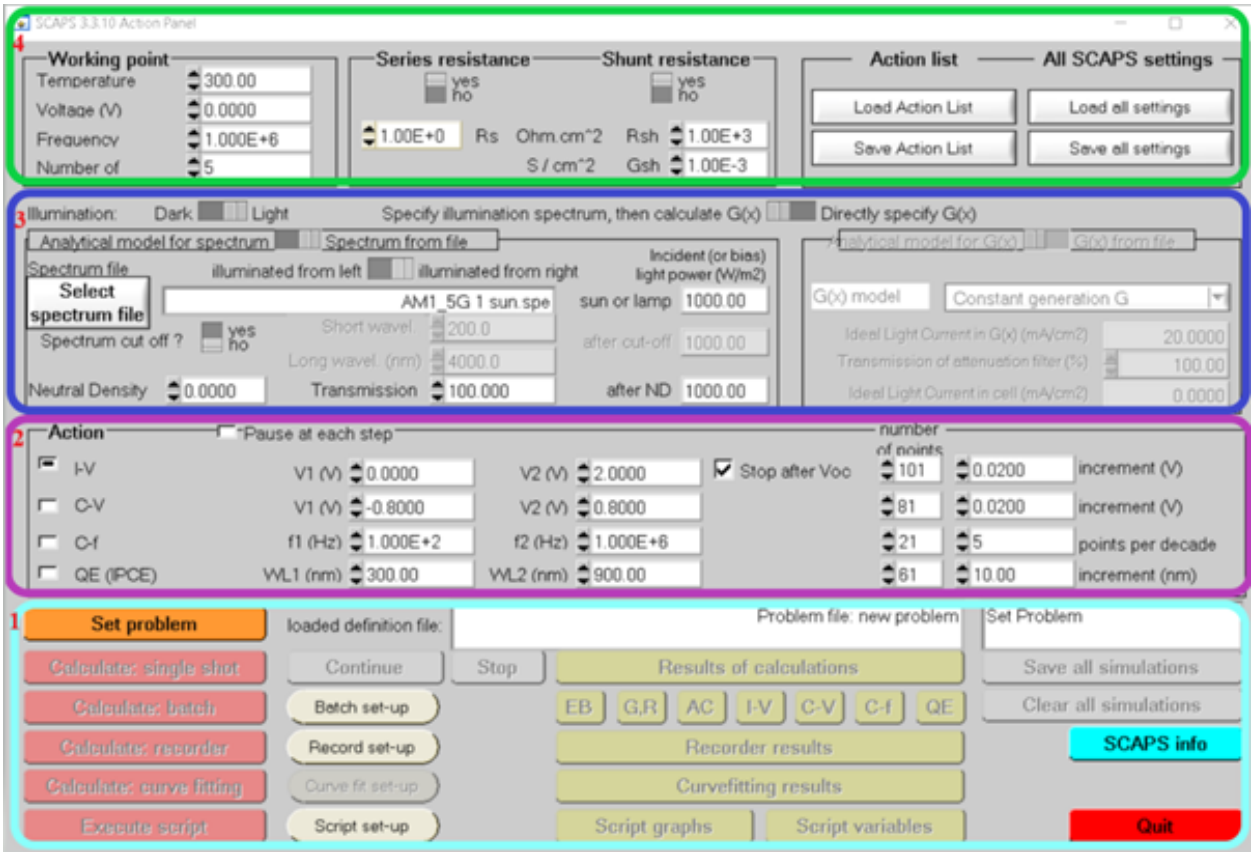

Figure 4.9 SCAPS 1D action panel

open circuit voltage (V_{OC}) is selected. Convergence failures are more likely to occur after the open circuit voltage.

Section 3- This section contains the illumination panel for adjusting the spectrum and the direction of sunlight entering the solar cell. The option of light entering the solar cell from left to right with 100% transmission at an intensity of 1000 W/ m^2 was selected.

Section 4- This section of the action panel displays the working point panel and allows the user to configure the operational circumstances under which the simulation will run. Configuring the

working temperature, voltage, frequency, series, and shunt resistances is possible. The working point temperature was set to 300 K at 0 V with the series and shunt resistance initially set to 1 and 3 $k\Omega.cm^2$ respectively. This portion of the action panel also includes the 'Action List' and 'All SCAPS settings.' Any action list or settings can be saved for future reference or loaded to use in the simulation.

4.6.3 SCAPS 1D Solar Cell Definition Panel

Once the front interface settings are complete, the perovskite solar cell model structure (FTO/Zn-TiO_2/$CH_3NH_3PbI_3$/Spiro-OmeTAD/Carbon) on the SCAPS 1D software can be defined by clicking the set problem option, which opens the solar cell definition panel interface shown in Figure 4.10. Section 1 allows loading saved SCAPS 1D files, saving already modeled structures, and creating a new structure. Section 2 provides for the setting of the front and back contacts and allows for up to seven layer structures to be defined. In section 3, the illumination is set to enter from the right-hand side, and the voltage is applied from the left-hand side. To add a layer, click on the add layer option.

Clicking on the add layer option will open the layer properties setting interface panel as shown in Figure 4.11. This is the main interface that allows for the parameter setting such as film thickness, bandgap, electron affinity, dielectric permittivity, conduction band effective density of states, valence band effective density of states, electron thermal velocity, hole thermal velocity, electron mobility, hole mobility, shallow uniform donor density, shallow uniform acceptor density, and interface defects and recombination. Once the parameter settings for each layer has been entered, the simulation setup is completed.

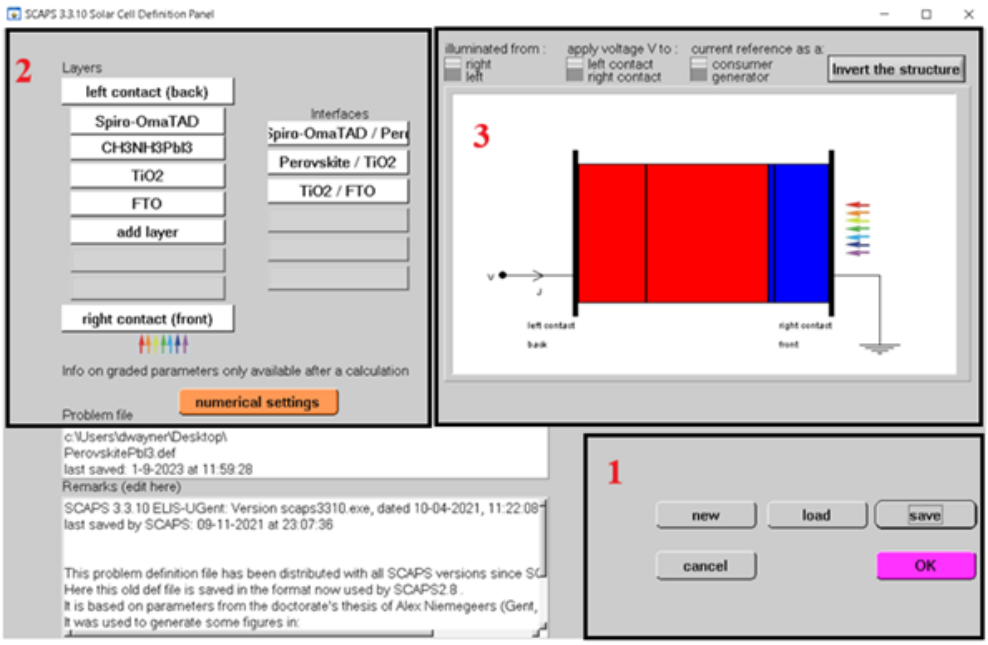

Figure 4.10 SCAPS 1D solar cell definition panel

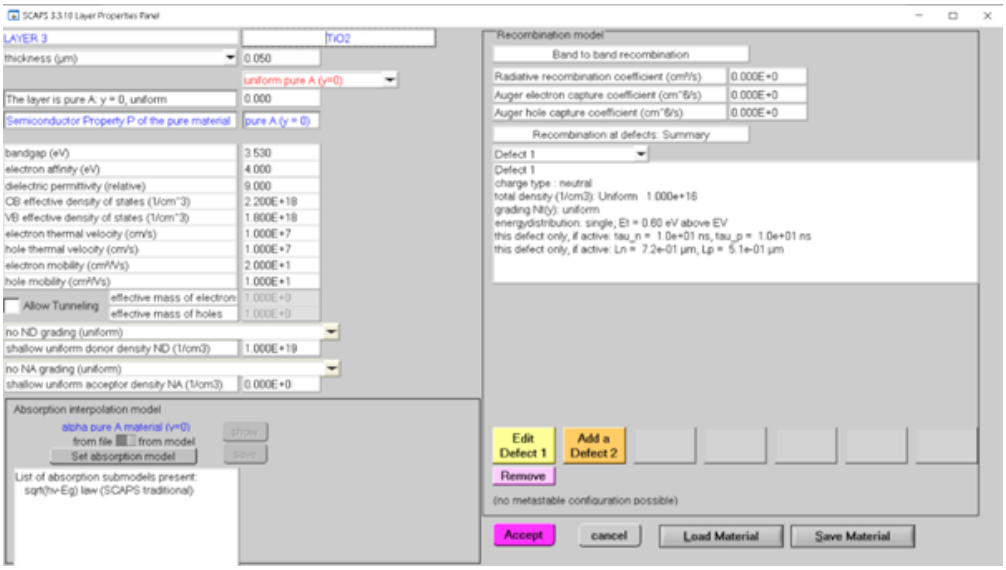

Figure 4.11 SCAPS 1D layer properties interface

4.7 SCAPS 1D Settings

The baseline parameter settings for the materials used for the electron transport layer, hole transport layer, absorbing layers, front and back contacts are indicated in Table 4.1.

The fabricated planar n-i-p structure perovskite device (FTO/ Zn-doped TiO_2/ $CH_3NH_3PbI_3$ /Spiro /carbon/ FTO) was simulated using the Solar Cell Capacitance Simulator (SCAPS 1D) software [167]. The simulation was performed at 300 K under one sun (AM 1.5 G, 100 mW cm^{-2}). The optical bandgaps of the FTO, ETL, and $CH_3NH_3PbI_3$ layer included in the simulation were determined from the Tauc plot in Section 5.5. Other parameters such as electron affinity, dielectric permittivity (relative), CB effective density of states, VB effective density of states, electron and hole thermal velocity, acceptor and donor doping densities, and defect densities were collected from literature as given in Table 4.1. The FTO front contact and carbon back contact work functions were taken as 4.4 [168] and 5 eV [169] respectively.

Table 4.1 Material layer settings.

Parameters	**FTO**	**TiO_2**	**$CH_3NH_3PbI_3$**	**SPIRO**
Thickness(μm)	0.1	0.05	0.9	0.05
Bandgap (eV)	3.5*	Experimentally fitted (3.53*,3.48*, 3.45*,3.38*, 3.41*)	2.030*	2.99
Electron affinity (eV)	4	4.1	3.9	2.05
Dielectric permittivity (relative)	9	9	6.5	3
CB effective density of states (1/cm^3)	2.2x10^{18}	2.2x10^{18}	1.8x10^{18}	2.5x10^{18}
VB effective density of states (1/cm^3)	1.8x10^{18}	1.8x10^{19}	1.8x10^{19}	1.8x10^{19}
Electron thermal velocity (cm/s)	10^7	10^7	10^7	10^7
Hole thermal velocity (cm/s)	10^7	10^7	10^7	10^7
Electron mobility (cm^2/V$_s$)	20	200	5x10^{-1}	2x10^{-4}
Hole mobility	1	100	5x10^{-1}	2x102^{-4}
Shallow uniform donor density N_D(1/cm^3)	2x10^{19}	2x10^{19}	0	0
Shallow uniform acceptor density N_A(1/cm^3)	0	0	10^{15}	10^{19}
Defect density N_t (1/cm^3)	10^{13}	10^{16}	10^{16}	10^{19}
References	[170]	[170–172]	[173–175]	[176–178]

Chapter 5

EXPERIMENTAL RESULTS

This chapter aims to study the effects of doping TiO_2 with Zinc on ETL material properties and the performance of PSCs. Experimental characterization, including XRD, FTIR SEM, TEM, UV-Vis, Photoluminescent, and J-V characterization, is presented and analyzed.

5.1 X-Ray Diffraction

For nanoparticles, XRD is typically employed to identify the crystal phase structure and estimate crystallite size as well as crystallinity [179, 180]. The XRD results of perovskite films annealed at 65°C for 30 s and then annealed at 100°C for 30 s, 1 min, and 2 minutes are presented in Figure 5.1. Strong peaks at 14.06° (110), 28.15° (220), and 31.68° (312) indicate the formation of tetragonal perovskite ($CH_3NH_3PbI_3$) phase [181, 182] with high crystallinity for the samples annealed for 30 s and 1 min. According to Figure 5.1, the lead iodide phase in the XRD pattern of the sample annealed for 30 s may be due to the residual phase from preparation, which remains within the bulk

of the material. In other words, the annealing time was insufficient to convert the precursors to the perovskite phase completely. For the sample annealed for 2 min, the peaks at 13.59° (001), 27.58° (101), 30.49° (102), 43.52° (111), 50.17° (201), and 73.57° (105) correspond to hexagonal lead iodide phase (JCPDS No. 07-0235) [183]. The PbI_2 phase is formed due to the decomposition of the perovskite phase upon annealing at 100 °C, where methyl ammonium iodide (CH_3NH_3I) breaks away from the perovskite film to form lead iodide by heating for a longer time (2 min). It was found previously that during the annealing process, CH_3NH_3I can break away if annealed too long, especially for some loosely bonded perovskite phases [184, 185].

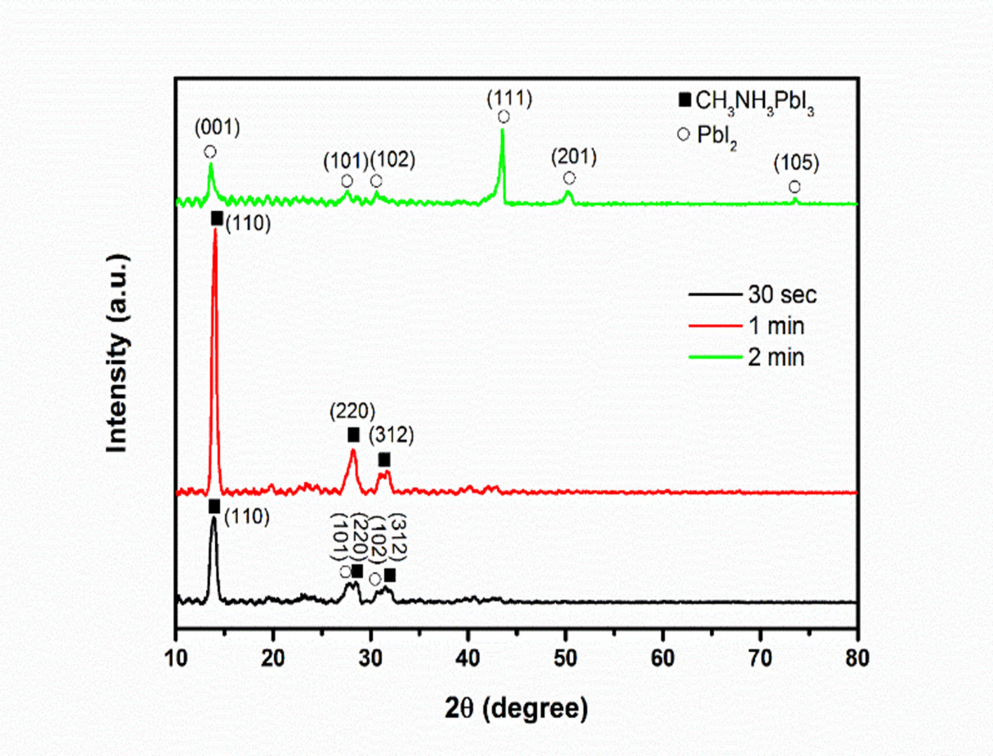

Figure 5.1 XRD patterns of Perovskite thin films annealed at 65^{o}C for 30 s and 100^{o}C for 30 s, 1 min, and 2 min

The average crystallite size of the under-studied samples was calculated by resolving the characteristic peaks using Equation (4.2). The crystallite size for the perovskite phase was equal to 14.32 nm and 19.99 nm for the samples annealed at 65^{o}C for 30 s and 100^{o}C for 30 s and 65^{o}C

for 30 s and 100^{o}C for 1 min, respectively. In addition, the crystallite size of the PbI_2 phase in the sample annealed at 65^{o}C for 30 s and 100^{o}C for 2 min was 12.21 nm. The more intense characteristic peaks and larger average crystal size after 65^{o}C for 30 s and 100^{o}C for 1 min annealing time attributed to the improved crystallinity or composition homogeneity with fewer low-dimensional defects and less scattering between grain boundaries in the solvent-annealed perovskite film.

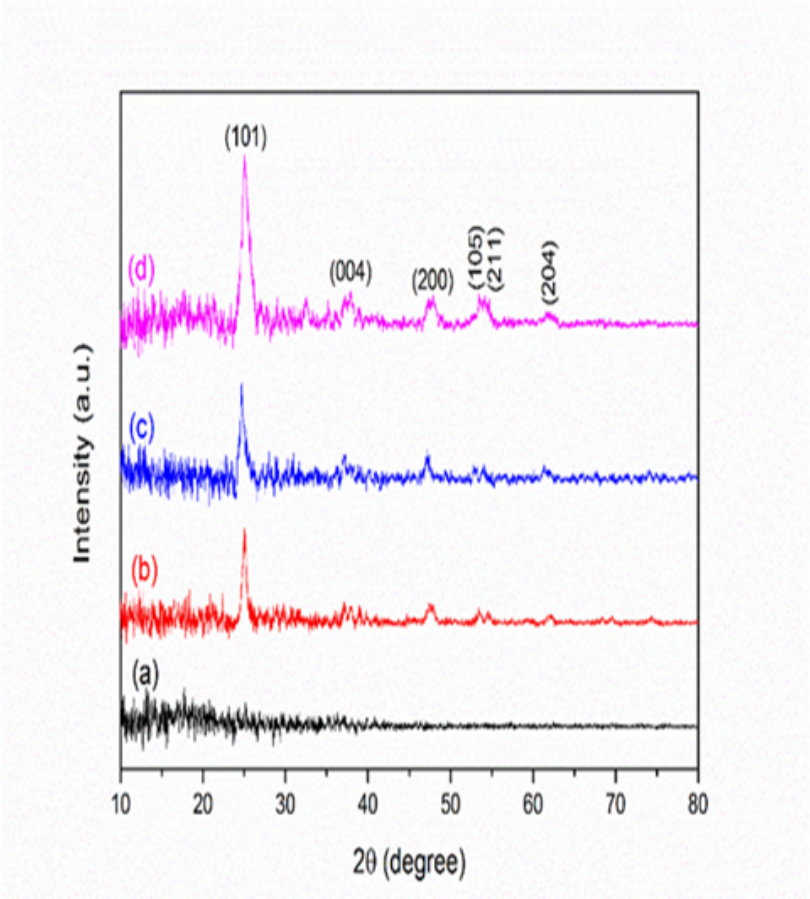

Figure 5.2 XRD patterns of Zn-TiO_2 powder samples doped with (a) 0.5 mol%, (b) 1 mol%, (c) 2 mol%, and (d) 5 mol%

.

Figure 5.2 shows the XRD patterns of Zn-TiO_2 powder samples doped with a Zn molar percentage doping of 0.5%, 1%, 2%, and 5%. The XRD peaks at $2\theta = 25.1^o$ (101), 37.8^o (004), 47.1^o (200), 53.4^o (105), 54.5^o (211), and 61.8^o (204) are typically characterized as the typical diffraction

peaks of the anatase crystal phase of tetragonal titanium dioxide structure (JCPDS No. 21-1272) with excellent surface performance [186]. All Zn-TiO_2 samples show a pure anatase phase with no rutile phase or ZnO phase. Due to the low Zn content, no additional diffraction peaks associated with ZnO develop even at the greatest Zn dopant concentration (5 mol%). Furthermore, Figure 5.2 shows that the sample doped with 0.5% Zn was largely amorphous, and the half-width of the peak (101) plane increases slightly as the doped Zn amount increases, indicating that the degree of crystallinity of samples, as well as crystallite size, decreases while the surface defect content increases. This could be attributed to the slight inhibition of TiO_2 crystal formation by Zn doping during the heat treatment process[187]. The peak intensity of the (101) plane increases with increasing Zn doping up to 5%, which can be attributed to the influence of Zn^{2+} on the TiO_2 lattice structure, as previously found by Arunachalam et al. [188]. Additionally, with Zn ion insertion, XRD patterns exhibited a slight shift to lower angles because the ionic radius of Zn^{2+} (i.e., 0.074 nm) is greater than that of Ti^{4+} (i.e., 0.061 nm). It suggests that Zn^{2+} may enter the TiO_2 lattice or interstitial site [189]. The phase composition of Zn-doped TiO_2 films is shown to be dependent on dopant concentration. The crystallite size (D) for the samples containing 1%, 2%, and 5% Zn was $\sim$ 12.7, 10.8, and 7.1 nm, respectively, as determined by equation (4.2) from the half width (β) of the peak at $2\theta = 25.1^{o}$.

5.2 Fourier Transform Infrared Spectroscopy

FTIR spectroscopy using the Agilent Cary 60 was conducted to identify $CH_3NH_3Pb_2I$ formation. The FTIR spectra in Figure 5.3 feature vibrational modes at 3116 cm^{-1} (N-H stretch), 3116- 1569 cm^{-1} (C-H stretch), 1569 cm^{-1} (antisymmetric $NH_3{}^{+}$), 1458 cm^{-1} (symmetric NH_3+bend), 1015 cm^{-1} (MAI·PbI_2, DMSO), 950 cm^{-1} (C-N stretch) and 907 cm^{-1} (NH_3+/CH_3 rock) which is

similar to related literature [187–189]. The adduct of Pb_2 with DMSO and Methyl Ammonium Iodide (MAI) was confirmed by FTIR spectroscopy at 1015 cm^{-1} [190, 191].

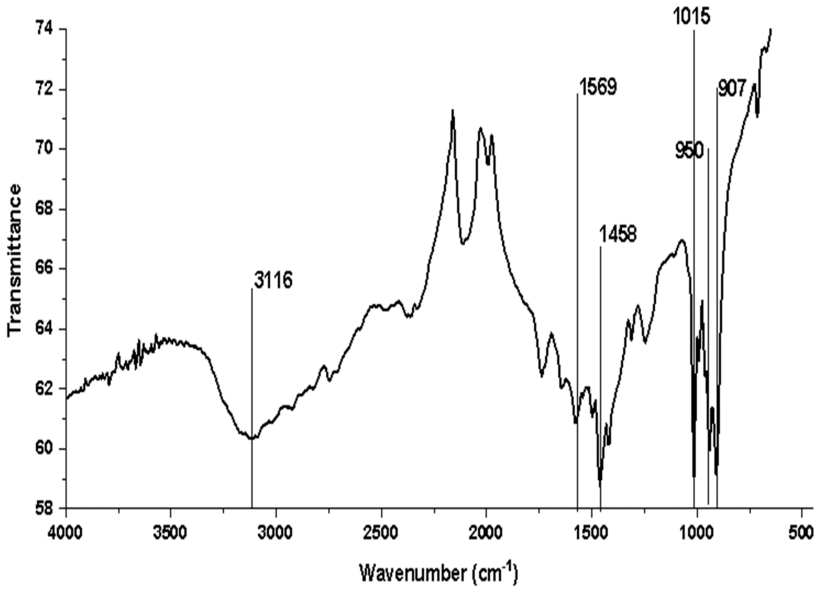

Figure 5.3 FTIR spectra of perovskite thin film

The FTIR measurement of undoped and Zn-doped TiO_2 nanoparticles calcined at 550°C is shown in Figure 5.4. The absence of O-H hydroxyl groups in the wavenumber range 3100-3600 cm^{-1} can be explained by the high calcination temperature of 550°C and the elimination of hydroxyl groups. The interactions of the hydroxyl groups with the NH_4 and CH_3 in the perovskite could reduce the performance of the PSC, resulting in the breakdown of $CH_3NH_3PbI_3$ into PbI_2 and CH_3NH_3I [192]. Sharp peaks related to O-Ti-O bonding between 528 and 408 cm^{-1} indicate that the nanoparticles are crystalline. The prominent peak at 438 cm^{-1} is typical of Zn-doped-TiO_2 anatase [192–198].

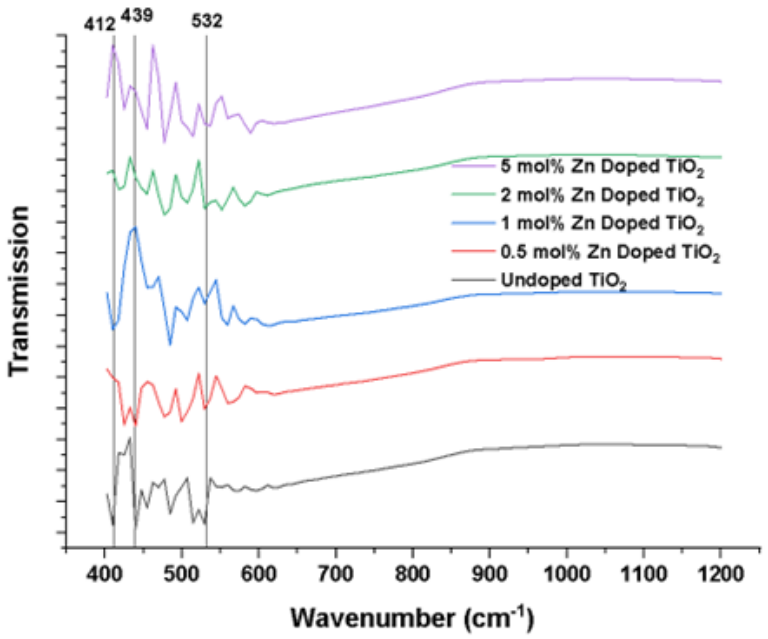

Figure 5.4 FTIR results of Zn-doped TiO_2 nano particles annealed at 550°C

5.3 Transmission Electron Microscope

The synthesized nanoparticles' size and shape were further investigated by TEM and are shown in Figure 5.5(a-e), which shows the morphology and size distribution of the TiO_2 nanoparticles ranging from 15 to 20 nm. The Zn-doped TiO_2 exhibits a homogeneous spherical morphology. The TEM results summarised in Figure 5.5(f) illustrate an increase in the particle size from 15.91 nm for undoped TiO_2 to 20.31 nm for 5 mol% Zn-doped TiO_2; this could be attributed to the incorporation of Zn ions into the TiO_2 lattice structure [199, 200]. The larger particle size reduces the bandgap and recombination sites in the ETL layer as the space between the valence and conduction bands narrows and electron–hole pairs are further apart, and the effect of the coulomb interaction between them is reduced [201, 202]. This is confirmed by the Tauc plot in Figure 5.12, which shows bandgap narrowing up to 2 mol% Zn doping as the particle size increases.

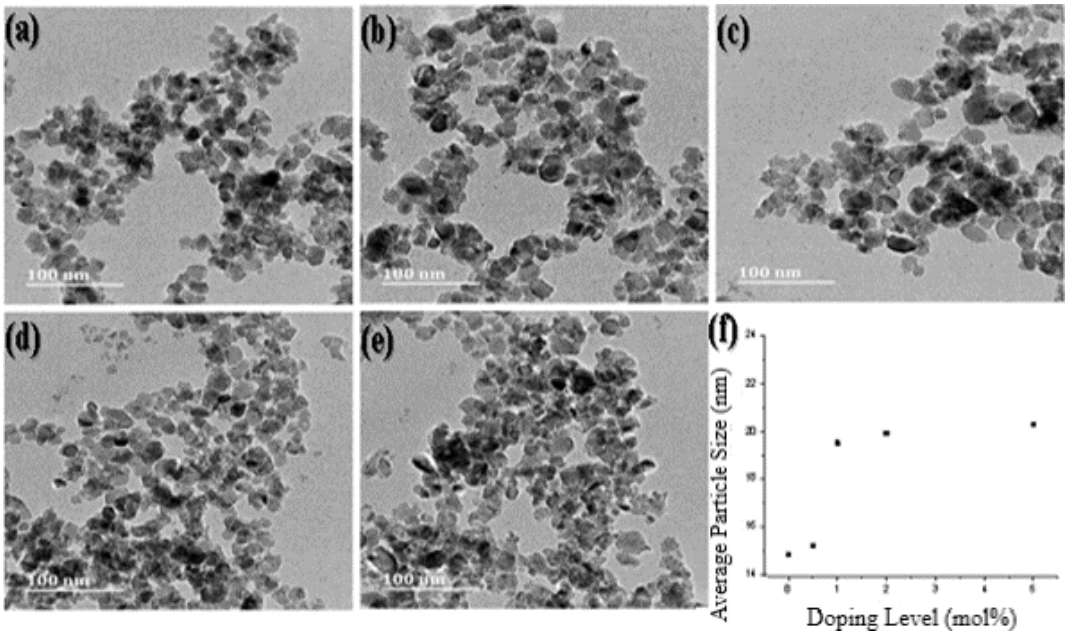

Figure 5.5 TEM images of (a) undoped TiO_2 (b) 0.5 mol% (c) 1 mol% (d) 2 mol% (e) 5 mol% (f) average particle size vs doping %

5.4 Scanning Electron Microscope and EDX

SEM was used to examine the morphology of the TiO_2 and Zn-doped TiO_2 thin films after annealing at 550° C for 30 minutes. The top view of the SEM images of the TiO_2 and Zn-doped TiO_2 layers is shown in Figure 5.6(a-e). A porous and fairly uniform surface covering with no discernible pinholes is created on the surface. A dense, pinhole-free layer enables fast electron movement in the PSC by blocking holes and reducing recombination [203, 204]. The Zn-doped TiO_2 nanoparticles on the surface exhibit an irregular morphology and a conical shape. According to the SEM images, TiO_2 nanoparticle instability results in agglomeration, which causes the particles to bond. The aggregation of the nanoparticles is further illustrated by the SEM images showing the formation of clusters which appears to reduce upon increasing Zn doping concentration. This could also be attributed to the decrease in crystallite size upon increasing Zn doping observed by the XRD characterization.

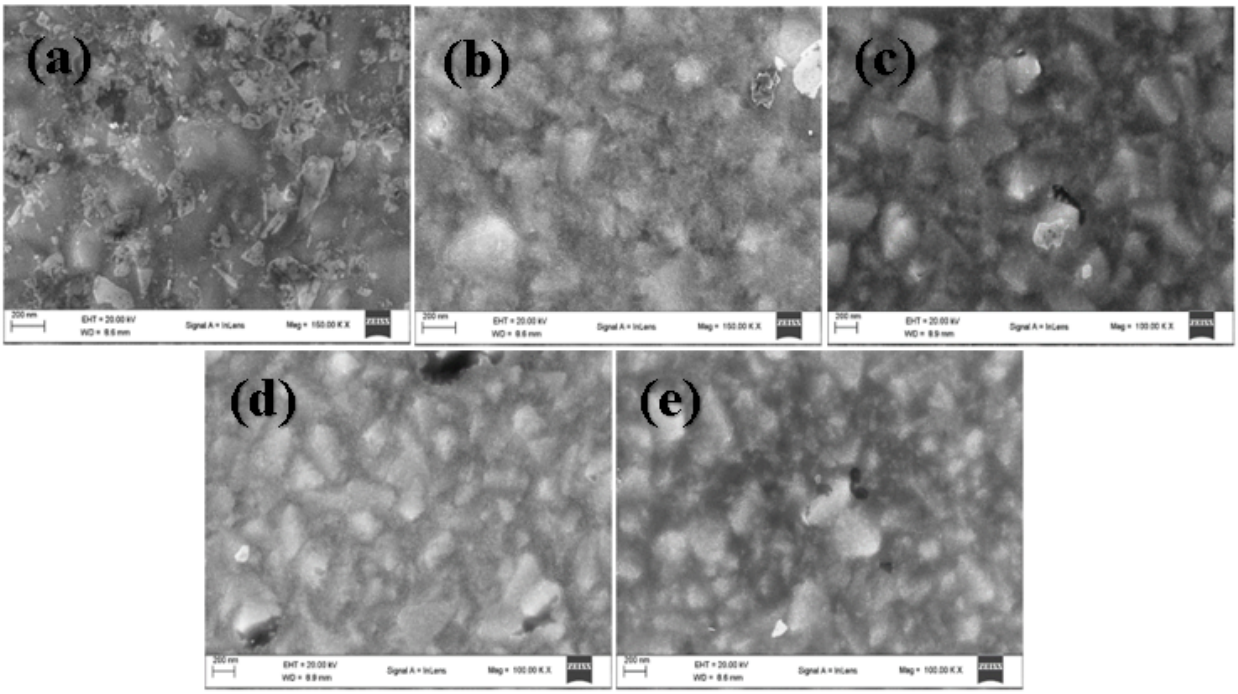

Figure 5.6 SEM images of the (a) undoped TiO_2 (b) 0.5 mol% (c) 1 mol% (d) 2 mol% (e) 5 mol%

The surface profiles and the root mean square (Rq) values shown in Figure 5.7 indicate the surface roughness of the samples. Figure 5.7(f) shows the highest surface roughness of 26.85 nm for the undoped TiO_2 sample and the lowest surface roughness of 23.4 nm for the 5 mol% Zn-doped TiO_2 layer. It can be seen that the surface roughness rate decreased gradually with increasing Zn doping concentration from 0 to 5 mol%. The decrease in surface roughness and smoother surfaces could be due to less aggregation upon the addition of Zn ions into TiO_2. The surface smoothness of the Zn-doped TiO_2 compact layer has a critical role in the electron transport behavior by providing an improved surface interface for the deposition and annealing of the perovskite layer, which is essential for improving the performance of PSC .

Energy dispersive X-ray spectrometry analysis of Zn-doped TiO_2 thin films was performed using a Zeiss scanning electron microscope to determine and identify the elemental composition

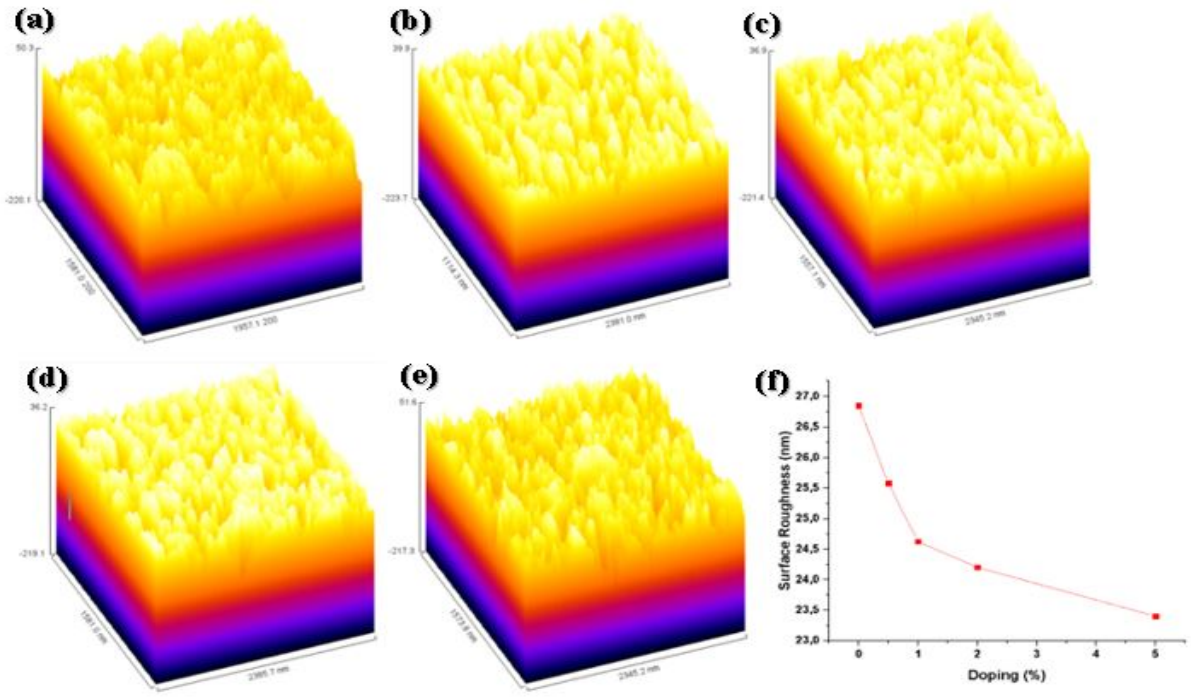

Figure 5.7 Surface roughness of (a) undoped TiO_2 (b) 0.5 mol% (c) 1 mol% (d) 2 mol% (e) 5 mol% (f) surface roughness vs doping %

and concentrations of the FTO\ Zn- TiO_2 layers and is shown below in Table 5.1. It can be seen that the wt% of Zn increases from 0 to 1.08 as the molar percentage concentration increases from 0 to 5 mol %. Figure 5.8 (a-e) shows peaks for Ti, O, Zn, Sn, and Si; no other impurities are seen. The spectra include small carbon peaks, which may be due to the presence of carbon tape fixed on the SEM stub during characterization. Overall, the EDX spectra indicate crystalline synthesis of Zn-doped TiO_2 nanoparticles.

The SEM image of the $CH_3NH_3PbI_3$ thin film presented in Figure 5.9(a) shows non-uniform, dense, and fairly well-interconnected layers with particle sizes ranging from 50 nm to 800 nm with an average particle size of 397 nm shown in Figure 5.9(b). The dense, flat, and semi-transparent $CH_3NH_3PbI_3$ thin film was formed due to the rapid evaporation of DMF caused by depositing an anti-solvent consisting of diethyl ether during the last 5 seconds of the spin coating cycle. Anti-solvents have a critical role in controlling annealing time, and particle size in improving

Table 5.1 Elemental composition and wt % concentrations of the FTO Zn- TiO_2 layers.

Sample	C	O	Si	Ti	Zn	Sn
Spectrum 1: Undoped TiO_2	0	27.2	2.75	3.05	0	66.9
Spectrum 2: 0.5 mol%-Zn DopedTiO_2	2.11	29	2.33	3.95	0.29	62.3
Spectrum 3: 1 mol%-Zn Doped TiO_2	2.56	27.1	2.5	3.85	0.38	63.5
Spectrum 4: 2 mol%-Zn Doped TiO_2	2.02	27.9	2.79	3.82	0.49	62.9
Spectrum 5: 5 mol%-Zn Doped TiO_2	1.74	28.8	2.22	3.24	1.08	62.8

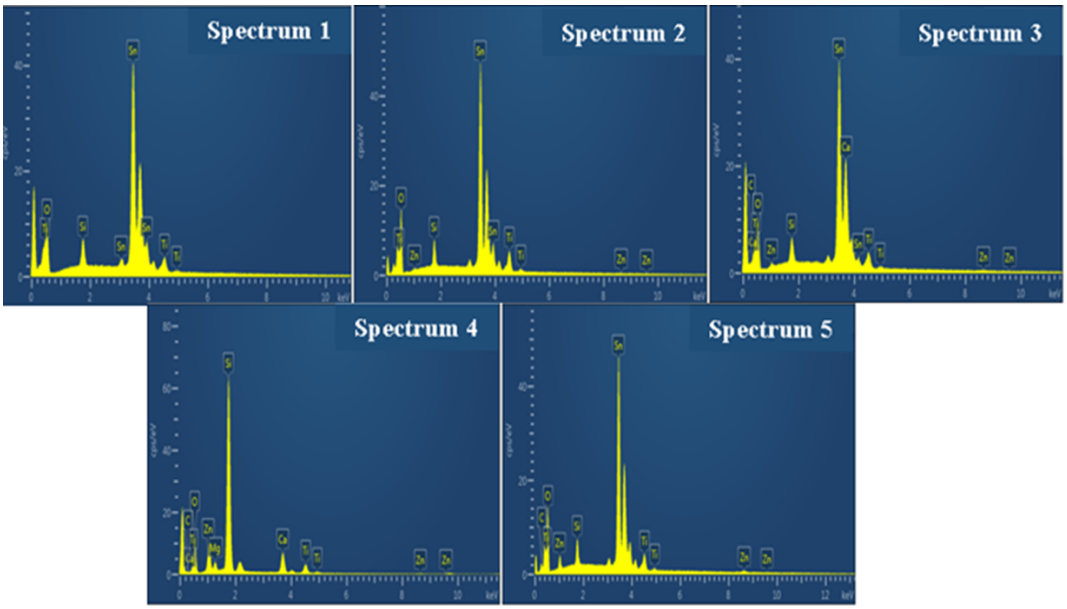

Figure 5.8 Elemental weight percentage compositions of (a) undoped TiO_2 (b) 0.5 mol% (c) 1 mol% (d) 2 mol% (e) 5 mol%

the perovskite layer surface morphology. When di-ethyl ether was omitted and perovskite precursor solution annealed under the optimized duration and temperature settings, the films were opaque, with a dark grey almost lead appearance with a visibly rough surface morphology. Such a surface morphology is not suitable for the development of efficient thin-film solar cells. Hence anti-solvents are necessary to ensure the full conversion of the precursor solution to perovskite

and improve the development of dense flat films. The spin-coated film has a root mean square surface roughness of approximately 27.26 nm shown in Figure 5.9(c). The roughness could be due to the non-uniformity and pinholes observed in the SEM images. However, improved deposition techniques such as vapor deposition could improve surface coverage and uniformity.

Energy dispersive X-ray analysis of FTO/TiO_2/ $CH_3NH_3PbI_3$ thin films was performed to determine and identify the elemental composition and weight percentage (wt %). Figure 5.9(d) shows peaks for Ti, O, Sn, I, and Pb. The presence of Si is due to the FTO-coated quartz substrate used; no other impurities are seen.

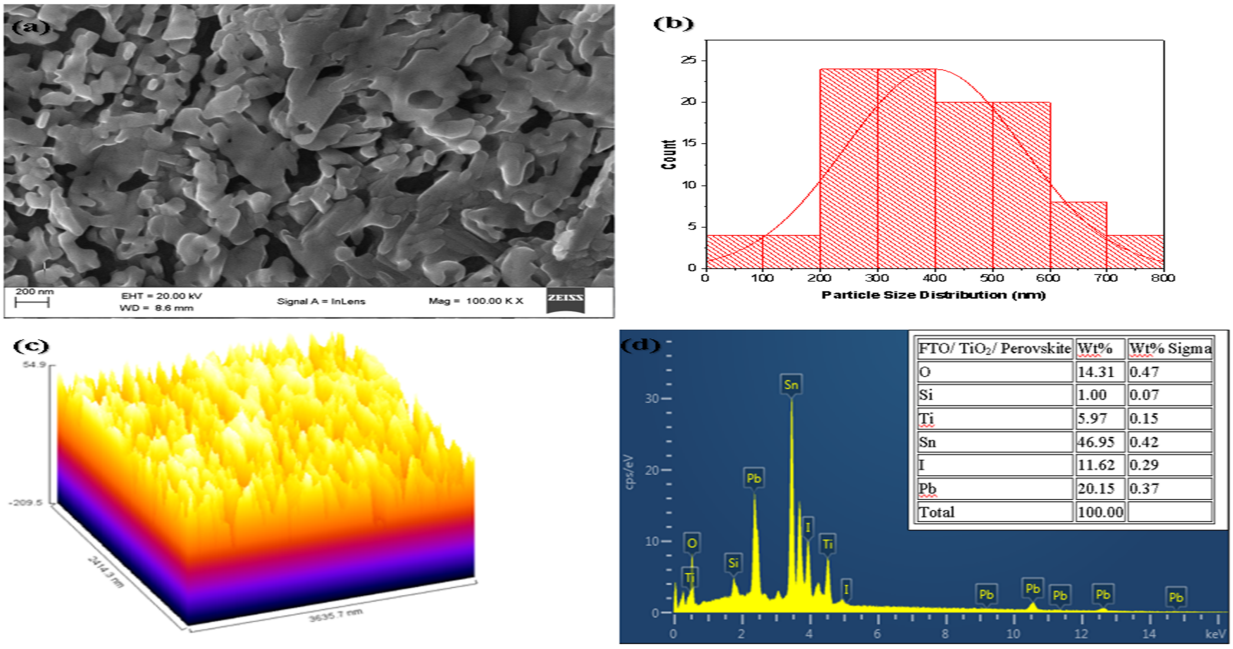

FTO/ TiO_2/ Perovskite	Wt%	Wt% Sigma
O	14.31	0.47
Si	1.00	0.07
Ti	5.97	0.15
Sn	46.95	0.42
I	11.62	0.29
Pb	20.15	0.37
Total	100.00	

Figure 5.9 (a) SEM image of the Perovskite surface layer (b) Perovskite particle size distribution (c) Surface plot of Perovskite layer (d) Elemental composition of the FTO/ TiO_2/ Perovskite layers

5.5 UV-Vis Spectroscopy

The Cary 60 UV-Vis was used to collect UV-Vis transmission and absorption spectra. The UV-Vis transmission spectra of various TiO_2 and Zn-doped TiO_2 thin films coated on FTO substrates are shown in Figure 5.10. The transmission intensity of the Zn-doped TiO_2 thin film samples decreased between 380 and 550 nm when compared to the undoped TiO_2 sample; between 550 and 800 nm a slight improvement is observed for the 2 mol% Zn-doped sample, other than that, there is no discernible variation in transmission intensity. The transmission spectra of between 65 - 70% over this region show a slight light loss when compared to the transmittance of the FTO substrate of between 70 - 80%. The slight improvement in optical transmission exhibited by the 2 mol% Zn-doped TiO_2 could be due to a decrease in surface roughness by the incorporation of Zn ion into the TiO_2 lattice structure [205, 206], improvement in optical transmission will directly increase the light absorption of the perovskite film.

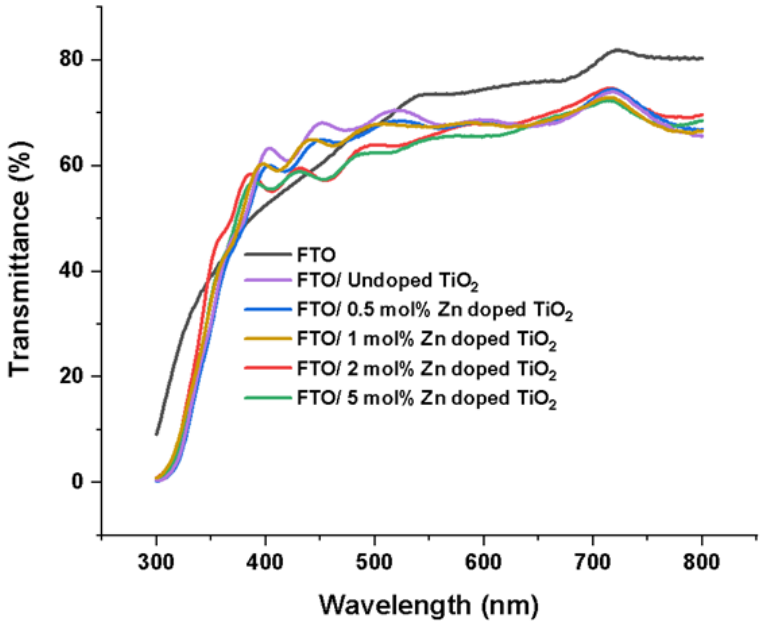

Figure 5.10 Transmission spectra of undoped and Zn-doped TiO_2

The absorption spectra of TiO_2, Zn-doped TiO_2, and TiO_2/ perovskite samples are shown in Figure 5.11. There are very slight variations in the optical absorption from 300 nm to 800 nm for the Zn-doped samples. The perovskite films show strong light-absorbing properties from an optical onset of 800 nm. The excellent absorption properties could be attributed to the dense surface coverage and uniformity of the perovskite film.

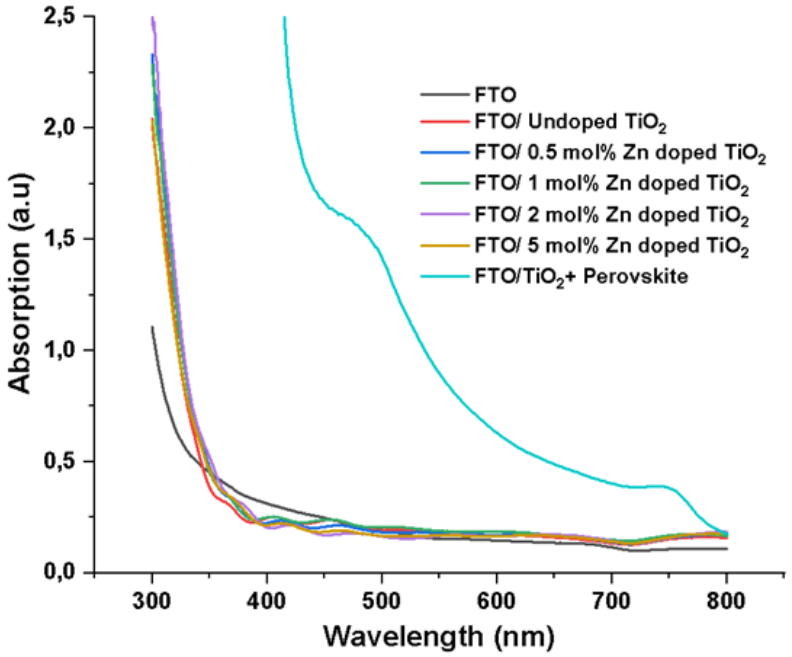

Figure 5.11 Absorption spectra of undoped and Zn-doped TiO_2

The band gap of the undoped TiO_2, Zn-doped TiO_2, and the perovskite layer was determined by plotting $(a/hv)^2$ as a function of photon energy, and extrapolating the linear region of the absorption curve as shown in Figure 5.12. The bandgap of the perovskite layer was determined to be 2.03 eV. The bandgaps of undoped TiO_2 and 0.5, 1, 2, 5 mol% Zn-doped TiO_2 are respectively 3.53, 3.48, 3.45, 3.38, and 3.41 eV. As the mol% Zn doping concentration increased from 0 % to 5 %, the band gap gradually decreased from 3.53 eV for the undoped samples up to 3.38 eV for 2 mol%, then increased by 0.03 eV for the 5 mol% when compared to 2 mol%. By increasing

Zn doping concentration, the band gap of Zn-doped TiO_2 compact layers decreases and introduces a new band in the TiO_2 bandgap. Previous results indicate that bandgap narrowing can shift the Fermi energy level up and lower the position of the conduction band, which can improve electron injection from the perovskite layer to the Zn-doped TiO_2 compact layer [202].

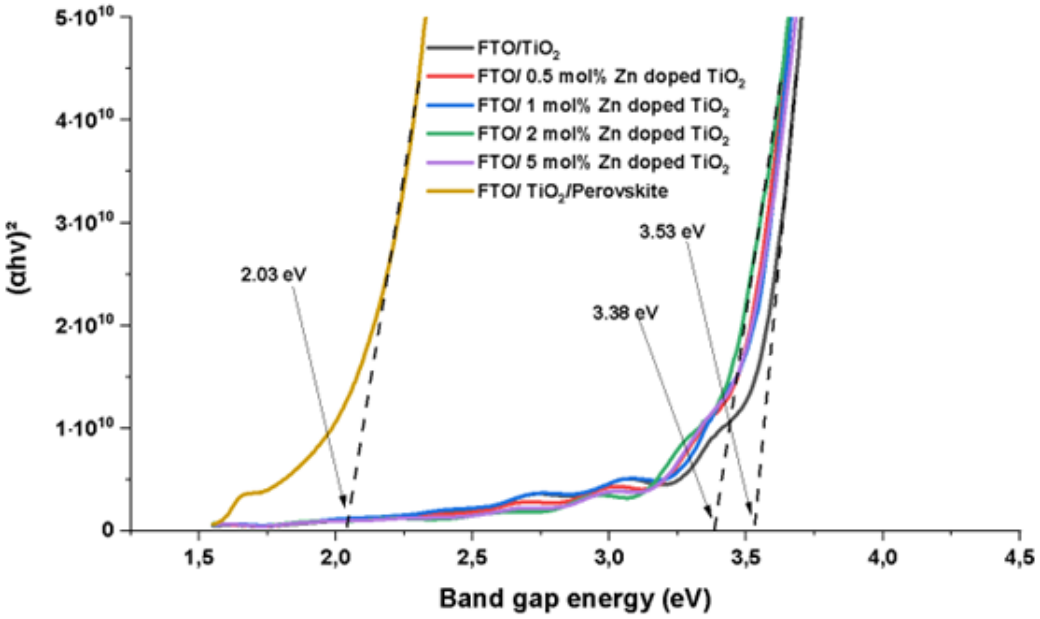

Figure 5.12 Tauc Plot

5.6 Photoluminescence

To gain insight into the charge transfer kinetics within the TiO_2 and Zn-doped TiO_2 perovskite thin films, photoluminescence intensity measurements recorded at room temperature (300 K) was done using the Perkin Elmer Lambda 35 UV/Vis spectrometer. The excitation wavelength of 525 nm produced a photoluminescence peak at 735 nm (1.69 eV) corresponding closely to the bandgap of the perovskite film. The peak position is slightly lower (0.37 eV) than the bandgap value (2.06 eV)

estimated from the Tauc plot but relatively close to the bandgap value of 1.6 eV reported by Kong et al for the tetragonal structure of $CH_3NH_3PbI_3$ [207]. The tetragonal structure of $CH_3NH_3PbI_3$ was also identified from XRD analysis shown in Figure 5.1. According to the corresponding shape on the PL spectra for the undoped and doped TiO_2 films, Zn doping does not introduce additional PL signals. The broad photoluminescence peak observed at 735 nm is a result of the the radiative recombination of electrons and holes near the band edges[208]. This depicts the direct bandgap nature of the $CH_3NH_3PbI_3$ film. In materials with a direct bandgap, the recombination of charge carriers leads to the emmission of photons and in this case, it occurs at 735 nm. Additionally, Figure 5.13 shows a decrease in PL intensity from the undoped TiO_2 to the Zn-doped TiO_2, with 2 mol% and 5 mol% Zn-doped TiO_2 showing the strongest PL quenching indicating electrons can be effectively transferred from the perovskite layer to TiO_2 thus resulting in faster charge transfer kinetics and less recombination. The low emission intensities of the Zn-doped TiO_2 films confirm that Zn doping can reduce electron-hole recombination reactions.

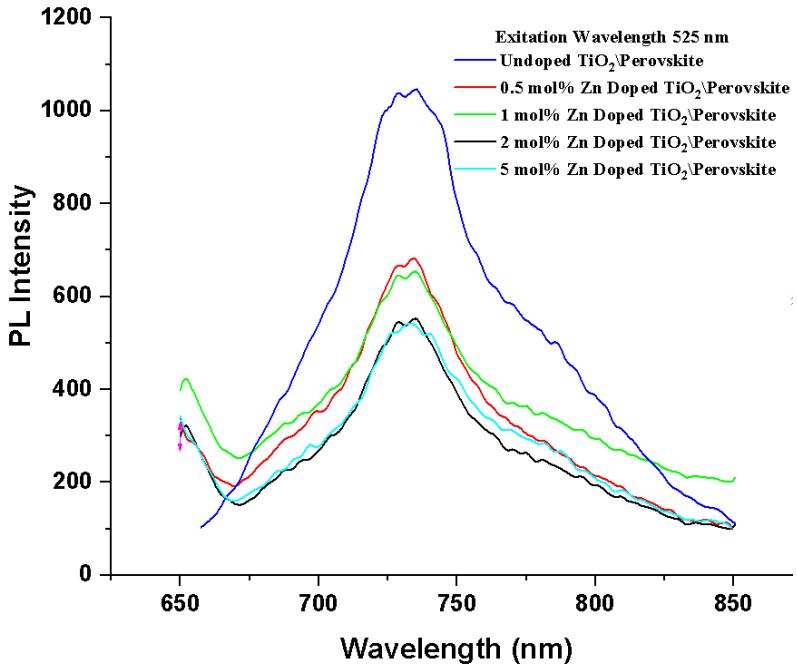

Figure 5.13 Photoluminescence spectra of undoped and Zn-doped TiO_2

5.7 Photovoltaic Properties

The J-V curves and best performance of the various PSCs developed are shown in Figure 5.14. The open circuit voltage slightly improved from 0.90569 V to 0.92774 V when the Zn doping concentration increased. Adding Zn ions into the TiO_2 lattice structure raises the CB toward the absorber's LUMO level and enables electron injection from the absorber into the compact layer. When compared to undoped TiO_2, the lower conduction band of Zn-doped TiO_2 improves electron injection from the perovskite to the ETL layer and electron transport rate.

Doping (%)	Voc (V)	Jsc (mA/cm²)	FF (%)	PCE (%)
0	0.90569	12.21851	48.0502	5.199
0.5	0.90981	12.22852	48.4989	5.3266
1	0.91082	12.23811	48.7714	5.4364
2	0.92774	12.25594	49.4823	5.675
5	0.9231	12.2387	49.226	5.5648

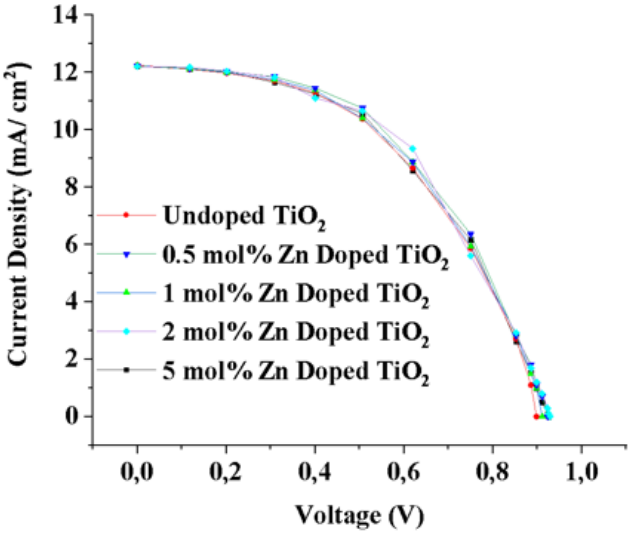

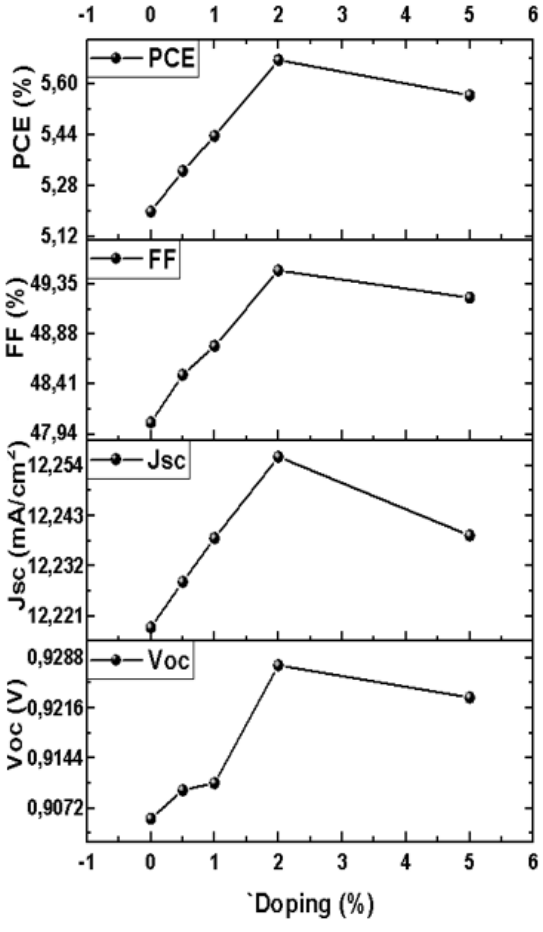

Figure 5.14 PV characteristics of TiO_2 and Zn-doped TiO_2 PSCs

Due to bandgap narrowing and improved charge transport, the J_{SC} increased from 12.21851 mA/ cm^2 to 12.25594 mA/ cm^2 when Zn doping concentration increased from 0 to 2 mol%. The best PCE of the perovskite solar cell with undoped TiO_2 was 5.199%. As Zn doping concentrations were increased to 2 mol%, the PCE increased to 5.675% and FF from 48.0502% - 49.4823%. The PSC with 5 mol% Zn-doped TiO_2 has a slightly lower V_{OC}, J_{SC}, FF, and PCE. The PCE decreased slightly to 5.5648% when compared with 2 mol% Zn-doped TiO_2. A possible reason for the reduction in the efficiency of cells with a doping level of 5 mol% is that this doping level moves the CB of the ETL by $\sim$0.03 eV upward. The electron injection from the absorber layer toward the ETL may be made easier by the proximity of the CB of the ETL to the LUMO of the absorber layer. However, when the CB goes higher, it moves away from the CB of the FTO layer. As a result, it would raise the recombination rate within the ETL while decreasing electron injection from the CB of the ETL to the CB of the FTO layer. Additionally, the efficiencies are lower than reported values because the PSC performance could have been affected by the humidity under the ambient conditions of fabrication and characterization including the instability of the single cation of perovskite $CH_3NH_3PbI_3$.

SCAPS 1D numerical simulation was used to further investigate the influence of ion doping on the performance of perovskite solar cells and better understand the difference in PSC performance and behavior at the ETL/perovskite interface.

Chapter 6

NUMERICAL RESULTS

This chapter focused on including experimentally obtained values into SCAPS 1D to develop a reliable reference model for numerical analysis. This allowed for further investigation and analysis into the effects of ion doping on the ETL and absorber layer. We also showed that the PSC device performance can be enhanced by improving bandgap alignment by doping and adding an interfacial layer at the absorber/ ETL interface.

6.1 Introduction

In this section, a reference model was developed to study the effects of ETL donor concentration doping, absorber acceptor concentration doping, and adding an interfacial layer between the absorber/ETL interface. The reference model was developed from the experimentally obtained bandgap values for the ETL and absorber layers.

Ideal devices built without considering the effect of series and shunt resistance do not accurately match the experimental performance. However, they reflect the influence of physical parameter variations such as bandgap, doping density, and film thickness. The development of ideal devices is challenging to reproduce accurately using the spin coating method of fabrication; however, improved fabrication techniques employed by Husainat et al known as concurrent multi-beam multi-target pulsed laser deposition, have significantly reduced the margin of error for photovoltaic parameters [209]. Adding experimentally obtained series and shunt resistance to SCAPS 1D allows us to more accurately match the simulation and experimental performance data gathered in this study to develop a reliable reference model. The validation of the software tool used allows for further investigation into the effects of ETL and absorber layer doping concentration, absorber bandgap variation, and the effect of adding an interfacial layer to enhance the performance of the PSC.

6.2 Reference Model Results and Discussion

Firstly, ideal perovskite devices are simulated without considering the series and shunt resistance responsible for electrical losses. Although ideal devices are unrealistic, they serve as a good base to evaluate the higher limits of device performance when considering an optimization approach.

Figure 6.1 displays the simulated PV characteristics of the five ideal Zn-doped TiO_2 (0, 0.5, 1, and 2 mol% Zn-doped TiO_2) PSC devices and is tabulated in Table 6.1 for comparison with the experimentally developed PSC. As expected, the experimentally developed PSC performance from Section 5.7 is less than the simulated performance for the five devices. This is because ideal devices were simulated and compared against experimental non-ideal devices. One of the reasons for this observation could be associated with the instability of $CH_3NH_3PbI_3$ [210].

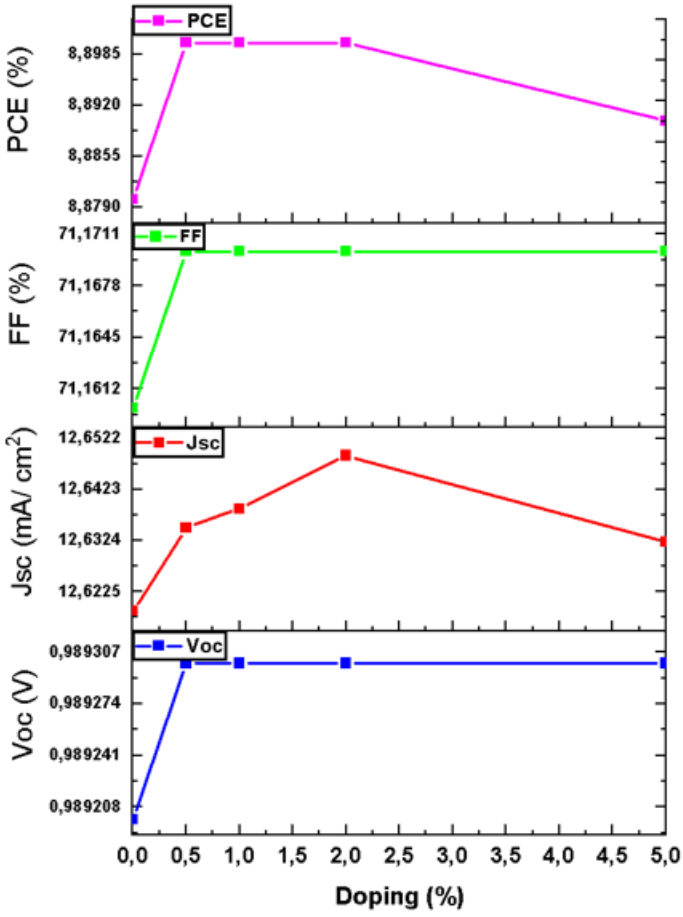

Figure 6.1 Ideal simulation of PV performance characteristics for fabricated PSC

Experimental performance testing was carried out 24 hours after the HTL was deposited and carbon contact applied; this was done to allow the Spiro-OmeTAD layer sufficient time to oxidize. Under these fabrication conditions, minor defects to the perovskite layer are a challenge to avoid. Additionally, the humidity level of the laboratory is associated with void formation in the active absorber layer, which is responsible for the gradual degradation of the active layer properties, resulting in lower PCE. The experimental devices suffer from phenomena such as defect states (at the surface and interface), which lead to charge recombination or current leakage, which introduces series and shunt resistances.

Next, we introduce and analyze the effects of series and shunt resistances to obtain a more realistic approximation between the experimental and simulated results. We inserted series resistance 25 Ω.cm^2 and shunt resistance 5 x 10^5 Ω.cm^2 respectively, which was extracted from the J-V characteristic curve in section 5.7. Figure 6.2 shows the corresponding changes in PV characteristics.

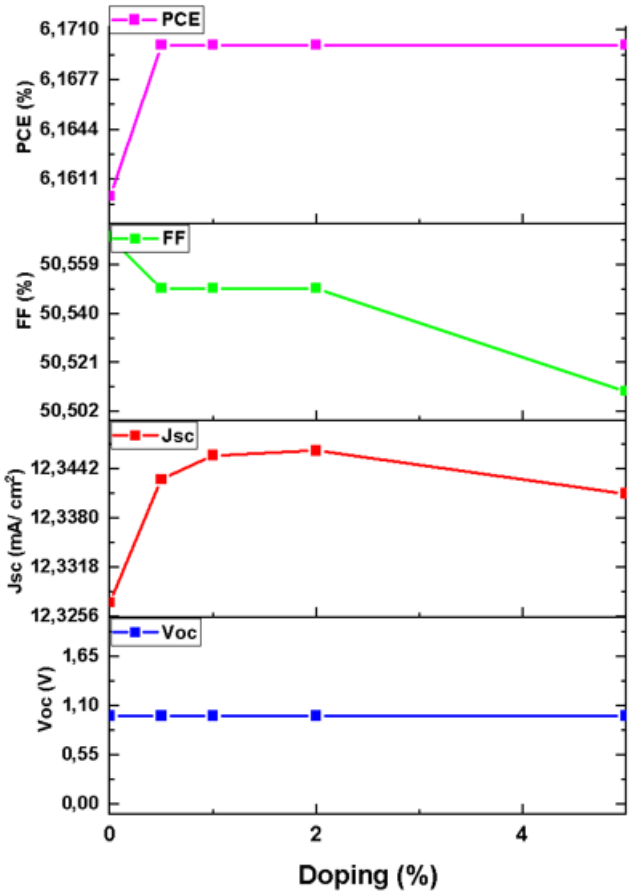

Figure 6.2 Realistic PV characteristics of simulated PSC with R_s& R_{sh}

The results clearly show that by including series and shunt resistance into the simulation model, the FF and PCE reduce from 71.16% to 50.5% and 8.89% to 6.16%, respectively. Additionally, J_{SC} slightly reduced from 12.65 to 12.34 mA/ cm^2 with V_{OC} not being affected. While both J_{SC} and V_{OC} are only slightly affected by the effects of R_s and R_{sh} the effects on FF and PCE are significant in developing a realistic model that compares to the experimental results. A compar-

ison of the experimental and simulated device performance is shown in Table 6.1. Based on the simulation and experimental results shown in Table 6.1, the margin error for V_{OC}, J_{SC}, FF, and PCE are 5.35%, 0.78%, 2.155%, and 8.1% when the best parameter results are compared. The results show an acceptable margin of error and a reliable model developed for further investigation into parameter optimization to reach the higher limits for this device architecture. The optimum ETL doping density using the experimentally determined bandgap for the 2 mol% Zn-doped TiO_2, absorber layer doping density, absorber band gap, and interfacial layer was determined to develop an enhanced simulation model.

Table 6.1 Comparison of experimental device performance with simulated devices after inserting R_s and R_{sh}

Doping %	Data	Voc (V)	Jsc (mA/ cm^2)	FF %	PCE %
0	Experimental	0.90569	12.21851	48.05	5.19
	Ideal Sim	0.9892	12.6187	71.16	8.88
	Realistic Sim	0.9887	12.3274	50.57	6.16
0.5	Experimental	0.90981	12.22852	48.49	5.32
	Ideal Sim	0.9893	12.6349	71.17	8.9
	Realistic Sim	0.9887	12.3429	50.55	6.17
1	Experimental	0.91082	12.2381	48.77	5.43
	Ideal Sim	0.9893	12.6386	71.17	8.9
	Realistic Sim	0.9887	12.3459	50.55	6.17
2	Experimental	0.92774	12.25594	49.48	5.67
	Ideal Sim	0.9893	12.6489	71.17	8.9
	Realistic Sim	0.9887	12.3465	50.55	6.17
5	Experimental	0.9231	12.2387	49.22	5.56
	Ideal Sim	0.9893	12.6321	71.17	8.89
	Realistic Sim	0.9887	12.3411	50.55	6.17
Margin Error % of the best performing PV parameters (Experimental vs Realistic Sim)		5.35	0.78	2.155	8.1

6.3 Influence of ETL Doping

In this study, the influence of increasing donor doping concentration N_d from $10e^5$ cm^{-3} to $10e^{25}$ cm^{-3} on the device's (2 mol% Zn-doped TiO_2 PSC) performance was investigated. Figure 6.2 shows the influence doping concentration on the ETL layer has on the device performance. Increasing doping concentration up to $10e^{10}$ cm^{-3} shows an improvement in the FF (47.42% to 50.73%) and PCE (5.58% to 6.2%) whilst a slight improvement in V_{OC} (0.9634 V to 0.9884 V) and J_{SC} (12.10 mA/ cm ^{2} to 12.34 mA/ cm^2) is also observed. The constant V_{OC} after doping concentration 10^{10} cm^{-3} implies that the rate of recombination is not affected, indicating that recombination resistance has not changed. The findings agree with Jeyakumar et al [211], who reported that high doping densities of the ETL layer improve electron conductivity by offering a lower resistance to the flow of electrons. This also results in a strong electrical field build-up at the ETL/perovskite interface, causing electrons to move more freely away from the perovskite layer. The increased electric field strength generated at high doping concentrations effectively collects electrons while blocking minority carriers from the ETL/perovskite interface, effectively decreasing interface recombination.

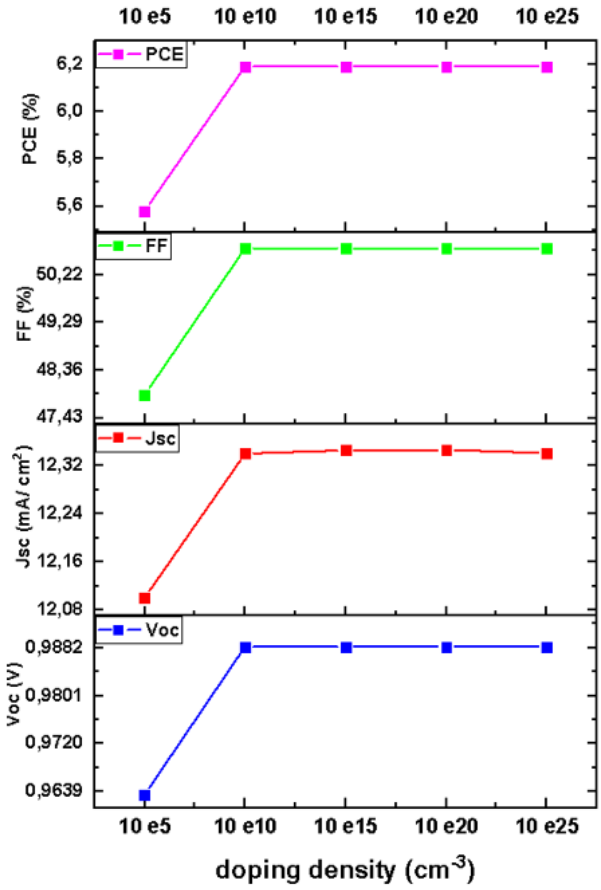

Figure 6.3 PV characteristics of varying ETL N_d doping concentration

6.4 Energy Band Alignment by ETL Doping

In this simulation study, the donor concentration of 2 mol% Zn-doped TiO_2 was varied from $10e^{05}$ cm^{-3} to $10e^{20}$ cm^{-3}. Figure 6.4(a) shows the CB of the absorber and ETL; the CB of the ETL is lower than that of the absorber layer, creating a cliff structure at the ETL/absorber interface. This conduction band offset is improved as the doping concentration increases from $10e^{05}$ to $10e^{20}$ cm^{-3} as shown in Figure 6.4(d). This alignment of CB between the ETL and absorber layer reduces the electron trap states and recombination and increases the conductivity of the ETL, resulting in the improvement of V_{OC} and J_{SC} produced as shown in Figure 6.3. As shown experimentally and via

simulation, doping in TiO_2 affects energy levels, conductivity, and material structure, making this a suitable ETL for the perovskite absorber layer.

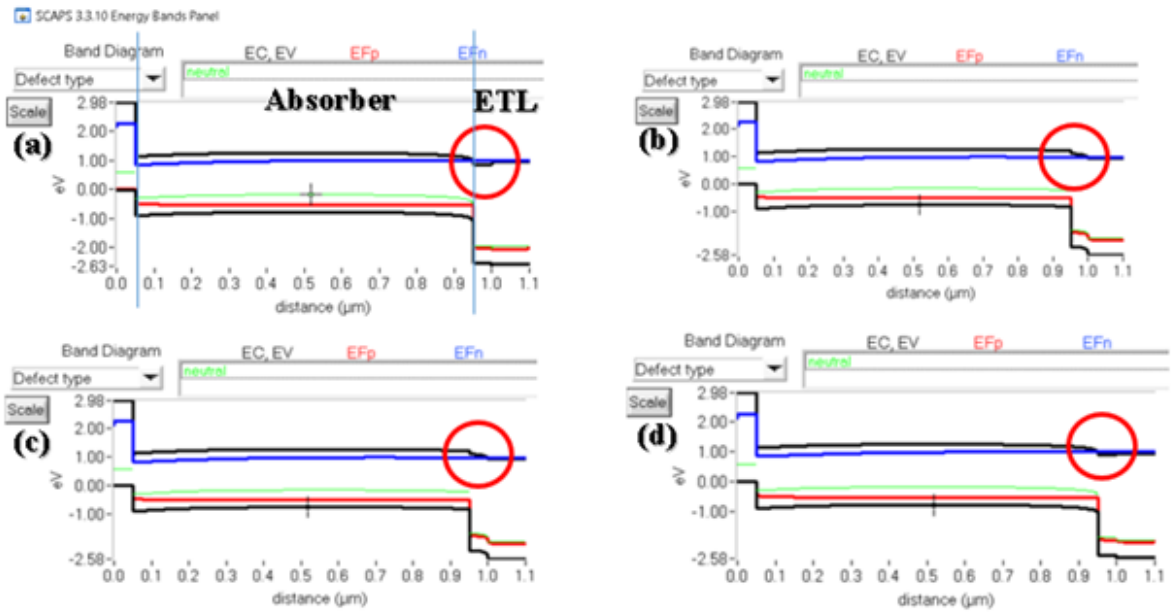

Figure 6.4 (a) N_d=10e^{05} (cm^{-3});(b) N_d=10e^{10} (cm^{-3});(c); N_d=10e^{15} (cm^{-3});(d) N_d=10e^{20} (cm^{-3})

6.5 The External Quantum Efficiency

A PSC's external quantum efficiency primarily depends on the absorption properties of the absorber layer. The quantum efficiency of the PSC describes the conversion of incident photons to charge carriers. The QE plot in Figure 6.5 has a relatively broad absorption from 300 to 620 nm. The EQE cuts off sharply at 620nm (2 eV) due to the 2.03 eV bandgap of the experimentally obtained perovskite layer. There is also a slight increase in the QE as the doping concentration of the ETL layer increases from 10e^{05} to 10e^{20}. This can be attributed to the increased charge carrier concentration caused by doping and the slight increase in J_{SC} (12.10 mA/ cm ^{2} to 12.34 mA/ cm^2)

observed in Figure 6.3.

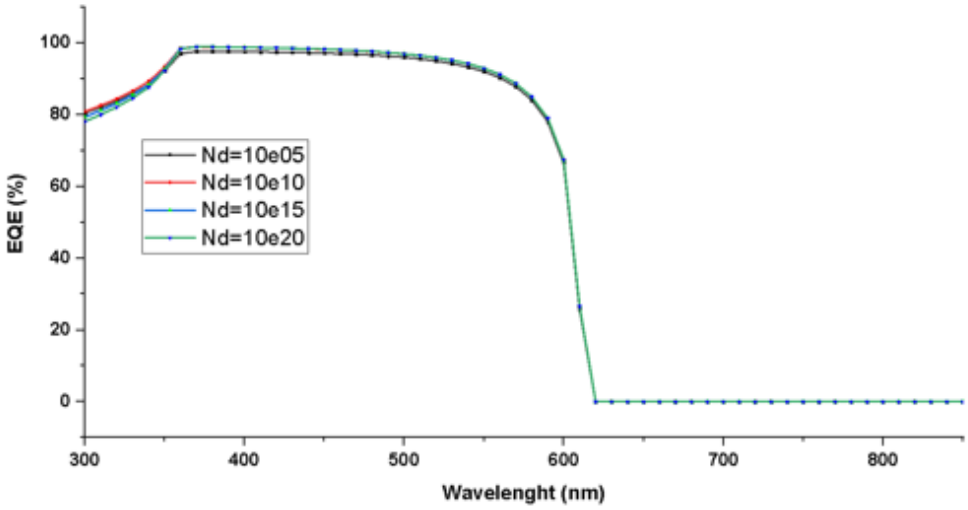

Figure 6.5 Effect of N_d doping concentration on QE

6.6 Influence of Absorber Layer Doping

Introducing dopants into the absorber layer can alter the electrical, optical, and semiconductor properties. This can be achieved by self-doping or doping via an external agent [212]. To enhance the simulation model in this study, the absorber layer acceptor doping concentration was varied from $1e^{15}$ cm $^{-3}$ to $1e^{19}$ cm^{-3}. Figure 6.6 shows the PSC photovoltaic characteristics as a function of acceptor doping density. An increase in V_{OC}, FF and PCE is observed as the N_a doping concentration increases from 1e ^{15} cm $^{-3}$ to $1e^{18}$ cm^{-3}, beyound this all three parameters decrease. Addionally a significant decrease in J_{SC} from 12.34 mA/ cm^2 to 8.15 mA/cm^2 is observed from $1e^{15}$ cm $^{-3}$ to $1e^{19}$ cm^{-3}. This phenomenon can be explained by the fact that heavy doping narrows the depletion zone, enhancing the recombination process at the absorber bulk and leading to a drop in charge carrier mobility [213, 214]

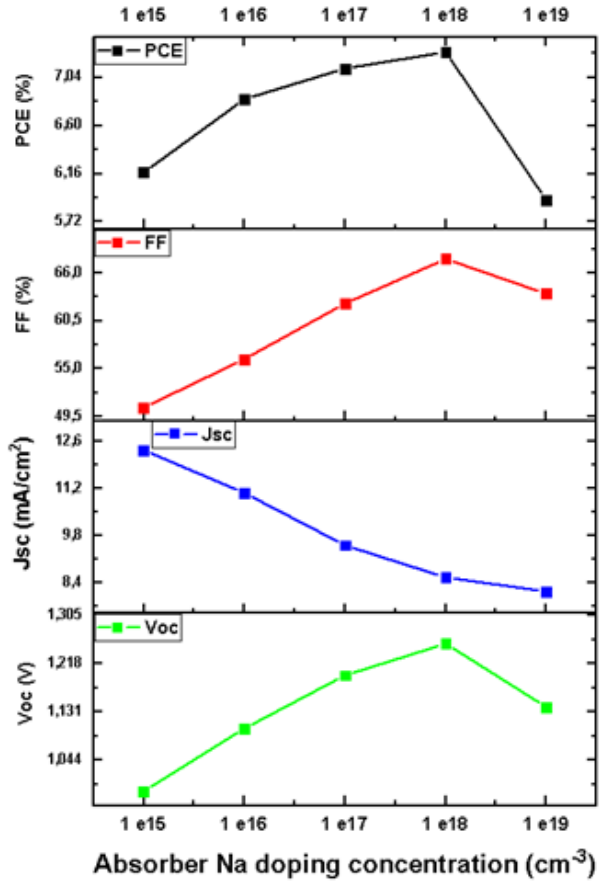

Figure 6.6 PV characteristics of varying absorber layer N_a doping concentration

The decrease in J_{SC} can be further explained from Figure 6.7(a-e), which shows the formation of a cliff structure at the ETL/absorber interface, creating a potential barrier that hinders electron transport. An increase in N_a doping concentration up to $N_a=1e^{18}(1/cm^3)$ shows the VB of the absorber layer align with the Fermi energy level for holes (E_{FP}) which could be attributed to the improvement in V_{OC}, FF and PCE.

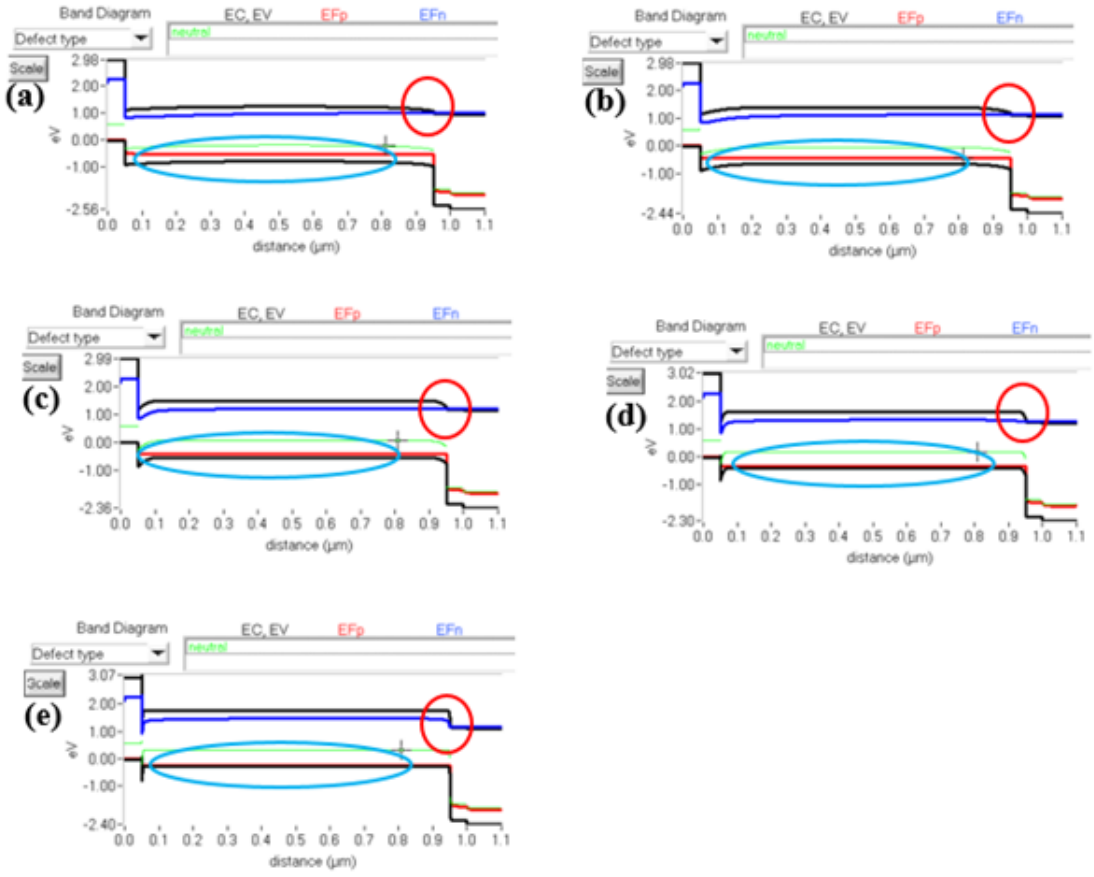

Figure 6.7 (a) N_a=10e^{15}(1/cm^3); (b) N_a=10e^{16}(1/cm^3); (c) N_a=10e^{17}(1/cm^3); (d) N_a=10e^{18}(1/cm^3); (e) N_a=10e^{19}(1/cm^3)

6.7 Influence of Absorber Bandgap Variation

One of the key features of perovskite absorber material is that the bandgap can be tuned. The bandgap of perovskites can be tuned by adjusting the halide ratio and the A site cations [215] [Cesium, formamidinum (FA), methylammonium (MA)]. Here the bandgap was varied in five steps from 1.55 eV to the experimentally obtained 2.03 eV.

Figure 6.8, shows a significant increase as expected in J_{SC} from 8.5691 mA/ cm^2 to 17.951 mA/cm^2 and PCE from 7.27% to 10.79% as the bandgap of the perovskite layer decreased to

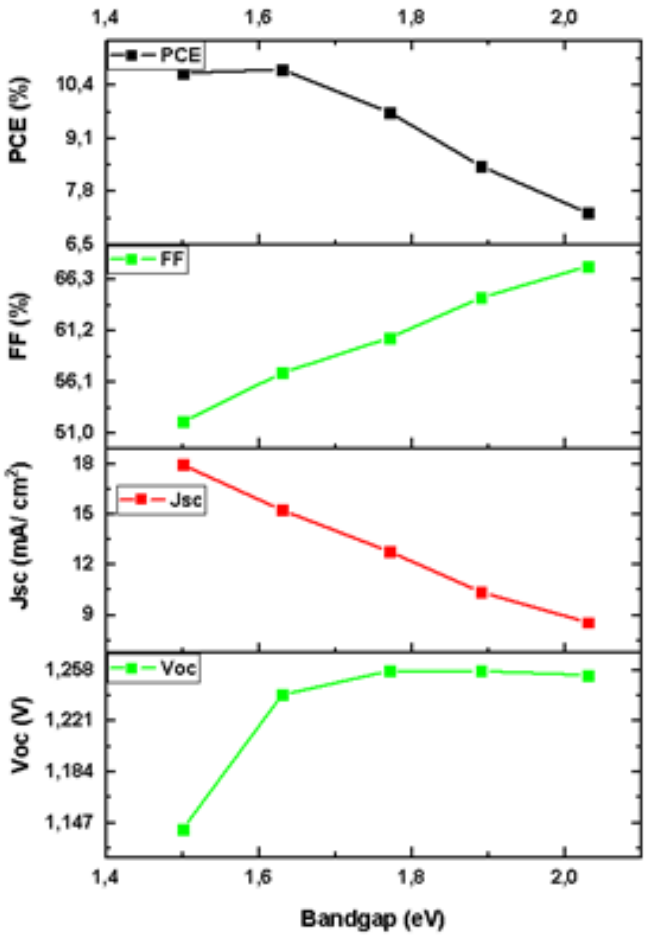

Figure 6.8 Effect of absorber bandgap variation

1.5 eV. A slight decrease in V_{OC} and FF is also noticed from 1.2545 V to 1.1424 V and 67.61% to 52.18% respectively as the bandgap narrows. The drop in FF could be due to the significant increase in J_{SC} leading to an increased probability of recombination currents as voltage increases from zero (short circuit conditions) to V_{OC} (open circuit conditions) at the interfaces and contacts as shown in Figure 6.9(a-b).

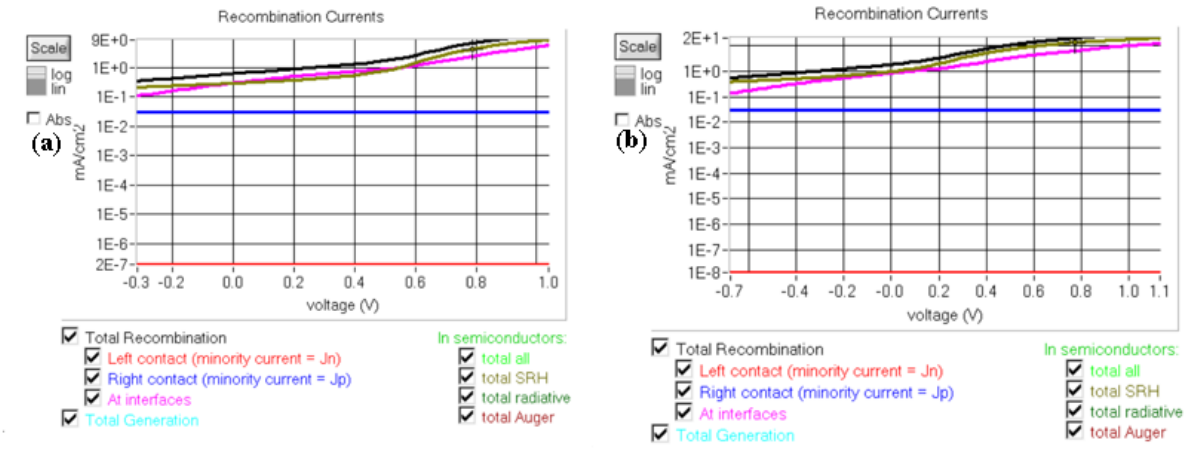

Figure 6.9 (a) Recombination currents at 2.03 eV (b) Recombination currents at 1.55 eV

6.8 Effect of the Interfacial Layer

The amount of energy released when an electron is added to a neutral atom to create a negatively charged ion is referred to as electron affinity. Two types of conduction band offsets (CBO) can be obtained in semiconductor structures based on the electron affinities (X). A spike or cliff band offset could be the CBO in the PSC between the absorber and the ETL. When ETL's conduction band exceeds CBO (+), the conduction band of the perovskite absorber, the spike structure is formed. The electrons trying to flow from the absorber layer to the ETL are blocked by this configuration. Contrarily, if the conduction band of the ETL is lower than that of the absorber layer, as shown in Figure 6.10 below, a cliff, i.e., CBO (-), like structure will form at the ETL/absorber layer which has no potential barrier generated [216].

Accumulation of electrons at the ETL and absorber interface due to conduction band offset (CBO) can negatively affect the performance of PSC. This increase in electrons at the interface increases the probability of charge recombination, causing a decrease in current density and PCE.

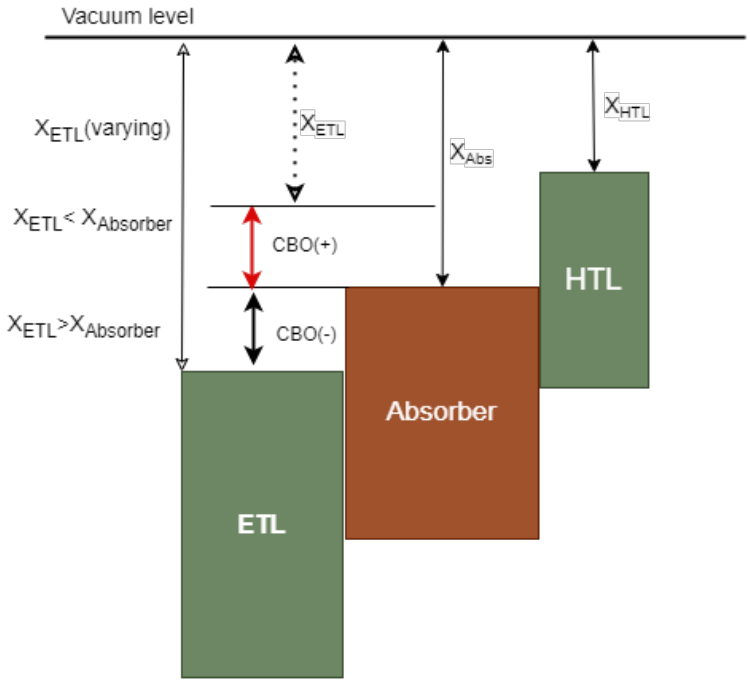

Figure 6.10 Conduction band offset between different PSC layers

By reducing the CBO, charge carrier extraction can be enhanced by reducing the effects of recombination at the ETL absorber interface. The conduction band offset is defined as the difference in electron affinity between the absorber and ETL (X_{ABS} - X_{ETL}). By inserting an interfacial layer with an electron affinity that reduces the CBO, electron transport to the ETL can be improved. In this simulation, we added a range of interfacial layers between the ETL and absorber layer to enhance the performance and demonstrate the benefits of adding an interfacial layer. The selected materials explored were indium (III) sulfide (In_2S_3), cubic silicon carbide (3C-SiC), gallium arsenide (GaAs), and zinc sulfide (ZnS) which provide a conduction band offset with different levels shown in Figure 6.11. The simulation input settings for the interfaces and references are given in Table 6.2.

TiO_2 has an electron affinity of -4.1 eV while the $CH_3NH_3PbI_3$ absorber layer has an electron affinity of -3.9 eV. Here, a cliff CBO (-) is formed as the conduction band of the ETL is lower than

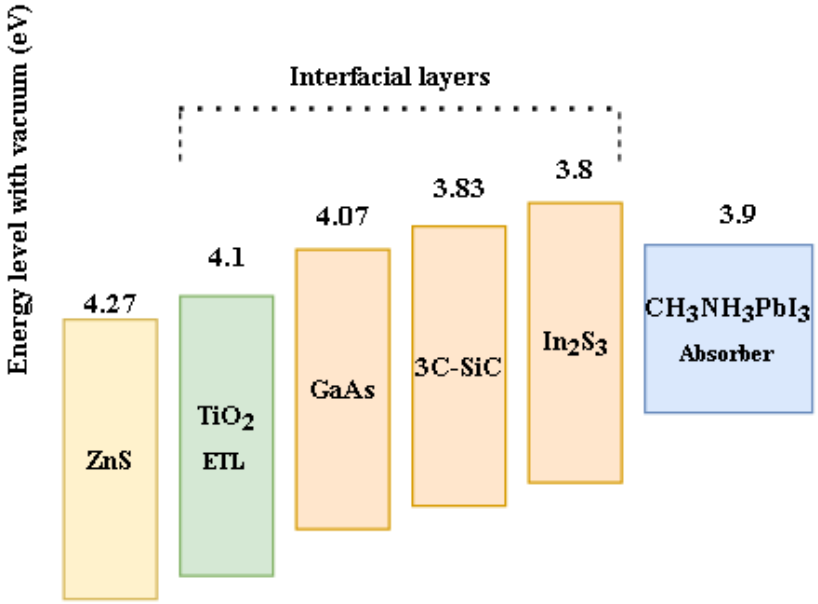

Figure 6.11 Energy level diagram of PSC with varying electron affinity of the interfacial layers

the absorber. as shown in Figure 6.12(a). The difference in electron affinities will produce a -0.1 eV band offset. As obtained in the last section, this structure with no interface produced PV parameters of 1.1424 V, 17.951 mA/cm^2, 52.18%, and 10.79% for V_{oc}, J_{sc}, FF, and PCE respectively. The CBO between the ETL/absorber was adjusted by adding an interfacial layer of In_2S_3 with an electron affinity of -3.8 eV. This produced ΔX_1 = +0.1 and ΔX_2 = -0.3 eV where X_1 and X_2 are the absorber/interfacial and interfacial/ETL interfaces respectively. Since the CBO of the interfacial layer is higher than the absorber layer a spike (CBO+) is formed at the absorber/ interfacial layer interface and a cliff (CBO-) is formed at the interfacial/ETL interface shown in Figure 6.12(b). The inserted layer due to this structure at the interface produces a slight improvement in J_{sc} and V_{oc} however a slight drop in FF and PCE is observed. The PV parameters for the PSC are 1.153 V, 18.05 mA/cm^2, 50.32% and 10.47% for V_{oc}, J_{sc}, FF and PCE respectively.

The CBO was further adjusted by adding an interfacial layer of cubic silicon carbide (3C-SiC)

Table 6.2 Simulation parameters settings of the interfacial layers

Interfacial layer	In_2S_3	3C-SiC	GaAs	ZnS
Thickness (μm)	0.05	0.05	0.05	0.05
Bandgap (eV)	2.4	2.42	2.9	3.1
Electron affinity (eV)	3.8	3.83	4.07	4.27
Dielectric permittivity (relative)	10	9.72	13.18	10
CB effective density of states (1/cm^3)	2.2E+18	1.553E+19	4.7E+17	1.56E+18
VB effective density of states (1/cm^3)	1.8E+19	1.163E+19	9.8E+18	1.84E+18
Electron thermal velocity (cm/s)	1.000E+ 7	1.000E+ 7	1.000E+ 7	1.000E+ 7
Hole thermal velocity (cm/s)	1.000E+ 7	1.000E+7	1.000E+ 7	1.000E+ 7
Electron mobility (cm^2/Vs)	50	650	2830	50
Hole mobility (cm^2/Vs)	12	40	154	20
Shallow uniform donor density N_d (1/cm^3)	1E+18	1E+18	1E+18	1E+18
Shallow uniform acceptor density N_a (1/cm^3)	-	-	-	-
References	[217]	[218]	[219]	[220]

instead of In_2S_3 with an electron affinity of -3.83 eV. This layer produces delta ΔX_1 = 0.07 eV and ΔX_2 = -0.27 eV, this kept the spike-cliff band alignment but further reduced the offset value compared to the In_2S_3 interfacial layer as shown in Figure 6.12(c). The 3C-SiC interfacial layer with decreasing CBO resulted in the PSC parameters becoming 1.262 V, 18.22 mA/cm^2, 53.97%, and 12.09% for V_{oc}, J_{sc}, FF, and PCE respectively.

It can be seen in Figure 6.12(c) that the inserted 3C-SiC interfacial layer further reduces the CBO when compared to Figure 6.12(a) and Figure 6.12(b), leading to an improvement in the photovoltaic parameters shown in Table 6.4. This can be attributed to a decrease in recombination at

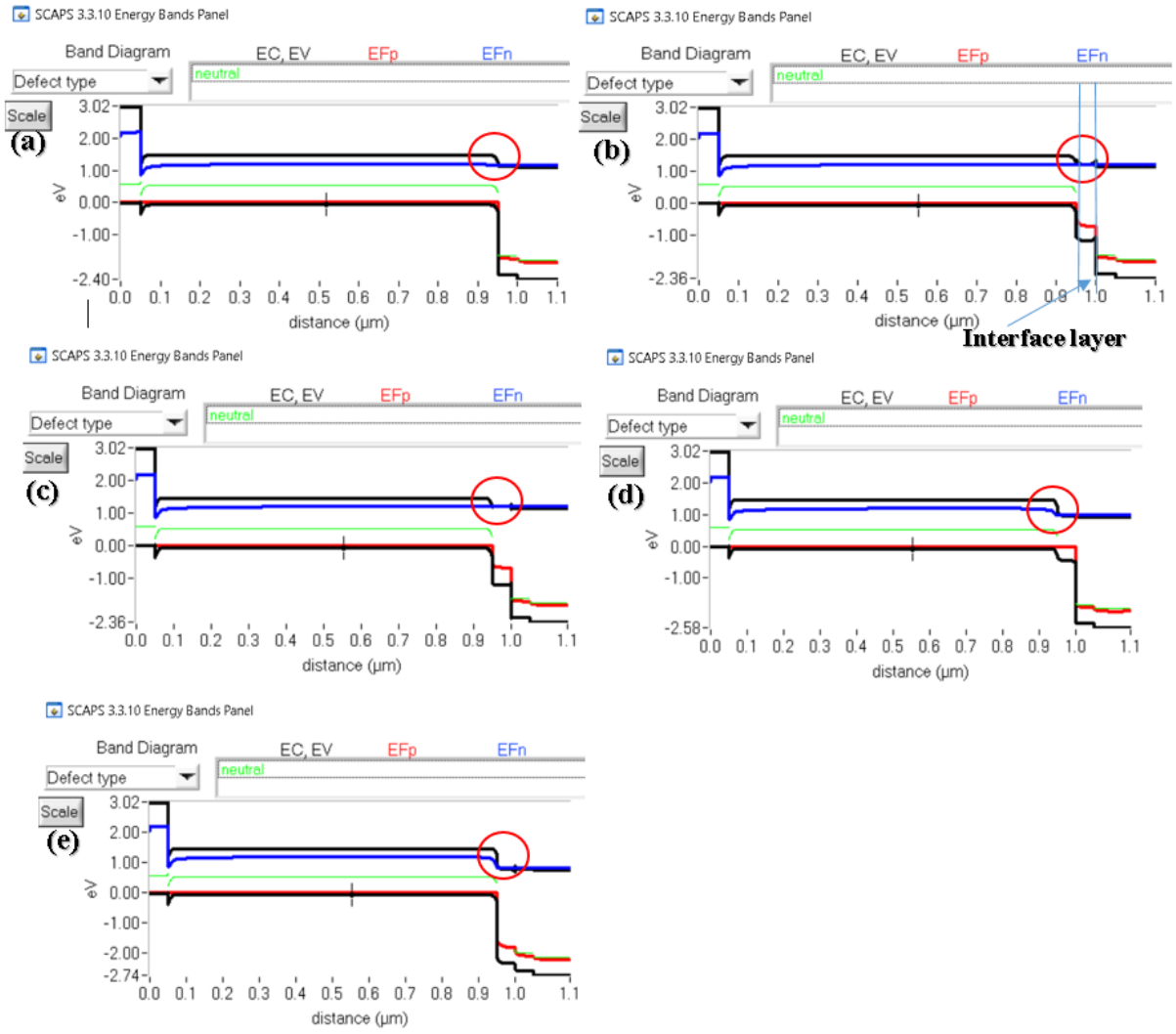

Figure 6.12 (a)Energy band diagram for with no interface (b) Energy band diagram with In_2S_3 interface (c) Energy band diagram with 3C-SiC interface (d) Energy band diagram with GaAs interface (e) Energy band diagram with ZnS interface

the absorber/ ETL interface. Replacing the 3C-SiC layer with GaAs with electron affinity of -4.07 eV causes the CBO to become ΔX_1 = -0.17 eV and ΔX_2 = - 0.03 eV resulting in a transformation from the spike-cliff structure to a cliff-cliff structure shown in Figure 6.12(d). The gradient developed by the cliff CBO between the absorber and ETL causes an increase in J_{sc} to 20.47 mA/cm^2 however V_{oc}, FF, and PCE decrease to 0.961 V, 40.58%, and 7.89% respectively. This could be

attributed to the cliff cliff structure formed at the interface. To confirm this attribution an interfacial layer of ZnS with an electron affinity of -4.27 eV was used between the ETL and absorber. This produced ΔX_1 = -0.37 eV and ΔX_2 = +0.17 eV resulting in the formation of a cliff-spike structure shown in Figure 6.12(e). This structure at the interface badly affected the PV parameters, decreasing V_{oc}, J_{sc}, FF, and PCE to 0.805 V, 17.61 mA/cm^2, 38%, and 5.4% respectively. The impact of CBO variation on the PSC performance parameters for the different interfacial layers in Table 6.3, while Figure 6.13 illustrates the influence of the various interfacial layers on V_{oc}, J_{sc}, FF, and PCE.

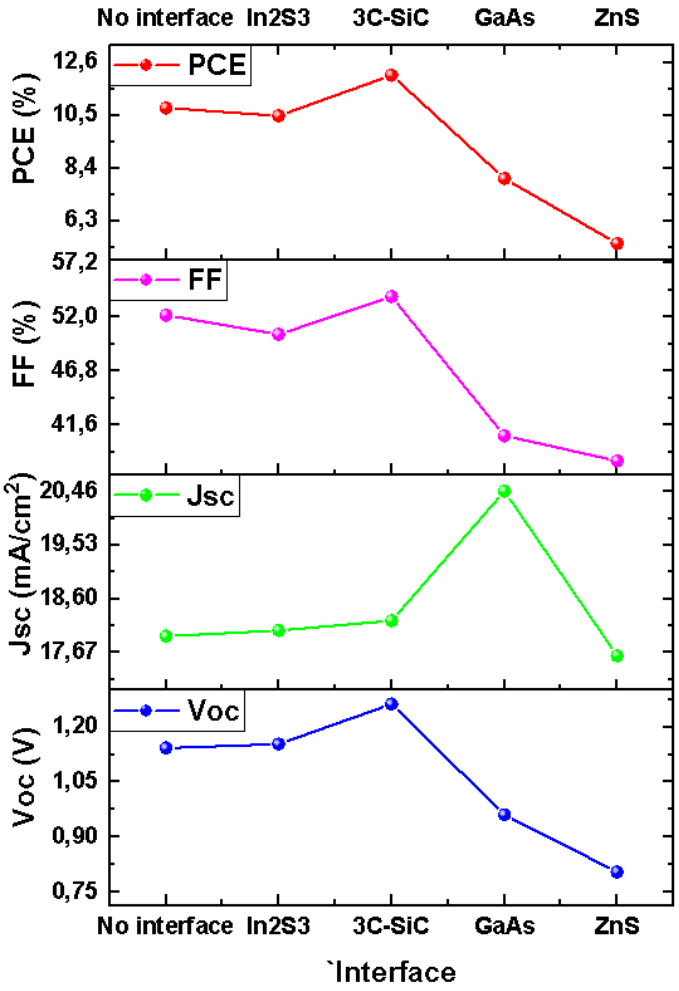

Figure 6.13 Perovskite solar cell PV parameters with and without interfaces

The V_{oc} changes from 0.805 V for the ZnS interfacial layer to 1.262 V for the 3C-SiC interfacial layer down to could be due to the improved energy level alignment at the interface between the ETL and absorber layer. The V_{oc} for the other interfacial layers of around 1 V were relatively similar. The maximum current density achieved was 20.47 mA/cm^2 when the electron affinity was -4.07 eV, transformed into a cliff-cliff structure at the ETL/absorber interface, however, this resulted in a decrease in FF and PCE to 40.58% and PCE 7.98% respectively. As the electron affinity went beyond -4.07 eV, J_{sc} dropped to its lowest value of 17.61 mA/cm^2 which could be attributed to the increase in the recombination process as a result of the cliff-spike transformation at the interface. This resulted in a further decrease of FF and PCE to 38.16% and 5.4% respectively. The findings indicate that after the insertion of the 3C-SiC interface with an electron affinity of -3.83 eV the reduced CBO and formation of a spike-cliff structure resulted in the best PCE of 12.09% with an improvement of 12.04% from the initial PCE 10.79% with no interface material inserted.

Table 6.3 PV parameter values of simulated PSC with and without interfacial layers

PSC	V_{OC} (V)	J_{SC} (mA/ cm^2)	FF %	PCE %
No interface	1.1424	17.951	52.18	10.79
In_2S_3 interface	1.153	18.05	50.32	10.47
3C-SiC interface	1.2291	18.2241	53.97	12.09
GaAs interface	0.961	20.47	40.58	7.98
ZnS interface	0.805	17.61	38.16	5.4

6.9 External Quantum Efficiency

The QE plot in Figure 6.14 shows a broad generation of charge carriers from 300 nm to 800 nm for the enhanced model using the 3C-SiC interface layer when compared against the reference simu-

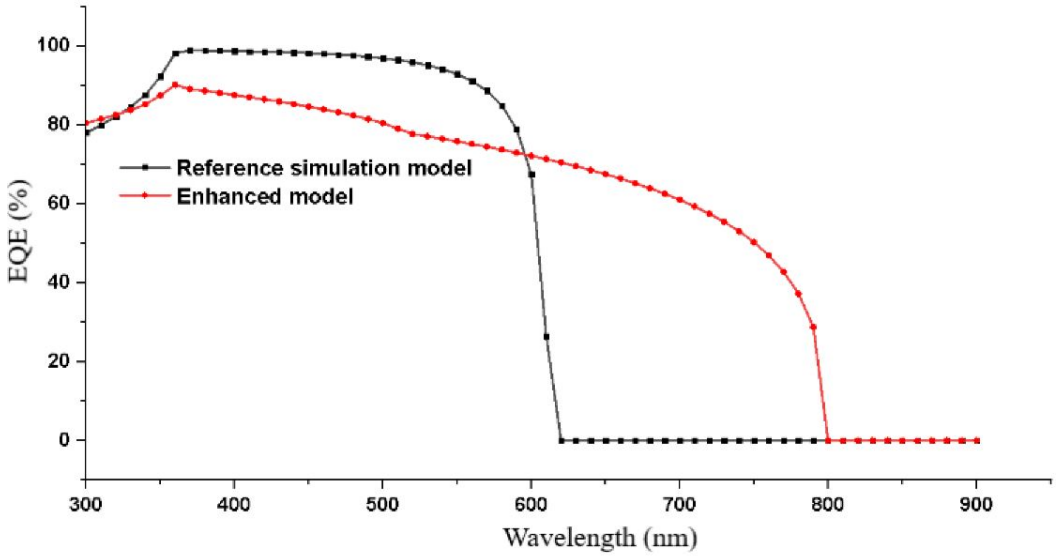

Figure 6.14 EQE of simulation mode with no interface vs. enhanced simulation model with 3C-SiC interface

lation model developed. Between 310 to 600nm, the enhanced simulation model shows decreased charge carrier generation. The decrease in charge generation in this region can be attributed to the decrease in Jsc from 12.34 mA/ cm ^{2} to 8.5691 mA/cm^2 when the absorber layer doping concentration was set to N_a=1e^{18}(1/cm^3) resulting in an increased PCE of 7.27% due to the improvement in FF and V_{OC}. However between 600 and 800 nm, the enhanced simulation model displays an increased charge carrier generation which corresponds to the increase in J_{SC} from 12.34 mA/ cm ^{2} to 18.22 mA/ cm^2 which resulted in a PCE of 12.09%. The EQE cuts off at 800 nm corresponding to the optimized $CH_3NH_3PbI_3$ bandgap of 1.55 eV.

Chapter 7

CONCLUSION and RECOMMENDATIONS

7.1 Conclusion

The aim of the thesis was to empirically investigate the effect of ion-doped metal oxide on the efficiency of PSCs. The intention was to improve the performance experimentally and utilize the findings gained to further enhance the performance of the devices numerically using SCAPS 1D simulation. We studied the structural, morphological, and optical properties of the perovskite, TiO_2 and Zn-doped TiO_2 thin films before fabricating planar heterojunction perovskite solar cells using the one-step method under controlled ambient conditions (relative humidity < 65%, room temperature $\sim 20^oC$). We demonstrated that PSCs can be fabricated without expensive equipment under ambient conditions by ensuring the ambient and process parameters are carefully considered.

The comprehensive XRD analysis of perovskite films annealed at varying temperatures and durations provided valuable insights into their structural characteristics. Strong peaks in the XRD patterns indicated the optimized formation of a tetragonal perovskite ($CH_3NH_3PbI_3$) phase with high crystallinity for samples annealed at 65°C for 30 s and 100°C for 1 min. However, the emergence of peaks corresponding to the hexagonal lead iodide phase (PbI_2) in the sample annealed for 2 min indicated the decomposition of the perovskite phase. The calculated average crystallite sizes further highlighted differences between samples, with enhanced crystallinity and larger crystal sizes observed for the perovskite phase in films annealed at 65°C for 30 s and 100°C for 1 min. Differences in crystallite sizes indicated that the optimized annealing conditions lead to enhanced crystallinity, attributed to improved composition homogeneity and reduced defects. The XRD analysis of Zn-TiO_2 synthesized nanoparticles revealed a pure anatase phase with no rutile phase. Trends in peak characteristics and crystallite sizes suggested that Zn doping influenced the crystallinity and surface performance of TiO_2, with a decrease in crystallite size from 12.7 to 7.1 nm as Zn content increased.

Investigation through TEM unveiled a consistent and homogeneous spherical morphology for Zn-doped TiO_2 nanoparticles, with particle sizes ranging from 15 to 20 nm. The incorporation of Zn ions into the TiO_2 lattice structure resulted in an increase in particle size, leading to a reduction in bandgap and recombination sites in the ETL layer. The Tauc plot supported these findings, illustrating bandgap narrowing with increasing Zn doping up to 2 mol%. These insights underscore the potential for controlled manipulation of nanoparticle size and composition, particularly through Zn doping, to optimize the electronic properties and performance of TiO_2 nanoparticles across diverse applications.

SEM analysis of TiO_2 and Zn-doped TiO_2 thin films post-annealing at 550°C showcased a uniform surface without discernible pinholes, a critical factor for enhancing electron movement in

perovskite solar cells (PSC). Zn-doped TiO_2 exhibited irregular morphologies and conical shapes, with reduced particle agglomeration as Zn doping concentration increased. Surface roughness analysis revealed a gradual reduction, suggesting that Zn insertion mitigates nanoparticle aggregation. Smoother surfaces are pivotal for enhancing electron transport behavior and optimizing the interface for perovskite layer deposition. Energy dispersive X-ray spectrometry confirmed Zn incorporation into TiO_2, with higher concentrations correlating to increased Zn doping.

The SEM image of the $CH_3NH_3PbI_3$ thin film demonstrated a non-uniform, dense layer with well-interconnected particles, influenced by the use of anti-solvent during spin coating. This played a crucial role in improving the perovskite layer's surface for efficient PSC performance.

UV-Vis and photoluminescence analyses of TiO_2 and Zn-doped TiO_2 thin films elucidated key optical and electronic properties. Band gap analysis revealed a concentration-dependent modulation in the band gap of Zn-doped TiO_2, with a minimum of 3.38 eV for 2 mol% Zn. This reduction in band gap aligned with enhanced electron transfer efficiency, as supported by photoluminescence quenching. Overall, Zn doping demonstrates promise for optimizing the optical and electronic performance of TiO_2 thin films in perovskite applications.

The experimental investigation into Zn-doped TiO_2 for perovskite solar cells (PSCs) showcased nuanced performance dynamics. The incremental increase in open circuit voltage (V_{OC}) from 0.90569 V to 0.92774 V with escalating Zn doping concentrations was notable. Zn incorporation into the TiO_2 lattice structure effectively lowered the conduction band (CB), facilitating electron injection from the absorber into the compact layer. Comparative analysis with undoped TiO_2 highlighted the advantageous impact of Zn-doping on electron injection from the perovskite to the electron transport layer (ETL) and electron transport rate. This was reflected in a rise in short-circuit current density (J_{sc}) from 12.21851 mA/cm^2 to 12.25594 mA/cm^2 as Zn doping increased

from 0 to 2 mol%. The power conversion efficiency (PCE) exhibited a moderate improvement from 5.199% with undoped TiO_2 to 5.675% at 2 mol% Zn doping, accompanied by an increase in fill factor (FF) from 48.05 to 49.4823.

The simulation and analysis of perovskite solar cells (PSCs) presented in this study yield valuable insights into the factors influencing their performance and potential avenues for improvement. Increasing the doping concentration of the ETL improved the PCE (6.2 %) by aligning the ETL and absorber layer CB, reducing electron trap states, recombination, and increasing conductivity. Increasing the doping concentration of the absorber layer up to N_a=1e^{18}(1/cm^3) showed improvements in the PCE (7.14%), FF, and V_{OC}. However, a drop in PCE (5.92%), FF, and V_{OC} was observed at higher doping concentrations due to a cliff structure formation at the ETL/ perovskite interface. Although the PCE improved to 10.79% by narrowing the bandgap of the perovskite layer, the cliff structure was still present.

Various materials, including indium (III) sulfide (In_2S_3), cubic silicon carbide (3C-SiC), gallium arsenide (GaAs), and zinc sulfide (ZnS), were investigated for their suitability as interfacial layers. The electron affinity differences between the electron transport layer (ETL) and the absorber layer were manipulated to optimize the band alignment at the interfaces. The introduction of an In_2S_3 interfacial layer with an electron affinity of -3.8 eV resulted in a spike-cliff structure, improving the current density (Jsc) and voltage (Voc), but with a slight reduction in fill factor (FF) and power conversion efficiency (PCE). Replacing In_2S_3 with 3C-SiC (electron affinity -3.83 eV) further improved the performance by reducing the conduction band offset (CBO). This led to a spike-cliff structure and achieved the highest PCE of 12.09%, surpassing the initial PCE of 10.79% without an interfacial layer. Introducing GaAs and ZnS interfacial layers caused variations in CBO, resulting in cliff-cliff and cliff-spike structures, respectively. These changes negatively impacted PSC parameters, notably reducing FF and PCE. The findings highlight the sensitivity of PSC per-

formance to the interfacial layer properties. The 3C-SiC interfacial layer, with its specific electron affinity, proved to be particularly effective in improving energy level alignment, reducing CBO, and enhancing overall PSC efficiency.

The simulation study showed that proper band alignment at the ETL/perovskite interface by doping and adding an interfacial layer is crucial in improving the performance of PSCs. This further underscores the need to bridge the gap between theoretical modeling and practical application in advancing PSC technology. Ideal models serve as a foundational framework, but the realities of environmental conditions, material stability, and recombination must be considered in real-world applications. By addressing these complexities, and optimizing material properties and deposition techniques, PSCs can achieve higher levels of efficiency and reliability.

In the quest for more efficient and sustainable solar energy conversion, the experimental and numerical findings presented in this study provide a valuable roadmap for future research and development in the field of perovskite solar cells. Ongoing investigations into parameter optimization and innovative material combinations are essential to push the boundaries of PSC technology and move closer to realizing their potential as a clean and accessible energy source.

7.2 Recommendations

Further studies investigating the influence of process conditions on the structure of TiO_2 is a good starting point. Understanding how defects in the materials are created during fabrication is vital, as this significantly affects the material's properties. Synthesized anatase phase TiO_2 nanoparticles at 550^{o}C consume high electrical energy during annealing and limit device fabrication to solid substrates. Investigation and optimization into low-temperature annealing for TiO_2 will al-

low annealing onto more flexible substrates such as polyethylene (PET) and provide a way to develop flexible PSC, allowing for numerous applications. Annealing the TiO_2 thin films at varying temperatures and studying their influence on crystallinity, trap states, conduction band position, elemental composition, electron transport, and recombination will allow linking of annealing temperature, material composition, and device performance.

The DMF solvent used in the perovskite fabrication process is toxic, Stancu et al. [221] and Doolin et al. [222] showed that less toxic alternatives such as N –methyl-2-Pyrrolidone (NMP), ethyl acetate (EA) and DMSO, dimethyl propylene urea (DMPU), 2-methyl tetrahydrofuran respectively showed promising results although the drop in PCE indicates further research into solvent engineering is required.

Incorporating a surfactant such as Triton X-100 into the ETL, absorber, and HTL can improve device performance. Rahman et al. [223] showed that the Cadium sulfide (CdS) based ETL layer film quality, homogeneity, and material properties improved by incorporating Triton X-100 surfactant into the precursor solution. Additionally, Kim et al. [224] showed that incorporating a passivation layer using a polyaniline polymer as an interfacial modifier inserted between the ETL perovskite and ETL layer confined the Pb^{2+} ions at the passivation layer, thus maintaining an 84 % efficiency in ambient air for one month. Paravazian et al. [225] also showed that introducing small amounts of Triton X-100 surfactant into a triple cation mixed halide precursor solution improved the film quality, surface coverage, wettability, and crystallinity, resulting in an improved PCE and stability. Lee et al. [226] also showed that adding Triton X-100 into an HTL precursor solution consisting of polyanile: poly (styrene sulfonate) improved the hole extraction, film quality, and PCE, resulting in an alternate, less expensive, and low-temperature option for the HTL.

Carbon-based electrodes are attractive alternatives to high-temperature thermal evaporation of

back metal contacts due to the cost-effective processability and stability for large-scale production processes; however, issues related to inferior performance and poor interface contact between the perovskite and carbon electrodes require further investigation [227]. Graphene, carbon nanotubes, and carbon black are promising candidates that have shown excellent mechanical deformation robustness as flexible carbon electrodes. However, the problem of interface contact remains the main challenge facing carbon-based electrodes for PSCs.

Lastly, it's clear that due to the fantastic optical properties of perovskites and their tunable bandgap the engineering of metal oxides is critical to developing tandem and multijunction solar cells. Exploration into alternative metal oxide combinations to align with the current state-of-the-art single, double, and triple cation perovskite combinations is imperative in engineering the ETL/perovskite interface to push the PCE beyond the Shockley Queisser limit.

References

[1] HK Mohajan. *British petroleum (BP) statistical review of world energy*. London: British Petroleum, 2015. *www.bp.com*. Accessed 11/05/23

[2] World Health Organization et al. Ambient air pollution: *A global assessment of exposure and burden of disease*. 2016. *www.who.int*. Accessed 04/02/23

[3] Michael Jakob and Jérôme Hilaire. *Unburnable fossil-fuel reserves*. Nature, 517(7533):150–151, 2015

[4] France Greenpeace. *At which price? The hidden costs of nuclear wastes-a report by greenpeace*, France. 2019. *www.greenpeace.org*. Accessed 17/03/23

[5] Khaled Almohammadi and Amine Allouhi. *Techno-economic assessment of residential buildings grid connected solar PV in major Saudi cities*. *Available at SSRN 4523067*.

[6] H Ritchie, M Roser, and P Rosado. South Africa: Energy country profile. *Our World in Data*, 2022. *www.ourworldindata.org*. Accessed 05/04/23

[7] Global Renewables Outlook. *Global renewables outlook: Energy transformation 2050*. Abu Dhabi, United Arab Emirates, 2020. *www.irena.org*. Accessed 12/04/23

[8] Peter Diamandis. S*olar energy revolution: a massive opportunity*. *www.diamandis.com* Accessed 21/05/23

[9] Green Econometrics. *Understanding the cost of solar energy,* 2007. www.greenecon.net Accessed 25/04/23

[10] Zhelu Hu, Chenxin Ran, Hui Zhang, Lingfeng Chao, Yonghua Chen, and Wei Huan. *The current status and development trend of perovskite solar cells*. Engineering, 2022.

[11] Antonio Ricardo Zanatta. *The Shockley–Queisser limit and the conversion efficiency of silicon - based solar cells*. Results in Optics, 9:100320, 2022.

[12] Florian Gebhard and Florian Gebhard. *Metal, insulator transitions*. Springer, 1997.

[13] Uichiro Mizutani. *Introduction to the electron theory of metals*. Cambridge University Press, 2001.

[14] Amrozia Shaheen, Wasif Zia, and Muhammad Sabieh Anwar. *Band structure and electrical conductivity in semiconductors*. LUMS School of Science and Engineering, Lahore, Pakistan, 2011.

[15] Andreas Wacker and Matematisk Fysik. *An introduction to the concept of band structure*. Lund University, Sweden, 15, 2010.

[16] Alfred Clark. *The chemisorptive bond: Basic concepts,* Volume 32. Elsevier, 2012.

[17] William Shockley. *The Shockley - Queisser limit. J.* Appl. Phys, 32(3):510–519, 1961.

[18] Owen D Miller, Eli Yablonovitch, and Sarah R Kurtz. *Strong internal and external luminescence as solar cells approach the Shockley–Queisser limit*. IEEE Journal of Photovoltaics, 2(3):303–311, 2012.

[19] Jenny Nelson. *The physics of solar cell*s, Imperial College Press, Singapore, 2003.

[20] Juan Bisquert. *The physics of solar cells: perovskites, organics, and photovoltaic fundamentals*. CRC press, 2017.

[21] Mohd Ashraf Zainol Abidin, Muhammad Nasiruddin Mahyuddin, and Muhammad Ammirrul Atiqi Mohd Zainuri. *Solar photovoltaic architecture and agronomic management in agrivoltaic system*: A review. Sustainability, 13(14):7846, 2021.

[22] Ricardo A Marques Lameirinhas, João Paulo N Torres, and João P de Melo Cunha. *A photovoltaic technology review: history, fundamentals and applications*. Energies, 15(5):1823, 2022.

[23] Kiran Ranabhat, Leev Patrikeev, Aleksandra Antal'evna-Revina, Kirill Andrianov, Valerii Lapshinsky, and Elena Sofronova. *An introduction to solar cell technology*. Journal of Applied Engineering Science, 14(4):481–491, 2016.

[24] Salama Abdelhady, Mohamed S Abd-Elhady, and Mennatallah M Fouad. *An understanding of the operation of silicon photovoltaic panels*. Energy Procedia, 113:466–475, 2017.

[25] Mohammadreza Aghaei, Amir Nedaei, Aref Eskandari, and Jafar Milimonfared. *Introductory chapter:* Solar photovoltaic energy. *www.intechopen.com*. Accessed 14/05/23

[26] Mubarak Dirar Abd-Alla Yagoub, Mohamed Hamdan Hussin Ahmed, and Ilham Mohamed Kamal. *Study of structural and electrical properties of NiRxRSR$_1$-XROR$_2$R compound for possible application in solar cell.* International Journal of Innovative Science, Engineering & Technology, Vol 09 Issue 11, November 2022.

[27] Adrian Kitai. *Principles of Solar Cells, LEDs and Diodes: The role of the PN junction.* John Wiley & Sons, 2011.

[28] Zeeshan Abid, Faiza Wahad, Sughra Gulzar, Muhammad Faheem Ashiq, Muhammad Shahid Aslam, Munazza Shahid, Muhammad Altaf, and Raja Shahid Ashraf. *Solar cell efficiency energy materials.* Fundamentals of Solar Cell Design, pages 271–315, 2021.

[29] Jeffery L Gray. *The physics of the solar cell. Handbook of photovoltaic science and engineering,* 2:82–128, 2011.

[30] Saïdou Madougou, Mohamadou Kaka, and Gregoire Sissoko. *Silicon solar cells: Recombination and electrical parameters.* Solar Energy, pages 69–81, 2010.

[31] Andrew Blakers and Ngwe Zin. Silicon solar cell device structures. *Photovoltaic Solar Energy: From Fundamentals to Applications.* Wiley, pages 80–91, 2016.

[32] Yuqiang Liu, Yajuan Li, Yiliang Wu, Guangtao Yang, Luana Mazzarella, Paul Procel-Moya, Adele C Tamboli, Klaus Weber, Mathieu Boccard, Olindo Isabella, et al. *High-efficiency silicon heterojunction solar cells: materials, devices and applications.* Materials Science and Engineering: R: Reports, 142:100579, 2020.

[33] Stefaan De Wolf, Antoine Descoeudres, Zachary C Holman, and Christophe Ballif. *High-efficiency silicon heterojunction solar cells:* A review, 2(1):7–24, 2012.

[34] Giuseppina Ciulla, Valerio Lo Brano, Vincenzo Di Dio, and Giovanni Cipriani. *A comparison of different one-diode models for the representation of I–V characteristic of a PV cell.* Renewable and Sustainable Energy Reviews, 32:684–696, 2014.

[35] Hyeonah Park, Yong-Jung Kim, and Hyosung Kim. *PV cell model by single-diode electrical equivalent circuit.* Journal of Electrical Engineering & Technology, 11(5):1323–1331, 2016.

[36] M Azzouzi, Dumitru Popescu, and Mohammed Bouchahdane. *Modeling of electrical characteristics of photovoltaic cell considering single-diode model.* Journal of Clean Energy Technologies, 4(6):414–420, 2016.

[37] Masoud Darvish Ganji, Mahyar Rezvani, and Sepideh Tanreh. *Characterization and theoretical modeling of solar cells. Fundamentals of Solar Cell Design.* Wiley, pages 169–215, 2021.

[38] EMG Rodrigues, Rui Melicio, VMF Mendes, and Joao PS Catalao. *Simulation of a solar cell considering single-diode equivalent circuit model.* International conference on renewable energies and power quality, Spain, Volume 1, pages 13–15, 2011.

[39] Ali Khatibi, Fatemeh Razi Astaraei, and Mohammad Hossein Ahmadi. *Generation and combination of the solar cells: A current model review.* Energy Science & Engineering, 7(2):305–322, 2019.

[40] Dhass, A.D. & Natarajan, E. & Lakshmi, P.. (2012). *Influence of shunt resistance on the performance of solar photovoltaic cell.* Proceedings - ICETEEEM 2012, International Conference on Emerging Trends in Electrical Engineering and Energy Management. 382-386. 10.1109/ICETEEEM.2012.6494522.

[41] Eugene A Katz. Perovskite: name puzzle and German - *Russian odyssey of discovery.* Helvetica Chimica Acta, 103(6):e2000061, 2020.

[42] Victor Moritz Goldschmidt. *Die gesetze der krystallochemie. Naturwissenschaften*, 14(21):477–485, 1926.

[43] Christian Knakkergård Møller. *The structure of perovskite-like caesium plumbo trihalides*. Munksgaard, 1959.

[44] Dieter Weber. *$CH_3NH_3SnBrxI_{3-x}$ (x= 0-3), ein Sn (ii)-system mit kubischer perowskitstruktur/ $CH_3NH_3SnBrxI_{3-x}$ (x= 0-3), a Sn (ii)-system with cubic perovskite structure.* Zeitschrift für Naturforschung *B,* 33(8):862–865, 1978.

[45] Giles E Eperon, Samuel D Stranks, Christopher Menelaou, Michael B Johnston, Laura M Herz, and Henry J Snaith. *Formamidinium lead trihalide: a broadly tunable perovskite for efficient planar heterojunction solar cells.* Energy & Environmental Science, 7(3):982–988, 2014.

[46] Akihiro Kojima, Kenjiro Teshima, Yasuo Shirai, and Tsutomu Miyasaka. *Organometal halide perovskites as visible-light sensitizers for photovoltaic cells.* Journal of the American Chemical society, 131(17):6050–6051, 2009.

[47] Jeong-Hyeok Im, Chang-Ryul Lee, Jin-Wook Lee, Sang-Won Park, and Nam-Gyu Park. *6.5% efficient perovskite quantum-dot-sensitized solar cell.* Nanoscale, 3(10):4088–4093, 2011.

[48] Michael M Lee, Joël Teuscher, Tsutomu Miyasaka, Takurou N Murakami, and Henry J Snaith. *Efficient hybrid solar cells based on meso-superstructured organometal halide perovskites*. Science, 338(6107):643–647, 2012.

[49] Hui-Seon Kim, Chang-Ryul Lee, Jeong-Hyeok Im, Ki-Beom Lee, Thomas Moehl, Arianna Marchioro, Soo-Jin Moon, Robin Humphry-Baker, Jun-Ho Yum, Jacques E Moser, et al. *Lead iodide perovskite sensitized all-solid-state submicron thin film mesoscopic solar cell with efficiency exceeding 9%*. Scientific Reports, 2(1):591, 2012.

[50] Woon Seok Yang, Byung-Wook Park, Eui Hyuk Jung, Nam Joong Jeon, Young Chan Kim, Dong Uk Lee, Seong Sik Shin, Jangwon Seo, Eun Kyu Kim, Jun Hong Noh, et al. *Iodide management in formamidinium-lead-halide–based perovskite layers for efficient solar cells.* Science, 356(6345):1376–1379, 2017.

[51] A. Markose, D. Das, and P. Ravindran, *Quantitative framework development for understanding the relationship between doping and photo electrochemical energy conversion of TiO_2,* Mater. Adv., vol. 4, no. 16, pp. 3399–3451, 2023.

[52] C.-Y. Hsu *et al.*, *Experimental and theoretical study of improved mesoporous titanium dioxide perovskite solar cell: The impact of modification with graphene oxide,* Heliyon, vol. 10, no. 4, p. e26633, Feb. 2024.

[53] Martin Green, Ewan Dunlop, Jochen Hohl-Ebinger, Masahiro Yoshita, Nikos Kopidakis, and Xiaojing Hao. *Solar cell efficiency tables (version 57).* Progress in Photovoltaics: Research and Applications, 29(1):3–15, 2021.

[54] Teddy Salim, Shuangyong Sun, Yuichiro Abe, Anurag Krishna, Andrew C Grimsdale, and Yeng Ming Lam. Perovskite-based solar cells: *Impact of morphology and device architecture on device performance.* Journal of Materials Chemistry A, 3(17):8943–8969, 2015.

[55] René M Williams and Aram Farawar. *Perovskite solar cells: Stability, design architecture, photophysical properties, and morphology of the film in organometal halide perovskite based photovoltaics*. Literature thesis, University of Amsterdam. 2016.

[56] Priyanka Roy, Numeshwar Kumar Sinha, Sanjay Tiwari, and Ayush Khare. *A review on perovskite solar cells: Evolution of architecture, fabrication techniques,commercialization issues and status.* Solar Energy, 198:665–688, 2020.

[57] Istiak Hussain, Hoang Phong Tran, Jared Jaksik, Justin Moore, Nazmul Islam, and M Jasim Uddin. *Functional materials, device architecture, and flexibility of perovskite solar cell.* Emergent Materials, 1:133–154, 2018.

[58] Hyun Suk Jung and Nam-Gyu Park. *Perovskite solar cells: from materials to devices.* 11(1):10–25, 2015.

[59] Meidan Que, Boyue Zhang, Jin Chen, Xingtian Yin, and Sining Yun. *Carbon-based electrodes for perovskite solar cells.* Materials Advances, 2(17):5560–5579, 2021.

[60] Nam-Gyu Park. *Perovskite solar cells: an emerging photovoltaic technology.* Materials Today, 18(2):65–72, 2015.

[61] M. Imamzai, M. Aghaei, Y. H. Thayoob, and M. Forouzanfar, *"A Review on Comparison between Traditional Silicon Solar Cells and Thin- Film CdTe Solar Cells,"* 2012.

[62] Yu-Che Hsiao, Ting Wu, Mingxing Li, Qing Liu, Wei Qin, and Bin Hu. *Fundamental physics behind high-efficiency organo-metal halide perovskite solar cells.* Journal of Materials Chemistry A, 3(30):15372–15385, 2015.

[63] Khalil Ebrahim Jasim. *Dye sensitized solar cells-working principles, challenges and opportunities.* Solar Cells-Dye-Sensitized Devices, 8:172 ¯A210, 2011.

[64] Tze-Chien Sum and Nripan Mathews. *Halide perovskites: photovoltaics, light emitting devices, and beyond.* John Wiley & Sons, 2019.

[65] M. Vasilopoulou, A. R. B. Mohd Yusoff, and M. K. Nazeeruddin, *Background and Basic Knowledge of Perovskite Solar Cells in Printable Mesoscopic Perovskite Solar Cells,* 1st ed.,

H. Han, M. Grätzel, A. Mei, and Y. Hu, Eds., Wiley, 2023, pp. 1–18

[66] Wenxi Guo, Zijie Xu, Fayin Zhang, Shuyao Xie, Hongyao Xu, and Xiang Yang Liu. *Recent development of transparent conducting oxide-free flexible thin-film solar cells.* Advanced Functional Materials, 26(48):8855–8884, 2016.

[67] Raquel Ramírez-Amador, Gregorio Flores-Carrasco, Salvador Alcántara-Iniesta, Julio Rodríguez González, Ogilver García-Teniza, Eduardo Mercado-Agular, and Arturo Benito Vásquez-Ortiz. *Structural, morphological, optical, and electrical characterization of fluorine doped tin oxide (FTO) thin films synthesized by PSP.* Solid State Phenomena, 286:64–71, 2019.

[68] KL Chopra, S Major, and DK Pandya. Transparent conductors—a status review. *Thin solid films,* 102(1):1–46, 1983.

[69] Germain Rey, Céline Ternon, Mircea Modreanu, Xavier Mescot, Vincent Consonni, and Daniel Bellet. *Electron scattering mechanisms in fluorine-doped SnO_2 thin films.* Journal of Applied Physics, 114(18), 2013.

[70] M Ait Aouaj, Rosy Diaz, Azzam Belayachi, F Rueda, and M Abd-Lefdil. *Comparative study of ITO and FTO thin films grown by spray pyrolysis.* Materials Research Bulletin, 44(7):1458–1461, 2009.

[71] Yukihiko Kawamura, Hiroyuki Mashiyama, and Katsuhiko Hasebe. *Structural study on cubic-tetragonal transition of $CH_3NH_3PbI_3$.* Journal of the Physical Society of Japan, 71(7):1694–1697, 2002.

[72] Govind Reddy. *Design, synthesis and applications of novel hole transporting materials for Perovskite solar cells.* PhD thesis, RMIT University, 2020.

[73] Duyen H Cao, Constantinos C Stoumpos, Christos D Malliakas, Michael J Katz, Omar K Farha, Joseph T Hupp, and Mercouri G Kanatzidis. *Remnant PbI_2, an unforeseen necessity in high-efficiency hybrid perovskite-based solar cells?,* Applied Materials, 2(9), 2014.

[74] Paolo Umari, Edoardo Mosconi, and Filippo De Angelis. *Relativistic GW calculations on $CH_3NH_3PbI_3$ and $CH_3NH_3SnI_3$ perovskites for solar cell applications.* Scientific Reports, 4(1):4467, 2014.

[75] Zhibo Yao, Wenli Wang, Heping Shen, Ye Zhang, Qiang Luo, Xuewen Yin, Xuezeng Dai, Jianbao Li, and Hong Lin. *$CH_3NH_3PbI_3$ grain growth and interfacial properties in meso-structured perovskite solar cells fabricated by two-step deposition.* Science and Technology of Advanced Materials, 18(1):253–262, 2017.

[76] Man Yu, Shuai Yuan, Hao-Yi Wang, Jia-Shang Zhao, Yujun Qin, Li-Min Fu, Jian-Ping Zhang, and Xi-Cheng Ai. *Characterization of the influences of morphology on the intrinsic properties of perovskite films by temperature-dependent and time-resolved spectroscopies.* Physical Chemistry Chemical Physics, 20(9):6575–6581, 2018.

[77] Weiwei Li. *Investigations of the structural, dielectric, and piezoelectric properties of $MAPbI_3$ hybrid perovskites single crystals.* PhD thesis, Le Mans, 2021.

[78] Tom Baikie, Yanan Fang, Jeannette M Kadro, Martin Schreyer, Fengxia Wei, Subodh G Mhaisalkar, Michael Graetzel, and Tim J White. *Synthesis and crystal chemistry of the hybrid perovskite (CH_3NH_3) PbI_3 for solid-state sensitised solar cell applications.* Journal of Materials Chemistry A, 1(18):5628−5641, 2013.

[79] Constantinos C Stoumpos, Christos D Malliakas, and Mercouri G Kanatzidis. *Semiconducting tin and lead iodide perovskites with organic cations: phase transitions, high mobilities, and near-infrared photoluminescent properties.* Inorganic Chemistry, 52(15):9019−9038, 2013.

[80] Xin Yu Chin, Daniele Cortecchia, Jun Yin, Annalisa Bruno, and Cesare Soci. *Lead iodide perovskite light-emitting field-effect transistor.* Nature Communications, 6(1):7383, 2015.

[81] Ahmed Ali Said, Jian Xie, and Qichun Zhang. *Recent progress in organic electron transport materials in inverted perovskite solar cells.* Small, 15(27):1900854, 2019.

[82] Hyunwoong Park, Yiseul Park, Wooyul Kim, and Wonyong Choi. *Surface modification of TiO_2 photocatalyst for environmental applications.* Journal of Photochemistry and Photobiology C: Photochemistry Reviews, 15:1−20, 2013.

[83] Dennis YC Leung, Xianliang Fu, CuifangWang, Meng Ni, Michael KH Leung, XuxuWang, and Xianzhi Fu. *Hydrogen production over titania-based photocatalysts.* ChemSusChem, 3(6):681−694, 2010.

[84] H Kordi Ardakani. *Electrical and optical properties of in situ "hydrogen-reduced" titanium dioxide thin films deposited by pulsed excimer laser ablation.* Thin Solid Films, 248(2):234–239, 1994.

[85] Marketa Zukalova, ArnoštZukal, Ladislav Kavan, Mohammad K Nazeeruddin, Paul Liska, and Michael Gratzel. *Organized mesoporous TiO_2 films exhibiting greatly enhanced performance in dye-sensitized solar cells.* Nano Letters, 5(9):1789–1792, 2005.

[86] Yulong Liao,Wenxiu Que, Qiaoying Jia, Yucheng He, Jin Zhang, and Peng Zhong. *Controllable synthesis of brookite/anatase/rutile TiO_2 nanocomposites and single-crystalline rutile nanorods array.* Journal of Materials Chemistry, 22(16):7937–7944, 2012.

[87] Stacey J Smith, Rebecca Stevens, Shengfeng Liu, Guangshe Li, Alexandra Navrotsky, *Juliana Boerio-Goates, and Brian F Woodfield. Heat capacities and thermodynamic functions of TiO_2 anatase and rutile: Analysis of phase stability.* American Mineralogist, 94(2-3):236–243, 2009.

[88] Shang-Di Mo and WY Ching. *Electronic and optical properties of three phases of titanium dioxide: Rutile, anatase, and brookite.* Physical Review B, 51(19):13023, 1995.

[89] Toshiaki Ozawa, Mitsunobu Iwasaki, Hiroaki Tada, Tomoki Akita, Koji Tanaka, and Seishiro Ito. *Low-temperature synthesis of anatase–brookite composite nanocrystals: the junction effect on photocatalytic activity.* Journal of Colloid and Interface Science, 281(2):510–513, 2005.

[90] Xiaobo Chen and Samuel S Mao. *Titanium dioxide nanomaterials: synthesis, properties, modifications, and applications.* Chemical Reviews, 107(7):2891–2959, 2007.

[91] Yoon-Chae Nah, Indhumati Paramasivam, and Patrik Schmuki. *Doped TiO_2 and TiO_2 nanotubes: synthesis and applications.* ChemPhysChem, 11(13):2698–2713, 2010.

[92] A Narayan-Banerjee. *The design, fabrication, and photocatalytic utility of nanostructured semiconductors: Focus on TiO_2-base nanostructures.* Nanotechnology, Science and Applications, 4:35–65, 2011.

[93] David Reyes-Coronado, G Rodriguez-Gattorno, ME Espinosa-Pesqueira, C Cab, R d De Coss, and G Oskam. *Phase-pure TiO_2 nanoparticles: anatase, brookite and rutile.* Nanotechnology, 19(14):145605, 2008.

[94] Don T Cromer and K Herrington. *The structures of anatase and rutile.* Journal of the American Chemical Society, 77(18):4708–4709, 1955.

[95] Marketa Zukalova, Arnošt Zukal, Ladislav Kavan, Mohammad K Nazeeruddin, Paul Liska, and Michael Gratzel. *Organized mesoporous TiO_2 films exhibiting greatly enhanced performance in dye-sensitized solar cells.* Nano Letters, 5(9):1789−1792, 2005.

[96] Julian Haines and JM Leger. *X-ray diffraction study of TiO_2 up to 49 GPa.* Physica B: Condensed Matter, 192(3):233−237, 1993.

[97] Dieter *Kerner. Chemical processing of advanced materials*, 1992, 1048 pp., ISBN 0-471-54201-6. Advanced Materials, 5(9):682−682, 1993.

[98] Bok-Min Kim, Seon-Gyun Rho, and Choon-Hyoung Kang. *Effects of TiO_2 structures in dye-sensitized solar cell.* Journal of Nanoscience and Nanotechnology, 11(2):1515−1517, 2011.

[99] David O Scanlon, CharlesWDunnill, John Buckeridge, Stephen A Shevlin, Andrew J Logsdail, Scott M Woodley, C Richard A Catlow, Michael J Powell, Robert G Palgrave, Ivan P Parkin, et al. *Band alignment of rutile and anatase TiO_2.* Nature Materials, 12(9):798−801, 2013.

[100] Yuanyuan Zhou, Zhongmin Zhou, Min Chen, Yingxia Zong, Jinsong Huang, Shuping Pang, and Nitin P Padture. Doping and alloying for improved perovskite solar cells. *Journal of Materials Chemistry A,* 4(45):17623−17635, 2016.

[101] H Kordi Ardakani. *Electrical and optical properties of in situ "hydrogen-reduced" titanium dioxide thin films deposited by pulsed excimer laser ablation.* Thin Solid Films, 248(2):234 − 239, 1994.

[102] Yanqin Gai, Jingbo Li, Shu-Shen Li, Jian-Bai Xia, and Su-Huai Wei. *Design of narrow-gap TiO_2: a passivated codoping approach for enhanced photoelectrochemical activity.* Physical Review Letters, 102(3):036402, 2009.

[103] AT Paxton and L Thien-Nga. *Electronic structure of reduced titanium dioxide.* Physical Review B, 57(3):1579, 1998.

[104] Michael A Henderson. A surface science perspective on TiO_2 photocatalysis. Surface Science Reports, 66(6-7):185−297, 2011.

[105] Raja Sellappan. *Mechanisms of enhanced activity of model TiO_2/ carbon and TiO_2/ metal nanocomposite photocatalysts*. Chalmers Tekniska Hogskola (Sweden). PhD thesis, University of Technology Göteborg, 2013.

[106] Ulrike Diebold. *The surface science of titanium dioxide.* Surface Science Reports, 48(5-8):53–229, 2003.

[107] JingWang, Minchao Qin, Hong Tao,Weijun Ke, Zhao Chen, JiaweiWan, Pingli Qin, Liangbin Xiong, Hongwei Lei, Huaqing Yu, et al. Performance enhancement of perovskite solar cells with Mg-doped TiO_2 compact film as the hole-blocking layer. Applied Physics Letters, 106(12), 2015.

[108] Liang-Bin Xiong, Jia-Lin Li, Bo Yang, and Ying Yu. *Ti^{3+} in the surface of titanium dioxide: generation, properties and photocatalytic application.* Journal of Nanomaterials, 2012:9–9, 2012.

[109] Henry J Snaith and Lukas Schmidt-Mende. *Advances in liquid-electrolyte and solid-state dye-sensitized solar cells.* Advanced Materials, 19(20):3187–3200, 2007.

[110] Xiaobo Chen and Samuel S Mao. *Titanium dioxide nanomaterials: synthesis, properties, modifications, and applications.* Chemical Reviews, 107(7):2891–2959, 2007.

[111] M Radecka, M Rekas, A Trenczek-Zajac, and K Zakrzewska. *Importance of the band gap energy and flat band potential for application of modified TiO_2 photoanodes in water photolysis.* Journal of Power Sources, 181(1):46–55, 2008.

[112] Yuanyuan Zhou, Zhongmin Zhou, Min Chen, Yingxia Zong, Jinsong Huang, Shuping Pang, and Nitin P Padture. *Doping and alloying for improved perovskite solar cells.* Journal of Materials Chemistry A, 4(45):17623–17635, 2016.

[113] Adriana Zaleska. *Doped-TiO_2: a review.* Recent patents on engineering, 2(3):157–164, 2008.

[114] Yuexiang Li, Shaoqin Peng, Fengyi Jiang, Gongxuan Lu, and Shuben Li. *Effect of doping TiO_2 with alkaline-earth metal ions on its photocatalytic activity.* Journal of the Serbian Chemical Society, 72(4):393–402, 2007.

[115] Fei Huang, Aihua Yan, and Hui Zhao. *Influences of doping on photocatalytic properties of TiO_2 photocatalyst. Semiconductor Photocatalysis-Materials, Mechanisms and Applications.* Intech, pages 31–80, 2016.

[116] Dieter Weber. *$CH_3NH_3SnBrxI_3$-x (x= 0-3), ein Sn (ii)-system mit kubischer perowskitstruktur/ $CH_3NH_3SnBrxI_3$-x (x= 0-3), a Sn (ii)-system with cubic perovskite structure.* Zeitschrift fur Naturforschung B, 33(8):862–865, 1978.

[117] Margarita Sanchez-Dominguez, Getsemani Morales-Mendoza, Maria J Rodriguez-Vargas, Claudia C Ibarra-Malo, Arturo A Rodriguez-Rodriguez, Andrea V Vela-Gonzalez, SA Perez-Garcia, and Ricardo Gomez. *Synthesis of Zn-doped TiO_2 nanoparticles by the novel oil-in-water micro-emulsion method and their use for the photocatalytic degradation of phenol.* Journal of Environmental Chemical Engineering, 3(4):3037–3047, 2015.

[118] Nick Serpone. *Is the band gap of pristine TiO_2 narrowed by anion-and cation-doping of titanium dioxide in second-generation photocatalyst.?* Journal of Physical Chemistry B, 2006.

[119] JingWang, Minchao Qin, Hong Tao,Weijun Ke, Zhao Chen, JiaweiWan, Pingli Qin, Liangbin Xiong, Hongwei Lei, *Huaqing Yu, et al. Performance enhancement of perovskite solar cells with Mg-doped TiO_2 compact film as the hole-blocking layer.* Applied Physics Letters, 106(12), 2015.

[120] Guannan Yin, Jiaxin Ma, Hong Jiang, Juan Li, Dong Yang, Fei Gao, Jinghui Zeng, Zhike Liu, and Shengzhong Frank Liu. *Enhancing efficiency and stability of perovskite solar cells through Nb-doping of TiO_2 at low temperature.* ACS Applied Materials & Interfaces, 9(12):10752–10758, 2017.

[121] Xinlian Deng, Yanqing Wang, Zhendong Cui, Long Li, and Chengwu Shi. *Y-doping TiO_2 nanorod arrays for efficient perovskite solar cells.* Super Lattices and Microstructures, 117:283–287, 2018.

[122] Sandeep K Pathak, Antonio Abate, P Ruckdeschel, B Roose, Karl C Godel, Yana Vaynzof, Aditya Santhala, Shun-Ichiro Watanabe, Derek J Hollman, Nakita Noel, et al. *Performance and stability enhancement of dye-sensitized and perovskite solar cells by al doping of TiO_2.* Advanced Functional Materials, 24(38):6046–6055, 2014.

[123] Hirokazu Nagaoka, Fei Ma, Dane W Dequilettes, Sarah M Vorpahl, Micah S Glaz, Adam E Colbert, Mark E Ziffer, and David S Ginger. *Zr incorporation into TiO_2 electrodes reduces hysteresis and improves performance in hybrid perovskite solar cells while increasing carrier lifetimes.* The Journal of Physical Chemistry Letters, 6(4):669–675, 2015.

[124] Feng Zhu, Panpan Zhang, Xuejun Wu, Limin Fu, Jianping Zhang, and Dongsheng Xu. *The origin of higher open-circuit voltage in Zn-doped TiO_2 nanoparticle-based dye-sensitized solar cells.* ChemPhysChem, 13(16):3731–3737, 2012.

[125] Kai-PingWang and Hsisheng Teng. *Zinc-doping in TiO_2 films to enhance electron transport in dye-sensitized solar cells under low-intensity illumination.* Physical Chemistry Chemical Physics, 11(41):9489–9496, 2009.

[126] Qiuping Liu, Yang Zhou, Yandong Duan, Min Wang, and Yuan Lin. I*mproved photovoltaic performance of dye-sensitized solar cells (DSSC) by Zn^{+} Mg co-doped TiO_2 electrode.* Electrochimica Acta, 95:48–53, 2013.

[127] Bart Roose, Sandeep Pathak, and Ullrich Steiner. *Doping of TiO_2 for sensitized solar cells.* Chemical Society Reviews, 44(22):8326–8349, 2015.

[128] Laxmi Nakka, Yuanhang Cheng, Armin Gerhard Aberle, and Fen Lin. *Analytical review of Spiro-OMeTAD hole transport materials: Paths toward stable and efficient perovskite solar cells.* Advanced Energy and Sustainability Research, 3(8):2200045, 2022.

[129] Vinod E Madhavan, Iwan Zimmermann, Ahmer AB Baloch, Afsal Manekkathodi, Abdelhak Belaidi, Nouar Tabet, and Mohammad Khaja Nazeeruddin. *CuSCN as hole transport material with 3d/2d perovskite solar cells.* ACS Applied Energy Materials, 3(1):114–121, 2019.

[130] Francesco Lamberti, Teresa Gatti, Enrico Cescon, Roberto Sorrentino, Antonio Rizzo, Enzo Menna, Gaudenzio Meneghesso, Moreno Meneghetti, Annamaria Petrozza, and Lorenzo Franco. *Evidence of Spiro-OMeTAD de-doping by tert-butylpyridine additive in hole transporting layers for perovskite solar cells.* Chem, 5(7):1806–1817, 2019.

[131] William H Nguyen, Colin D Bailie, Eva L Unger, and Michael D McGehee. *Enhancing the hole-conductivity of spiro-ometad without oxygen or lithium salts by using Spiro (TFSI) in perovskite and dye-sensitized solar cells.* Journal of the American Chemical Society, 136(31):10996–11001, 2014.

[132] Yang Yang, Minh Tam Hoang, Disheng Yao, Ngoc Duy Pham, Vincent Tiing Tiong, Xiaoxiang Wang, and Hongxia Wang. *Spiro-OMeTAD or CuSCN as a preferable hole transport material for carbon-based planar perovskite solar cells.* Journal of Materials Chemistry A, 8(25):12723–12734, 2020.

[133] Michael Saliba, Juan-Pablo Correa-Baena, Christian M Wolff, Martin Stolterfoht, Nga Phung, Steve Albrecht, Dieter Neher, and Antonio Abate. *How to make over 20% efficient perovskite solar cells in regular (n–i–p) and inverted (p–i–n) architectures.* Chemistry of Materials, 30(13):4193–4201, 2018.

[134] Nathan L Chang, AnitaWing Yi Ho-Baillie, Doojin Vak, Mei Gao, Martin A Green, and Renate J Egan. *Manufacturing cost and market potential analysis of demonstrated roll-to-roll perovskite photovoltaic cell processes.* Solar Energy Materials and Solar Cells, 174:314– 324, 2018.

[135] Gan, Yongjin & Bi, Xueguang & Liu, Yucheng & Qin, Binyi & Li, Qingliu & Jiang, Qubo & Mo, Pei. (2020). *Numerical Investigation Energy Conversion Performance of Tin-*

Based Perovskite Solar Cells Using Cell Capacitance Simulator. Energies. 13. 10.3390/en13225907.

[136] Meidan Que, Boyue Zhang, Jin Chen, Xingtian Yin, and Sining Yun. *Carbon-based electrodes for perovskite solar cells.* Materials Advances, 2(17):5560–5579, 2021.

[137] Seigo Ito and Ajay Kumar Baranwal. *Carbon counter electrodes for dye-sensitized and perovskite solar cells.* Counter Electrodes for Dye-sensitized and Perovskite Solar Cells, 2:457–485, 2018.

[138] Huiyin Zhang, Keke Song, Lianqing Zhu, and Qingbo Meng. *Back-interface regulation for carbon-based perovskite solar cells.* Carbon, 168:372–391, 2020.

[139] J Livage, C Sanchez, M Henry, and S Doeuff. *The chemistry of the sol-gel process.* Solid State Ionics, 32:633–638, 1989.

[140] Ana C Marques. *Sol-gel process: an overview.* Lehigh Universitesi, ABD, 2007.

[141] Dmitry Bokov, Abduladheem Turki Jalil, Supat Chupradit, Wanich Suksatan, Mohammad Javed Ansari, Iman H Shewael, Gabdrakhman H Valiev, and Ehsan Kianfar. *Nanomaterial by sol-gel method: synthesis and application.* Advances in Materials Science and Engineering, 2021:1–21, 2021.

[142] Manasi Manoj Karkare. *Estimation of band gap and particle size of TiO_2 nanoparticle synthesized using sol gel technique.* In 2014 International Conference on Advances in Communication and Computing Technologies (ICACACT 2014), pages 1–5. IEEE, 2014.

[143] Niranjan Sahu, B Parija, and S Panigrahi. *Fundamental understanding and modelling of spin coating process: A review.* Indian Journal of Physics, 83(4):493–502, 2009.

[144] Mohammed S Mehde, Abdulnasser M Al-Gebori, and Ali K Hantoosh. *The effect of the spinning speed variation on the perovskite solar cell efficiency.* In IOP Conference Series: Materials Science and Engineering, volume 757, page 012071. IOP Publishing, 2020.

[145] *Scanning Electron Microscopy*. Nanoscience instruments, 2008.

[146] Faith Mokobi. *Scanning electron microscope (SEM)—definition, principle, parts, images.* Microbe Notes, 2021.

[147] Edward Pena. *Photocatalytic hydrogen evolution using porphyrin-metal organic framework nanocomposites decorated with plasmonic gold nanoparticles*. Molecular Catalysis, 2023.

[148] Frank Krumeich. *Properties of electrons, their interactions with matter and applications in electron microscopy.* Laboratory of Inorganic Chemistry, disponivel em http://www. microscopy. ethz. ch/downloads/Interactions. pdf, consultado em, pages 3–08, 2011.

[149] SM Steen and FY Zhang. *Energy dispersive x-ray and electrochemical impedance spectroscopies for performance and corrosion analysis. In Journal of Physics:* Conference Series, volume 548, page 012062. IOP Publishing, 2014.

[150] Ana Violeta Girao, Gianvito Caputo, and Marta C Ferro. *Application of scanning electron microscopy–energy dispersive, x-ray spectroscopy (SEM-EDS).* In Comprehensive Analytical Chemistry, volume 75, pages 153–168. Elsevier, 2017.

[151] Surender Kumar Sharma, Dalip Singh Verma, Latif Ullah Khan, Shalendra Kumar, and Sher Bahadar Khan. *Handbook of materials characterization.* Springer, 2018.

[152] Catherine Berthomieu and Rainer Hienerwadel. *Fourier transform infrared (FTIR) spectroscopy.* Photosynthesis Research, 101:157–170, 2009.

[153] Sang Hun Lee, Seung-min Park, and Luke P Lee. *Optical methods in studies of factory system. In Bioelectronic Nose: Integration of Biotechnology and Nanotechnology*. *Springer*, 2014.

[154] Brent Fultz and James M Howe. *Transmission electron microscopy and diffractometry of materials.* Springer Science & Business Media, 2012.

[155] Cristian Fabian Escalante Sierra. *Fundamentals of transmission electron microscopy, the technique with the best resolution in the world.* Screen, 9:10, 2019.

[156] Tahani H Flemban. *High quality zinc oxide thin films and nanostructures prepared by pulsed laser deposition for photodetectors.* PhD thesis, 2017.

[157] Hugo M Rietveld. *A profile refinement method for nuclear and magnetic structures.* Journal of Applied Crystallography, 2(2):65–71, 1969.

[158] Nicholas T Nolan, Michael K Seery, and Suresh C Pillai. *Crystallization and phase transition characteristics of sol- gel-synthesized zinc titanates.* Chemistry of Materials, 23(6):1496–1504, 2011.

[159] Yang Leng. *Materials characterization: introduction to microscopic and spectroscopic methods.* John Wiley & Sons, 2013.

[160] WL Bragg and JJ Thomson. *Diffraction of short electromagnetic waves.* In Proceedings of the Cambridge Philosophical Society: Mathematical and Physica Sciences, volume 17, page 43. Cambridge Philosophical Society, 1914.

[161] B Yacoubi, L Samet, J Bennaceur, A Lamouchi, and R Chtourou. Properties of transition metal doped-titania electrodes: *Impact on efficiency of amorphous and nanocrystalline dye sensitized solar cells*. Materials Science in Semiconductor Processing, 30:361–367, 2015.

[162] Coslimo Caro. *UV/Vis spectrophotometry–fundamentals and application.* Mettler-Toledo Publication, 2015.

[163] Patrycja Makuła, Michał Pacia, and Wojciech Macyk. *How to correctly determine the band gap energy of modified semiconductor photocatalysts based on UV–Vis spectra*, 2018.

[164] Sidney Perkowitz. *Optical characterization of semiconductors: infrared, Raman, and photoluminescence spectroscopy.* Elsevier, 2012.

[165] Edda E Neuteboom, Stefan CJ Meskers, EW Meijer, and Rene AJ Janssen. *Photoluminescence of self-organized perylene bisimide polymers*. Macromolecular Chemistry and Physics, 205(2):217–222, 2004.

[166] S Yasin, T Al Zoubi, and M Moustafa. *Design and simulation of high efficiency lead-free heterostructure perovskite solar cell using SCAPS-1D.* Optik, 229:166258, 2021.

[167] Marc Burgelman, Peter Nollet, and Stefaan Degrave. *Modelling polycrystalline semiconductor solar cells.* Thin Solid Films, 361:527–532, 2000.

[168] Michael G Helander, MT Greiner, ZB Wang, Wing Man Tang, and ZH Lu. *Work function of fluorine doped tin oxide.* Journal of Vacuum Science & Technology A, 29(1), 2011.

[169] Shiraishi, Masashi & Ata, Masafumi. (2001). *Work function of carbon nanotubes.* Carbon 39(12), 1913-1917. Carbon. 39. 1913-1917. 10.1016/S0008-6223(00)00322-5.

[170] Nina I Kovtyukhova and Thomas E Mallouk. *Nanowire p–n heterojunction diodes made by templated assembly of multilayer carbon-nanotube/polymer/semiconductor-particle shells around metal nanowires.* Advanced Materials, 17(2):187–192, 2005.

[171] B-S Jeong, DP Norton, and JD Budai. *Conductivity in transparent anatase TiO_2 films epitaxially grown by reactive sputtering deposition.* Solid-State Electronics, 47(12):2275–2278, 2003.

[172] Manish Kumar, Abhishek Raj, Arvind Kumar, and Avneesh Anshul. *An optimized lead-free formamidinium Sn-based perovskite solar cell design for high power conversion efficiency by SCAPS simulation.* Optical Materials, 108:110213, 2020.

[173] M Hirasawa, Teruya Ishihara, T Goto, K Uchida, and N Miura. *Magnetoabsorption of the lowest exciton in perovskite-type compound (CH_3NH_3) PbI_3.* Physica B: Condensed Matter, 201:427–430, 1994.

[174] Mingzhen Liu, Michael B Johnston, and Henry J Snaith. *Efficient planar heterojunction perovskite solar cells by vapour deposition.* Nature, 501(7467):395–398, 2013.

[175] James M Ball, Michael M Lee, Andrew Hey, and Henry J Snaith. *Low-temperature processed meso-superstructured to thin-film perovskite solar cells.* Energy & Environmental Science, 6(6):1739–1743, 2013.

[176] Samuel D Stranks, Giles E Eperon, Giulia Grancini, Christopher Menelaou, Marcelo JP Alcocer, Tomas Leijtens, Laura M Herz, Annamaria Petrozza, and Henry J Snaith. *Electron hole diffusion lengths exceeding 1 micrometer in an organometal trihalide perovskite absorber.* Science, 342(6156):341–344, 2013.

[177] Dmitry Poplavskyy and Jenny Nelson. *Nondispersive hole transport in amorphous films of methoxy-spirofluorene-arylamine organic compound.* Journal of Applied Physics, 93(1):341–346, 2003.

[178] Henry J Snaith and Michael Gratzel. *Electron and hole transport through mesoporous TiO_2 infiltrated with Spiro-OMeTAD.* Advanced Materials, 19(21):3643–3647, 2007.

[179] Armin Roshanghias, Gholamhossein Sodeifian, Ali Asghar Javidparvar, and Sara Tarashi. *Construction of a novel polytetrafluoroethylene-based sealant paste: The effect of polyvinyl butyral (PVB) and nano-alumina on the sealing performance and construction formulations*. Results in Engineering, 14:100460, 2022.

[180] Andrei A Bunaciu, Elena Gabriela Udri, STioiu, and Hassan Y Aboul-Enein. *X-ray diffraction: instrumentation and applications. Critical reviews in analytical chemistry,* 45(4):289– 299, 2015.

[181] Huanxin Peng, Zhenghua Su, Zhuanghao Zheng, Huabin Lan, Jingting Luo, Ping Fan, and Guangxing Liang. *High-quality perovskite $CH_3NH_3PbI_3$ thin films for solar cells prepared by single-source thermal evaporation combined with solvent treatment.* Materials, 12(8):1237, 2019.

[182] Namyoung Ahn, Dae-Yong Son, In-Hyuk Jang, Seong Min Kang, Mansoo Choi, and Nam-Gyu Park. *Highly reproducible perovskite solar cells with average efficiency of 18.3% and best efficiency of 19.7% fabricated via Lewis base adduct of lead (ii) iodide.* Journal of the American Chemical Society, 137(27):8696–8699, 2015.

[183] Zakir Hussain, Mohammad Mujahid, Ahmed Nawaz Khan, Syed Saad Javaid, and Amir Habib. *Low resistivity ZnO-go electron transport layer based $CH_3NH_3PbI_3$ solar cells.* AIP Advances, 6(6), 2016.

[184] Henry J Snaith, Antonio Abate, James M Ball, Giles E Eperon, Tomas Leijtens, Nakita K Noel, Samuel D Stranks, Jacob Tse-Wei Wang, Konrad Wojciechowski, and Wei Zhang. *Anomalous hysteresis in perovskite solar cells.* The Journal of Physical Chemistry Letters, 5(9):1511−1515, 2014.

[185] Qi Chen, Huanping Zhou, Ziruo Hong, Song Luo, Hsin-Sheng Duan, Hsin-Hua Wang, Yongsheng Liu, Gang Li, and Yang Yang. *Planar heterojunction perovskite solar cells via vapor-assisted solution process.* Journal of the American Chemical Society, 136(2):622−625, 2014.

[186] Dinkar V Aware and Shridhar S Jadhav. *Synthesis, characterization and photocatalytic applications of Zn-doped TiO_2 nanoparticles by sol−gel method.* Applied Nanoscience, 6(7):965−972, 2016.

[187] Gholamreza Gohari, Asghar Mohammadi, Ali Akbari, Sima Panahirad, Mohammad Reza Dadpour, Vasileios Fotopoulos, and Seisuke Kimura. *Titanium dioxide nanoparticles promote growth and ameliorate salinity stress effects on essential oil profile and biochemical attributes of dracocephalum moldavica.* Scientific Reports, 10(1):912, 2020.

[188] Abhilasha Sharma and Nandu B Chaure. *Studies on $CH_3NH_3PbI_3$ prepared by low-cost wet chemical technique.* Applied Physics A, 125:1−7, 2019.

[189] Arti Mishra, Zubair Ahmad, Farid Touati, RA Shakoor, and Mohammad Khaja Nazeeruddin. *One-dimensional facile growth of $MAPbI_3$ perovskite micro-rods.* RSC Advances, 9(20):11589−11594, 2019.

[190] Y Bouachiba, F Hanini, A Bouabellou, F Kermiche, A Taabouche, M Bouafia, S Amara, S Sahli, and K Boukheddaden. *TiO_2 thin films studied by FTIR, AFM and spectroscopic ellipsometry.* International Journal of Nanoparticles 11, 6(2-3):169−177, 2013.

[191] Wenhui Zhang, Yue Jiang, Yang Ding, Mingzhi Zheng, Sujuan Wu, Xubing Lu, Xinseng Gao, Qianming Wang, Guofu Zhou, Junming Liu, et al. *Solvent-induced textured structure and improved crystallinity for high performance perovskite solar cells.* Optical Materials Express, 7(7):2150−2160, 2017.

[192] Masaki Shirayama, Masato Kato, Takemasa Fujiseki, Shota Hara, Hideyuki Kadowaki, Daisuke Murata, Hiroyuki Fujiwara, Tetsuhiko Miyadera, Takeshi Sugita, and Masayuki

Chikamatsu. *Degradation mechanism of $CH_3NH_3PbI_3$ perovskite materials upon exposure to humid air.* Journal of Applied Physics, 119(11), 2016.

[193] Ruby Chauhan, Ashavani Kumar, and Ram Pal Chaudhary. *Structural and optical characterization of Zn doped TiO_2 nanoparticles prepared by sol–gel method.* Journal of sol-gel science and technology, 61:585–591, 2012.

[194] A Arunachalam, S Dhanapandian, C Manoharan, and G Sivakumar. *Physical properties of Zn doped TiO_2 thin films with spray pyrolysis technique and its effects in antibacterial activity.* Spectrochimica Acta Part A: Molecular and Biomolecular Spectroscopy, 138:105–112, 2015.

[195] AH Ghanbari Niaki, AM Bakhshayesh, and MR Mohammadi. *Double-layer dye-sensitized solar cells based on Zn-doped TiO_2 transparent and light scattering layers: Improving electron injection and light scattering effect.* Solar Energy, 103:210–222, 2014.

[196] Fahimeh Hajipour, Sedigheh Asad, Mohammad Ali Amoozegar, Ali Asghar Javidparvar, Jialun Tang, Haizheng Zhong, and Khosro Khajeh. *Developing a fluorescent hybrid nanobiosensor based on quantum dots and azoreductase enzyme for methyl red monitoring*. Iranian Biomedical Journal, 25(1):8, 2021.

[197] Esraa A Al-Oubidy and Firas J Kadhim. *Photocatalytic activity of anatase titanium dioxide nanostructures prepared by reactive magnetron sputtering technique.* Optical and Quantum Electronics, 51:1–11, 2019.

[198] Sung Bum Park, Won Hoon Jung, Ki Young Kim, and Byumseok Koh. *Toxicity assessment of SiO_2 and TiO_2 in normal colon cells, in vivo and in human colon organoids.* Molecules, 25(16):3594, 2020.

[199] Raghvendra S Dubey, Sandesh R Jadkar, and Ajinkya B Bhorde. *Synthesis and characterization of various doped TiO_2 nanocrystals for dye-sensitized solar cells.* ACS Omega, 6(5):3470–3482, 2021.

[200] Manasi Manoj Karkare. *Estimation of band gap and particle size of TiO_2 nanoparticle synthesized using sol gel technique.* In 2014 International Conference on Advances in Communication and Computing Technologies (ICACACT 2014), pages 1–5. IEEE, 2014.

[201] Tanya M Breault and Bart M Bartlett. *Lowering the band gap of anatase-structured TiO_2 by co-alloying with Nb and the electronic structure and photocatalytic degradation of methylene blue dye.* The Journal of Physical Chemistry C, 116(10):5986–5994, 2012.

[202] Xiaotao Liu, Zhenhua Wu, Yiqiang Zhang, and Christos Tsamis. *Low temperature Zn doped TiO_2 as electron transport layer for 19% efficient planar perovskite solar cells.* Applied Surface Science, 471:28–35, 2019.

[203] Asma M Alturki and Rachid Ayad. *Synthesis and characterization of titanium dioxide nanoparticles with a dosimetry study of their ability to enhance radiation therapy using a low energy x-ray source.* Indian Journal of Science and Technology, 12:1–5, 2019.

[204] Khin Phyu Tun. *XRD and SEM analysis, and semiconductor type determination of TiO_2 for dye-sensitized solar cell.* Science, 4(2):103–107, 2019.

[205] MI Khan, Mudassar Sabir, Ghulam M Mustafa, Mahvish Fatima, Asif Mahmood, Samar A Abubshait, Haya A Abubshait, and Munawar Iqbal. *300 keV cobalt ions irradiations effect on the structural, morphological, optical and photovolatic properties of Zn doped TiO_2 thin films based dye sensitized solar cells*. Ceramics International, 46(10):16813–16819, 2020.

[206] Burak Unlu, Soner Cakar, and Mahmut Ozacar. *The effects of metal doped TiO_2 and dithizone-metal complexes on DSSC performance.* Solar Energy, 166:441–449, 2018.

[207] Weiguang Kong, Zhenyu Ye, Zhen Qi, Bingpo Zhang, MiaoWang, Arash Rahimi-Iman, and Huizhen Wu. *Characterization of an abnormal photoluminescence behavior upon crystal phase transition of perovskite $CH_3NH_3PbI_3$.* Physical Chemistry Chemical Physics, 17(25):16405–16411, 2015.

[208] Yasuhiro Yamada, Toru Nakamura, Masaru Endo, Atsushi Wakamiya, and Yoshihiko Kanemitsu. *Near-band-edge optical responses of solution-processed organic–inorganic hybrid perovskite $CH_3NH_3PbI_3$ on mesoporous TiO_2 electrodes.* Applied Physics Express, 7(3):032302, 2014.

[209] Ali D Husainat. *Simulation and design implementation of low-cost and high-efficiency perovskite solar cells.* PhD thesis, Roy G Perry College of Engineering Prairie View A&M University, 2020.

[210] Caleb C Boyd, Rongrong Cheacharoen, Tomas Leijtens, and Michael D McGehee. *Understanding degradation mechanisms and improving stability of perovskite photovoltaics.* Chemical Reviews, 119(5):3418–3451, 2018.

[211] R Jeyakumar, Atanu Bag, Reza Nekovei, and R Radhakrishnan. *Influence of electron transport layer (TiO_2) thickness and its doping density on the performance of $CH_3NH_3PbI_3$ based planar perovskite solar cells.* Journal of Electronic Materials, 49:3533–3539, 2020.

[212] Goutam Paul, Soumyo Chatterjee, Hrishikesh Bhunia, and Amlan J Pal. *Self-doping in hybrid halide perovskites via precursor stoichiometry: to probe the type of conductivity through scanning tunnelling spectroscopy*. The Journal of Physical Chemistry C, 122(35):20194–20199, 2018.

[213] Ghazi Aman Nowsherwan, Muhammad Aamir Iqbal, Sajid Ur Rehman, Aurang Zaib, Muhammad Irfan Sadiq, Muhammad Ammar Dogar, Muhammad Azhar, Siti Sarah Maidin, Syed Sajjad Hussain, Kareem Morsy, et al. *Numerical optimization and performance evaluation of ZnPc: Pc70bm based dye-sensitized solar cell.* Scientific Reports, 13(1):10431, 2023.

[214] Sajid Sajid, Salem Alzahmi, Imen Ben Salem, Jongee Park, and Ihab M Obaidat. *Lead-free perovskite homojunction-based HTM -free perovskite solar cells: Theoretical and experimental viewpoints*. Nano Materials, 13(6):983, 2023.

[215] Qingdong Ou, Xiaozhi Bao, Yinan Zhang, Huaiyu Shao, Guichuan Xing, Xiangping Li, Liyang Shao, and Qiaoliang Bao. *Band structure engineering in metal halide perovskite nanostructures for optoelectronic applications.* Nano Materials Science, 1(4):268–287, 2019.

[216] SKM Iftiquar and Junsin Yi. *Numerical simulation and light trapping in perovskite solar cell.* Journal of Photonics for Energy, 6(2):025507–025507, 2016.

[217] Sonam Tripathi, Brijesh Kumar, and DK Dwivedi. *Numerical simulation of non-toxic In_2S_3/SnS_2 buffer layer to enhance CZTS solar cells efficiency by optimizing device parameters*. Optik, 227:166087, 2021.

[218] Anastasios Arvanitopoulos, Neophytos Lophitis, Konstantinos N Gyftakis, Samuel Perkins, and Marina Antoniou. *Validated physical models and parameters of bulk 3C–SiC aiming for credible technology computer aided design (TCAD) simulation.* Semiconductor Science and Technology, 32(10):104009, 2017.

[219] Malika Tridane, Abdessamad Malaoui, and Said Belaaouad. *Numerical simulation of GaAs photovoltaic cell using SCAPS-1D,* 2022.

[220] H El Farri, M Bouachri, M Fahoume, A Frimane, and O Daoudi. *Theoretical simulation of ZnS buffer layer thin films with SCAPS-1D software for photovoltaic applications.* Chalcogenide Letters, 18(8), 2021.

[221] Viorica Stancu, Andrei Gabriel Tomulescu, Lucia Nicoleta Leonat, Liliana Marinela Balescu, Aurelian Catalin Galca, Vasilica Toma, Cristina Besleaga, Sarah Derbali, and Ioana Pintilie. *Partial replacement of dimethylformamide with less toxic solvents in the fabrication process of mixed-halide perovskite films*. Coatings, 13(2):378, 2023.

[222] Alexander James Doolin, Rhys Gareth Charles, Catherine SP De Castro, Rodrigo Garcia Rodriguez, Emmanuel Vincent Pean, Rahul Patidar, Tom Dunlop, Cecile Charbonneau, Trystan Watson, and Matthew Lloyd Davies. *Sustainable solvent selection for the manufacture of methylammonium lead triiodide ($MAPbI_3$) perovskite solar cells.* Green Chemistry, 23(6):2471–2486, 2021.

[223] Md Ferdous Rahman, Jaker Hossain, Abdul Kuddus, Md Mahabub Alam Moon, and Abu Bakar Md Ismail. *Effect of Triton X-100 surfactant on thiol-amine co-solvents assisted facile synthesized CdS thin films on glass substrate by spin coating method.* SN Applied Sciences, 2:1–12, 2020.

[224] Dong In Kim, JiWon Lee, Rak Hyun Jeong, and Jin-Hyo Boo. *A high-efficiency and stable perovskite solar cell fabricated in ambient air using a polyaniline passivation layer.* Scientific Reports, 12(1):697, 2022.

[225] Ershad Parvazian, Amir Abdollah-zadeh, Mahdi Dehghani, and Nima Taghavinia. *Photovoltaic performance improvement in vacuum-assisted meniscus printed triple-cation mixed-halide perovskite films by surfactant engineering*. ACS Applied Energy Materials, 2(9):6209–6217, 2019.

[226] Kisu Lee, Kyung Hee Cho, Jaehoon Ryu, Juyoung Yun, Haejun Yu, Jungsup Lee, Wonjoo Na, and Jyongsik Jang. *Low-cost and efficient perovskite solar cells using a surfactant modified polyaniline: poly (styrenesulfonate) hole transport material.* Electrochimica Acta, 224:600–607, 2017.

[227] Meidan Que, Boyue Zhang, Jin Chen, Xingtian Yin, and Sining Yun. *Carbon-based electrodes for perovskite solar cells.* Materials Advances, 2(17):5560–5579, 2021.

Appendix A

Paper Publication

Indonesian Journal of Electrical Engineering and Computer Science
Vol. 34, No. 3, June 2024, pp. 1410~1419
ISSN: 2502-4752, DOI: 10.11591/ijeecs.v34.i3.pp1410-1419

Fabrication and characterization of methylammonium lead iodide-based perovskite solar cells under ambient conditions

Dwayne Jensen Reddy[1], Ian Joseph Lazarus[2]
[1]Department of Electrical Power Engineering, Durban University of Technology, Durban, South Africa
[2]Department of Physics, Faculty of Applied Sciences, Durban University of Technology, Durban, South Africa

Article Info

Article history:

Received Feb 2, 2023
Revised Dec 11, 2023
Accepted Feb 16, 2024

Keywords:

Bandgap
Electron transport layer
Methyl ammonium lead iodide
Perovskite solar cells
Titanium dioxide

ABSTRACT

This study investigated the fabrication and characterization of $CH_3NH_3PbI_3$ based perovskite solar cells (PSCs) using the one-step spin coating technique under ambient conditions, eliminating the need for expensive glovebox and thermal evaporation equipment. The perovskite layer was annealed at 65 °C for 30 seconds and 100 °C for 30 seconds, 1 and 2 minutes. The scanning electron microscope (SEM) images show a smooth and uniform surface coverage for the ETL and $CH_3NH_3PbI_3$ layers. SEM results also show an average grain size of 397 nm for $CH_3NH_3PbI_3$ and an average particle size of ~17 nm for TiO_2 was confirmed by transmission electron microscopy (TEM). X-ray diffraction (XRD) results confirmed the formation of tetragonal perovskite ($CH_3NH_3PbI_3$) phase with high crystallinity with a crystallite size of 19.99 nm for the samples annealed for 30 seconds at 65 °C and 1 min at 100 °C. FTIR results also confirmed the presence of anatase TiO_2 at wavenumber 438 cm^{-1} and the formation of the adduct of Pb_2 with dimethyl sulfoxide (DMSO) and MAI is confirmed at 1,015 cm^{-1}. From the Tauc plot the bandgap energy of TiO2 and Perovskite layers was determined to be 3.52 eV and 2.06 eV respectively. An open-circuit voltage was 0.9057 V and short circuit current density was 12.2185 mA/cm^2 with a fill factor of 48.05 and power conversion efficiency (PCE) of 5.199%.

Corresponding Author:

Ian Joseph Lazarus
Department of Physics, Faculty of Applied Sciences, Durban University of Technology
Durban, South Africa
Email: lazarusi@dut.ac.za

1. INTRODUCTION

Perovskite solar cells (PSC) has attracted much interest in recent years from researchers due to its potential as a next generation thin film solar technology. The attract features of PSC include high efficiency, low manufacturing costs, versatility and flexibility. This opens up the possibilities of applications in building integrated photovoltaics (BIPV), wearable electronics and integration into curved or irregular shaped structures.

The absorbing material of PSC devices with the generic crystal structure ABX_3 is referred to as perovskite [1]. So far, the most efficient PSC devices have been created using the following materials in the perovskite form of ABX_3 with methyl ammonium (CH_3NH_3) as (A), metal like lead (Pb) or tin (Sn) as (B), and a halide bromide (Br_3), iodide (I_3), or chloride (Cl_3) as X_3 [2]. This perovskite material has the following attractive features: a low bandgap that allows lighter to be absorbed, a high carrier charge mobility that allows the created electron and hole to move through the material without much resistance, and a high diffusion length that prevents electron-hole pair recombination [3].

As depicted in Figure 1, light is transmitted through the fluorine doped tin-oxide (FTO) and electron transport layer (TiO_2) and absorbed by the perovskite layer to cause charge separation. This process excites an electron into the conduction band and creates a hole (positive charge) in the valence band. While the electrons are injected into the electron-transport layer and the holes into the hole-transport layer (Spiro-OMeTad), the positive holes in the cathode layer are filled by the electrons after they have passed via an external circuit. As shown in Figure 1, a closed-circuit cell is created by connecting the transparent FTO electrode and the rear contact metal electrode [4], [5].

With a record PCE of 22.1%, metal halide perovskite (MHP) solar cells have shown the fastest rate of improvement in power conversion efficiency (PCE) among all photovoltaic technologies to date. MHP solar cells are now as efficient as silicon solar cells [6]. Additionally, earth-abundant compositions and inexpensive solution processing techniques can be used to create MHP solar cells. As a result, they have a stronger chance of realizing more competitive solar cell power technology from an economic perspective [7].

Much of the improvements to the performance of perovskite can be attributed to the refinement of the perovskite layer fabrications protocols. There have been several techniques developed such as the one-step, two-step spin coating solution method, solvent engineering method, anti-solvent engineering method as well as vacuum and vapor-assisted methods. The spin coating solution method is considered the most affordable deposition technique for research purposes which allows for fairly uniform surface coverage. Both the one and two-step deposition techniques for $CH_3NH_3PbI_3$ were investigated by Ahn *et al.* [8] and Im *et al.* [9]. Ahn *et al.* [8] showed that for the one-step method, the $CH_3NH_3PbI_3$ perovskite precursor solution was annealed at 40 °C for 3 min and 100 °C for 5 min to obtain a PCE of 7.5%. For the two-step method under the same annealing setting Im *et al*. [9] achieved a PCE of 13.9%. For a similar $CH_3NH_3PbI_3$ perovskite precursor composition, Ozaki *et al.* [10] achieved a PCE of 20.3% using the one-step method with an annealing setting of 40 °C for 5 min, 55 °C for 5 min, and 75 °C for 5 min and 100 °C for 30 minutes. By applying an anti-solvent during the last 2 seconds of the perovskite spin coating stage the desired high crystalline formation of tetragonal crystal structure perovskite was formed. Regardless of the method, a high degree of crystallinity, flat and dense perovskite layers are critical for low surface defects, energy losses, and high-power conversion efficiency. These characteristics play a vital role in minimizing the formation of pinholes and short-circuiting of the PSC device. However high efficiency and reproducible PSCs are fabricated using expensive deposition equipment, a clean room, glovebox, and thermal evaporation equipment which can limit research in the development of PSCs.

It is within this context of varying reports of annealing time at 100 °C that we focused on the widely used $CH_3NH_3PbI_3$ as the perovskite material developed with the one-step spin coating method and anti-solvent technique for an investigation into the crystal structure and performance under different annealing settings. The perovskite layer was annealed under three different settings of 65 °C for 30 s and 100 °C for 30 s, 65 °C for 30 s and 100 °C for 1 minute and 65 °C for 30 s and 100 °C for 2 minutes under ambient conditions. Modified spin coating parameter setting, perovskite annealing setting, and vacuum storage are provided to reliably fabricate and reproduce PSCs. After applying these methods a maximum PCE of 5.199% was achieved with reliabilty and reproducibility. The paper structure is as follows; in section 2 the fabrication method is presented. In section 3 we present the perfomance results and discussion of the characterization techniques used to determine the structural, morphological and optical properties. Our observations and recommendations are concluded in section 4.

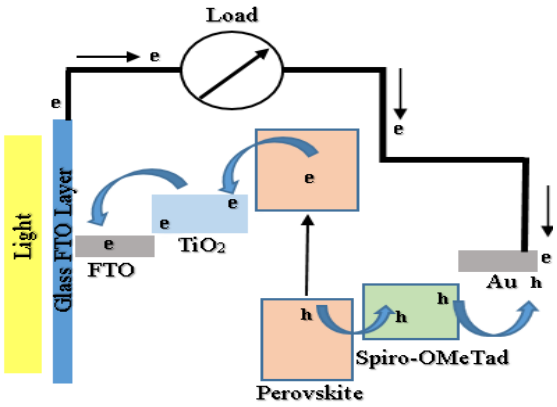

Figure 1. Typical PSC planar architecture and operation

2. CHEMICALS AND FABRICATION METHOD

2.1. Chemicals

The electron transport layer consisted of Titanium isopropoxide (TTIP), ethanol (EtOH, super dehydrated,) and hydrochloric acid (HCL). The perovskite absorber layer consisted of Methyl ammonium iodide (MAI, 99%), Lead (II) Iodide (PbI_2, 99.9%), dimethylformamide (DMF, super hydrated), dimethyl-sulfoxide (DMSO, super hydrated), di-ethyl ether. The hole transport layer consisted of 2, 2', 7, 7'-Tetrakis (N, N-di-p-methoxyphenylamino)-9, 9'- Spirobifluorene (Spiro- OMeTAD powder), 4- Tert – Butylpyridine (TBP, 96%), Bis (triflouromethane sulfonimide lithium salt (LiTFSI), chlorobenzene. All chemicals were purchased from Sigma- Aldrich Co.

2.2. Device fabrication

All layers of the PSC shown if Figure 2 were fabricated under ambient conditions, relative humidity was maintained at < 65% at a controlled room temperature of (~20°C) and was adapted and modified from [8]–[10]. Step 1: Fluorine-doped tin oxide glass substrates (25 mm x 25 mm) were cleaned in beakers containing detergent and deionized water, and ultrasonically cleaned in ethanol for 20 minutes at 80 °C. Substrates were carefully removed and rinsed in deionized water, dried on a hotplate and then placed in a UVO cleaner for 15 minutes for further cleaning before depositing the TiO_2 layer. A piece of tape was placed 5 mm from the top edge, leaving the front FTO anode contact exposed and leaving 20 mm x 20 mm space available for the depositing of the precursor solutions.

Step 2: the 0.22M, TiO_2 electron transport layer precursor solution was prepared by vigorously stirring 14.29 ml of ethanol and 0.28 ml of 2M HCL on a magnetic stirrer for 30 minutes, 1 ml of TTIP was added dropwise to this solution and was allowed to stir vigorously for 2 hours at room temperature. The TiO_2 precursor solution was then filtered using a 0.45 µm Teflon filter before spin coating to ensure the solution was free of any undissolved particles thus ensuring a smooth and uniform surface coverage was obtained. The 300 µl TiO_2 solution was dynamically spin-coated on the UVO-treated FTO at 1000 rpm for 15 seconds and annealed to 550 °C for 30 minutes to form a transparent, smooth, and homogeneous electron transport thin film layer as shown in Figure 2(a).

For the synthesis of the TiO_2 nanoparticles, the remaining 0.22 M solution was then left to age for ~72 days until a clear and transparent gel is formed. The gel was placed in a hot air dryer for 12 hours at a temperature of 80 °C to form a dry TiO_2 powder. The dried TiO_2 powder is then placed in a furnace and heated to 550 °C for 30 minutes to form anatase TiO_2 nanoparticles for Fourier transform infrared spectroscopy (FTIR), X-ray diffraction (XRD), and transmission electron microscopy (TEM) characterization.

Step 3: the perovskite absorber layer was prepared by dissolving 0.16 g methyl ammonium iodide and 0.46 g lead iodide into 0.08 ml dimethyl sulfoxide (DMSO) and 0.6 ml DMF. This was stirred for ~24 hours to ensure a homogenous solution before deposition onto the TiO_2 layer. The TiO_2 layer was UVO treated again for 15 minutes before spin-coating 250 µl of the perovskite solution at 5000 rpm for 15 seconds with 350 µl of di-ethyl ether slowly dripped from approximately 2cm away from the rotating substrate during the last 5 seconds. The coated surface was placed on a digital hotplate at 65 °C for 30 seconds then slowly ramped up to 100 °C and annealed for 1 minute to form the dark brown and transparent perovskite layer shown in Figure 2(b). This was then transferred immediately into a vacuum desiccator before deposition of the hole transport layer (HTL) to minimize the effects of degradation of the perovskite layer due to humidity.

Step 4: the HTL was prepared by dissolving 0.52 g of LiTFSI in 1 ml acetonitrile and stirred vigorously for 10 minutes to form the LiTFSI stock solution. Then 0. 07g of Spiro-OMeTAD powder was added to 1 ml chlorobenzene and stirred vigorously for 10 minutes to form the Spiro-OMeTAD solution. Thereafter 0. 03 ml of tBP and 0. 02 ml of the LiTFSI solution was added to the Spiro-OMeTAD solution and stirred for 30 minutes to form the HTL precursor solution. Lastly, 200 µl of the HTL solution was dynamically spin-coated on top of the perovskite layer at 1000 rpm for 15 seconds and placed in a vacuum desiccator to oxidize overnight, before the immediate application of 8 mg activated carbon powder and FTO as the back conductive cathode contact (steps 5 & 6) with binder clips to hold the PSC together shown in Figure 2(c). This allowed minimum exposure of our cells to environmental conditions and performance reduction. The complete step-by-step fabrication is shown in Figure 2(d).

2.3. Characterization equipment

The identification of the functional groups was acquired by Agilent Cary 630 attenuated total refl ectance-Fourier transform infrared (ATR-FTIR) using a diamond crystal operating between 400-4000 cm^{-1}. The X-Ray Diffractometer, model: D8 Advanc, make: M/s Bruker AXS, Germany was used to determine the perovskite structure. The surface morphology properties and elemental percentage concentration was

characterized by the Zeiss scanning electron microscope (SEM) operating at 40 kV and 40 mA and energy dispersive X-Ray (EDX). Particle size was determined by TEM using Image J software. The optical properties were obtained by the agilent cary 60 UV-Vis-NIR spectrometer. Bandgaps were calculated using the TAUC plot with a direct bandgap power factor. The photovoltaic properties were measured with a Keithley 2460 source measuring unit and an illumination light source of AM 1.5 (100 mW/cm^2).

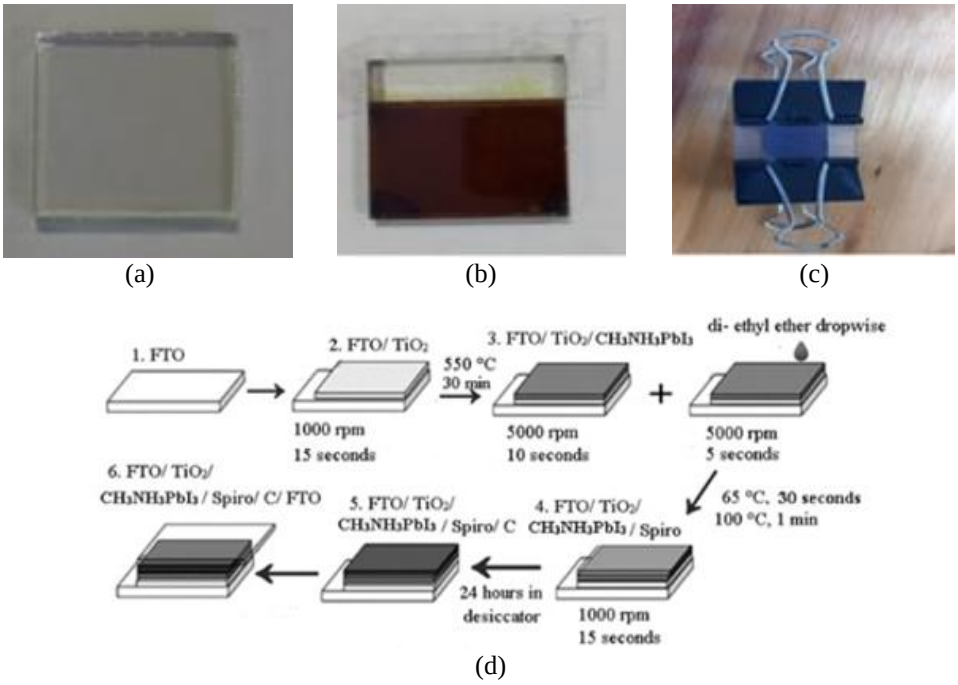

Figure 2. Perovskite solar cell fabrication; (a) TiO_2 spin coated on FTO glass substrate, (b) methyl ammonium lead iodide spin-coated and annealed on TiO_2 layer, (c) completed PSC, and (d) fabrication steps of PSC

3. RESULTS AND DISCUSSION

3.1. X- Ray diffraction: structural properties of $CH_3NH_3PbI_3$

The XRD results of perovskite films annealed at 65 °C for 30 seconds and then annealed at 100 °C for 30 s, 1min, and 2 minutes are presented in Figure 3. Strong peaks at 14.06° (110), 28.15° (220) and 31.68° (312) indicate the formation of tetragonal perovskite ($CH_3NH_3PbI_3$) phase [11] with high crystallinity for the samples annealed for 30 sec and 1 min. This verified the annealing settings of the work done by Ahn *et al.* [8] and was used for further characterization of the material's properties. According to Figure 3 the lead iodide phase in the XRD pattern of the sample annealed for 30 sec may be due to the residual phase from preparation which remains within the bulk of the material. In other words, the annealing time was not sufficient to completely convert the precursors to the perovskite phase. For the sample annealed for 2 min, the peaks at 13.59° (001), 27.58° (101), 30.49° (102), 43.52° (111), 50.17° (201), and 73.57° (105) correspond to hexagonal lead iodide phase (JCPDS No. 07-0235) [12]. The PbI_2 phase is formed due to the decomposition of the perovskite phase upon annealing at 100 °C, where methyl ammonium iodide (CH_3NH_3I) escaped from the Perovskite film to form lead iodide by heating for a longer time (2 min). It was found previously that during the annealing process, CH_3NH_3I can escape if annealed too long ,especially for some loosely bonded Perovskite phases [13], [14].

The average crystallite size of the under-studied samples was calculated by resolving the characteristic peaks using Debye-Scherer's formula [15]:

$$D = K\lambda / \beta \cos(\theta) \quad (1)$$

where K is the shape factor (0.9), D is the average crystallite size, β is the half-width of the measured diffraction peak, θ is the diffraction angle, and λ is the X-ray wavelength (0.154 nm). The crystallite size for the perovskite phase was equal to 14.32 nm and 19.99 nm for the samples annealed at 65 °C for 30 s and 100 °C for 30 s and 65 °C for 30 s and 100 °C for 1 min, respectively. In addition, the crystallite size of the PbI_2 phase in the sample annealed at 65 °C for 30 s and 100 °C for 2 min was 12.21 nm. The more intense

characteristic peaks and larger average crystal size after 65 °C for 30 s and 100 °C for 1 min annealing time attributed to the improved crystallinity or composition homogeneity with fewer low-dimensional defects and less scattering between grain boundaries in the solvent-annealed perovskite film.

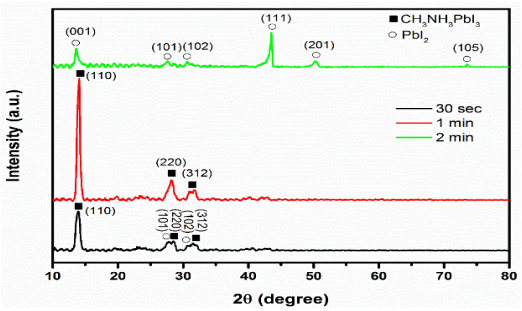

Figure 3. XRD patterns of Perovskite films annealed at 65 °C for 30 s and 100 ˚C for 30 sec, 65 °C for 30 s and 100 ˚C for 1 min, 65 °C for 30 s and 100 ˚C for 2 min

3.2. Fourier transform infrared spectroscopy: identification of functional groups

In the FTIR spectrums shown in Figure 4, it can be seen from Figure 4(a) that there is no presence of O-H hydroxyl groups, in the range of wavenumber 3100-3600 cm^{-1} which can be attributed to the high calcination temperature of 550 °C. The hydroxyl groups could interact with the NH_4 and CH_3 in the perovskite causing the decomposition of $CH_3NH_3PbI_3$ into PbI_2 and CH_3NH_3I which will lead to reduced performance of the PSC. The sharp peaks between 528-408 cm^{-1} indicate that the thin film is well crystallized and is assigned to O-Ti-O bonding. The sharp peak at 438 cm^{-1} is characteristic of TiO_2 anatase [16]–[19].

FTIR spectroscopy was conducted to identify $CH_3NH_3Pb_2I$ formation. The FTIR spectra in Figure 4(b) feature vibrational modes at 3116 cm^{-1} (N-H stretch), 3116-1569 cm^{-1} (C-H stretch), 1569 cm^{-1} (antisymmetric NH_3^+), 1458 cm^{-1} (symmetric NH_3^+bend) ,1015 cm^{-1} (MAI·PbI_2·DMSO) 950 cm^{-1} (C-N stretch) and 907 cm^{-1} (NH_{3+}/CH_3 rock) which is similar to related literature [19]–[23]. The adduct of Pb_2 with DMSO and MAI is confirmed by FTIR spectroscopy at 1015 cm^{-1}.

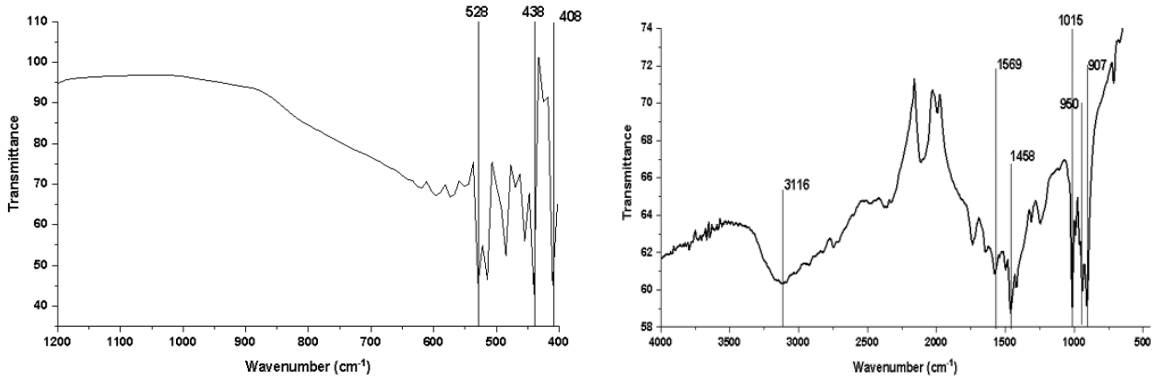

(a) (b)

Figure 4. FTIR spectra (a) FTIR spectra of planar TiO_2 thin film annealed at 550 °C and (b) FTIR spectra of perovskite thin film

3.3. SEM, TEM and EDX: morphological properties and elemental weight percentage compositions

The surface morphology and particle size of the TiO_2 layer shown in Figure 5. Figure 5(a) was observed by scanning electron microscope. The surface morphology of the thin films annealed at 550 °C under ambient conditions showed a relatively uniform surface coverage with densely packed TiO_2 nanoparticles confirmed by the TEM results shown in Figure 5(b). Figure 5(c) shows the morphology and size distribution of the TiO_2 nanoparticles ranging from 5 to 30 nm. To characterize the surface roughness of the TiO_2 and Perovskite layers, the image J software tool was utilized on the SEM images. The estimated root

mean square (RMS) roughness of 21.9 nm was obtained for the TiO_2 layer indicating a fairly smooth layer coverage; however, an ultra-smooth surface is imperative to achieve better performance as reported by [24], [25]. This allows for a smoother surface for the deposition of the perovskite layer and minimizes the formation of defects. The histogram in Figure 5(d) shows that the average particle size of TiO_2 nanoparticles synthesized was ~ 17 nm.

The SEM images of the $CH_3NH_3PbI_3$ thin film and elemental composition is presented in Figure 6. Figure 6(a) shows a dense and well-interconnected layer with particle sizes ranging from 50 nm to 800 nm with an average particle size of 397 nm shown in Figure 6(b). The estimated root mean square (RMS) roughness of 31.75 nm shown if Figure 6(c) was obtained for the Perovskite layer. Highly dense $CH_3NH_3PbI_3$ films were formed by the rapid evaporation of DMF with diethyl ether while spinning for the last 5 seconds [10]. Energy dispersive X-ray spectrometry analysis of FTO/TiO_2/$CH_3NH_3PbI_3$ thin films was performed to determine and identify the elemental composition and weight percentage (wt %) concentrations. Figure 6(d) shows peaks for Ti, O, Sn, I, Pb. The presence of Si is due to the FTO-coated quartz substrate used; no other impurities are seen.

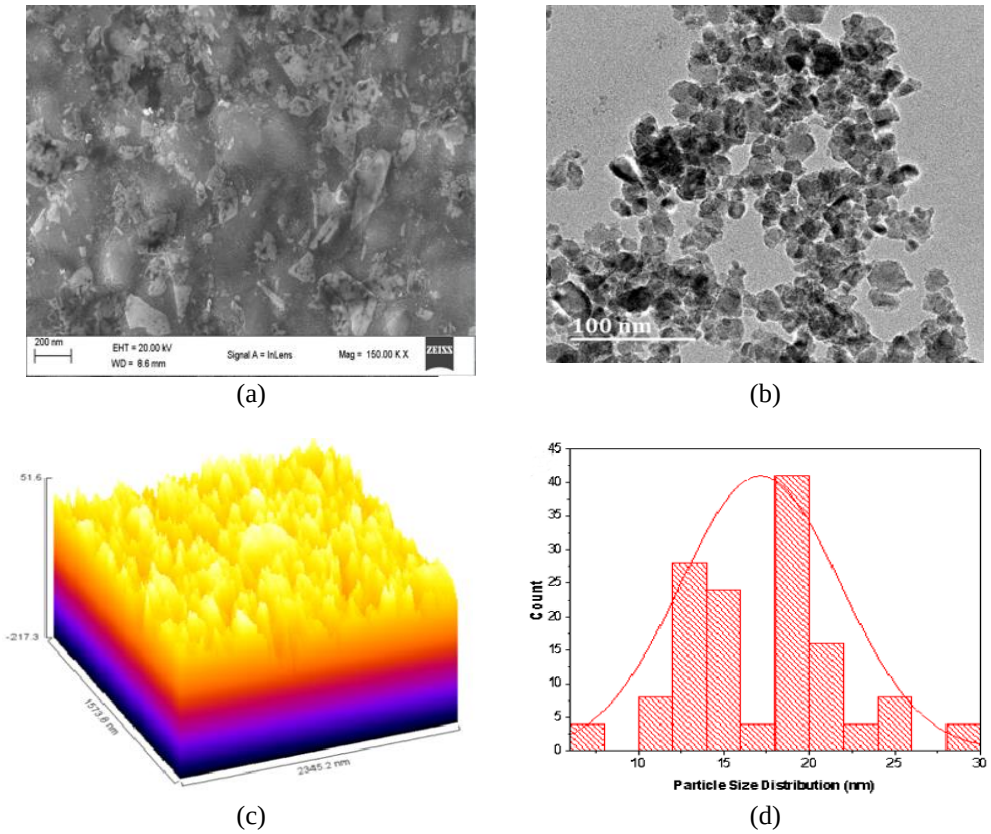

Figure 5. Surface and particle imaging of TiO_2; (a) SEM image of TiO_2 surface layer, (b) TEM image of TiO_2 nanoparticles, (c) surface roughness of TiO_2 layer, and (d) TiO_2 nanoparticle size distribution

3.4. UV-Vis spectroscopy: optical properties

The UV-Vis transmission and absorption spectra shown in Figure 7 were obtained using a Cary 60 UV-Vis. Figure 7(a) shows the UV-VIS transmission spectra of the FTO and TiO_2 thin films. The UV–Vis transmission spectra for the TiO_2 thin film indicate a ~10% drop in transmission from ~80% for FTO to ~70% from the visible light to near-infrared regions. The TiO_2 layer has a significantly lower absorbance in the 300 nm to 800 nm wavelength range as expected when compared to the perovskite layer. The UV–Vis absorption spectra in Figure 7(b) shows a redshift to near infrared in the absorption range with the introduction of the perovskite layer. The $CH_3NH_3PbI_3$ shows good light absorption with a bandgap of ~2.06 eV from the visible light to near-infrared regions. The decrease in bandgap and increase in fermi energy allows electrons to move more freely from the valence to the conduction band. The bandgap (Eg) of the thin film samples was calculated using the Tauc plot method. The bandgap energy of 3.52 eV for TiO_2 and 2.06 eV for perovskite was measured by plotting $(a/hv)^2$ as a function of photon energy, and extrapolating the linear region of the absorption curve as shown in Figure 7(c).

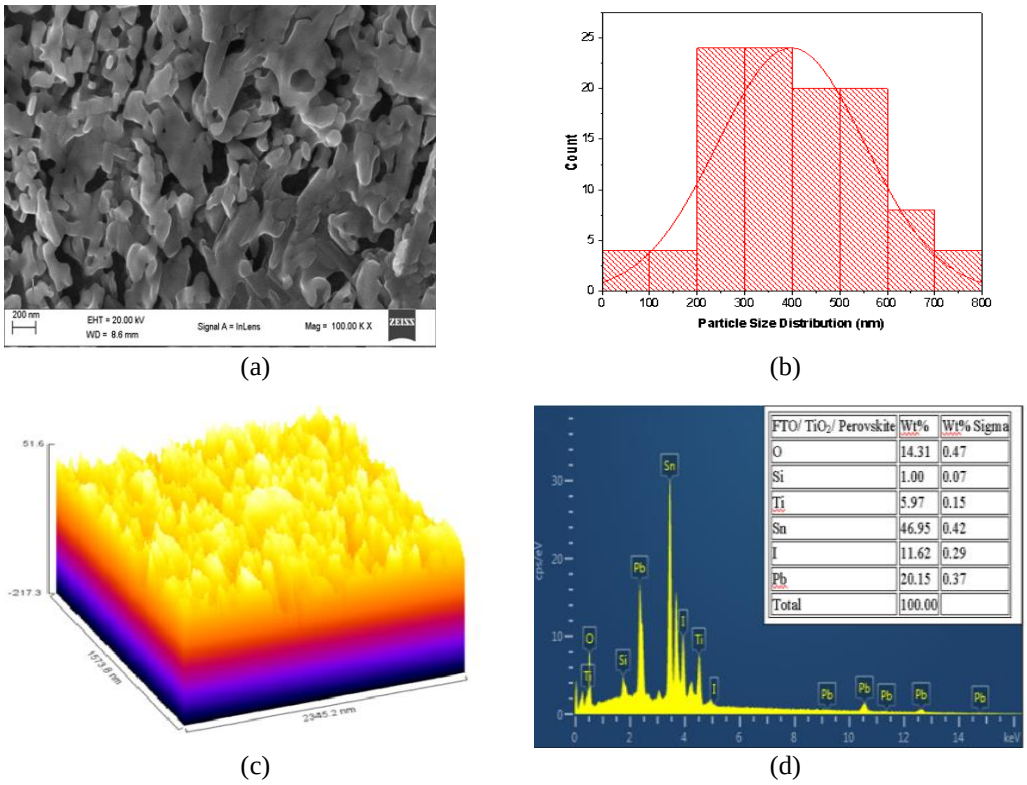

Figure 6. Perovskite surface and elemental composition; (a) SEM image of the Perovskite surface layer, (b) perovskite particle size distribution, (c) surface plot of Perovskite layer, and (d) elemental composition of the FTO/TiO_2/Perovskite layers

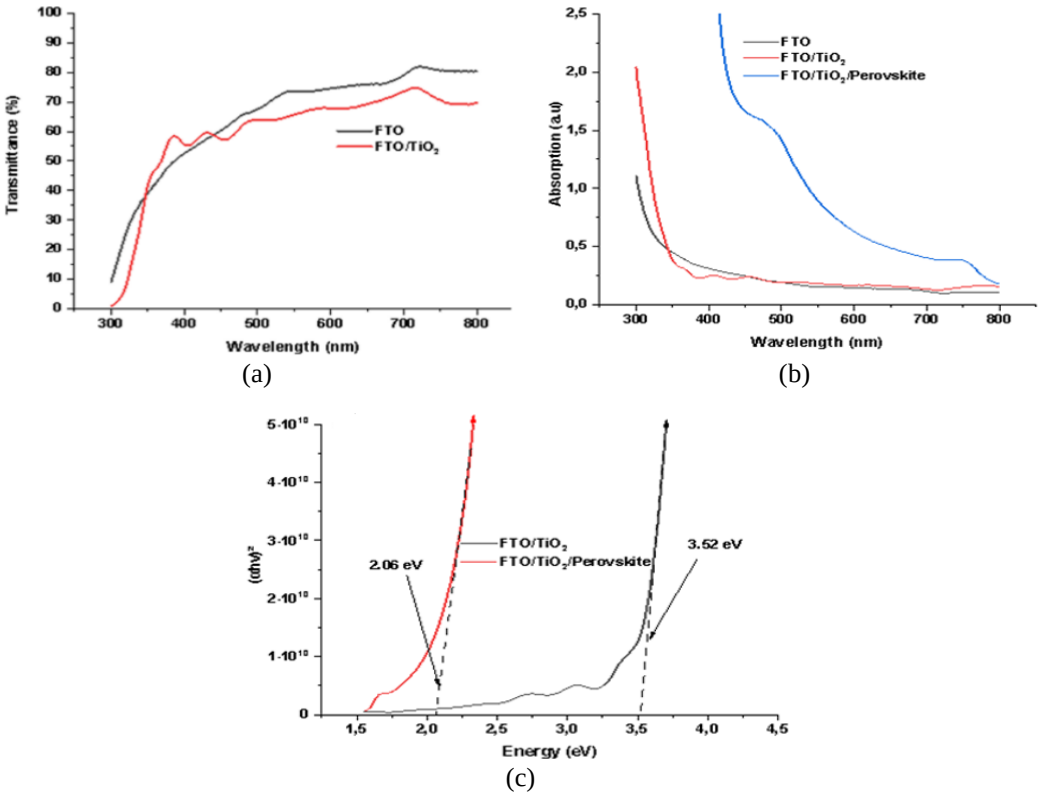

Figure 7. UV-Vis spectra; (a) transmission spectra FTO and FTO/ TiO_2 layer, (b) absorption spectra of FT0, FTO/TiO_2 and FTO/TiO_2/Perovskite, and (c) band gap energy of TiO_2 and Perovskite material

3.5. PSC performance

The open-circuit voltage (when current is zero), short-circuit current density (when voltage is zero), the voltage at maximum power point (V_{mpp}), and current density at maximum power point (J_{mpp}) values serve as important electrical parameters in determining the efficiency of converting sunlight to electricity in a solar cell. The performance measurements shown in Figure 8 were taken using a Kiethley 2460 source measuring unit at one sun (100 mW/cm^2). The solar cell device described was tested on an active area 0.1 cm^2 and gave an open-circuit voltage (V_{oc}) of 0.9057 V, short circuit current density up to 12.2185 mA/cm^2, PCE of 5.199% and fill factor of 48.05 was achieved in our device, compared to the fabrication of a vapour-assisted PSC solar cell under similar conditions of 0.972 V, 17. 5 mA/cm^2, PCE of 11%, and fill factor of 65.2 [26]. The voltage and current density at the maximum power point were 0.5763 V and 9.8213 mA/cm^2 respectively, resulting in a maximum power output of 5.2 mW. Energy losses in voltage and current occur due to the method of deposition, surface defects, increasing internal recombination of charge carriers, and bandgap misalignment between the ETL- Perovskite-HTL interfaces limiting charge transport,V_{oc} and PCE [27].

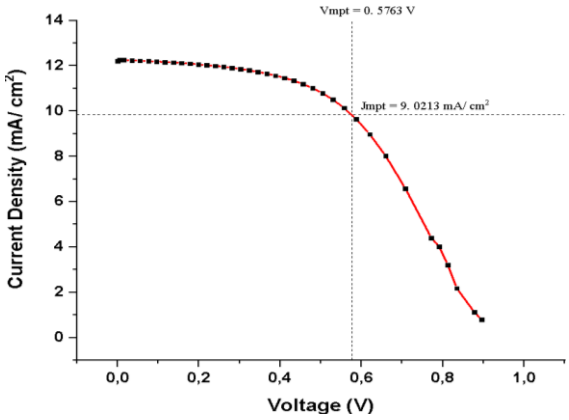

Figure 8. J-V curve for PSC

4. CONCLUSION

It has been shown that PSCs can be fabricated without expensive equipment under ambient conditions by carefully considering ambient and process parameters. In order to ensure the reliability and validity of our experimental setup, we replicated the results of our experiments to investigate how each PSC layer could be modified to address the problems identified. During spin coating, it is noted that tape protection of the FTO anode contact has limitations, including incomplete surface coverage, uneven surface coating, reduced active area, and edge effects, resulting in lower PCE and performance. For large cells and commercial viability, this leads to scalability issues. Optimization of the spin coating parameters (spin speed, duration, solution concentration), and etching off a small area of FTO, will decrease the active area and allow an exposed area for a back contact. This can reduce the effects mentioned and achieve a more even surface thickness and uniform coverage. Titanium dioxide annealed at a high temperature of ~ 550 °C consumes high amounts of electrical energy during annealing. Consequently, device fabrication is limited to solid substrates with good thermal properties. By investigating and optimizing low-temperature annealing materials for ETL layers, such as SnO_2, we will be able to anneal onto flexible substrates like polyester (PET) and develop flexible PSCs allowing for a wide variety of applications.

The optimum annealing temperature time of the perovskite layer at 100 °C using the anti-solvent method was verified and the corresponding material properties were presented and discussed. The structural, morphological, optical, and performance properties of the Perovskite absorber and TiO_2 electron transport layers were systematically studied and presented.

The results show the formation of a highly crystalline tetrahedral structure for $CH_3NH_3PbI_3$ via a one-step method, a well-interconnected surface layer, significant light absorption and a bandgap of 2.06 eV. The anatase phase of TiO_2 was confirmed via FTIR at wavenumber 438 cm^{-1}. It had an average particle size of ~20 nm, uniform thin film coverage, optical transmission of ~ 70% and a bandgap of 3.52 eV. The PSC developed under the mentioned conditions achieved an open circuit voltage of 0.9057 V, short circuit current density of 12.2185 mA/cm^2, and PCE of 5.199%.

Perovskites are fabricated using toxic DMF solvents. Investigations into less toxic substitutes including N-methyl-2-pyrrolidone (NMP), ethyl acetate (EA) and DMSO, dimethyl propylene urea (DMPU) and 2-methyl tetrahydrofuran achieved promising results, although the drop in PCE indicates that solvent

engineering research is needed further. By looking at the effects of elemental doping on the ETL, absorber layer and HTL, fundamental properties of the ETL, absorber, and HTL layers can be improved. Through numerical analysis of SCAPS 1D improving fundamental PV properties can be achieved by including and optimizing the buffer layer between the ETL/Perovskite interface and the Perovskite/HTL interface.

Additionally incorporating a surfactant such as Triton X-100 into the ETL, absorber and HTL, can improve film quality, homogeneity, material properties and device performance. Adding small amounts of Triton X-100 surfactant to a triple cation mixed halide precursor solution improves film quality, surface coverage, wettability, crystallinity, and stability. The HTL precursor solution containing polyanile poly (styrenesulfonate) can also be improved by adding Triton X-100, which results in an alternative, less costly, and low-temperature HTL option that improves hole extraction, film quality, and PCE.

As a result of their cost-effective processability and stability in large production processes, carbon-based electrodes are attractive alternatives to thermal evaporation of back metal contacts at high temperatures. There are, however, issues related to poor interface contact and inferior performance between perovskite and carbon electrodes that need to be explored in greater detail. As flexible carbon electrodes, graphene, carbon nanotubes, and carbon black have shown excellent resistance to mechanical deformation. Carbon-based electrodes for PSCs continue to face the challenge of interface contact. The recommendations and results indicate that further research into material combination optimization, surfactant engineering, elemental doping, and process optimization is required to further improve the fundamental properties of each layer of the PSC and its overall performance and stability for commercialization.

ACKNOWLEDGEMENTS

The authors gratefully acknowledge the financial support from the South African National Research Foundation grant reference TTK200309508592.

REFERENCES

[1] R. L. Z. Hoye *et al.*, "Perovskite-inspired photovoltaic materials: toward best practices in materials characterization and calculations," *Chemistry of Materials*, vol. 29, no. 5, pp. 1964–1988, Mar. 2017, doi: 10.1021/acs.chemmater.6b03852.

[2] A. Farawar, "Perovskite solar cells : stability, design architecture, photophysical properties, and morphology of the film in organometal halide perovskite-based photovoltaics," no. November, p. 54, 2015, doi: 10.13140/RG.2.1.1406.8242.

[3] N.-G. Park, "Perovskite solar cells: an emerging photovoltaic technology," *Materials Today*, vol. 18, no. 2, pp. 65–72, Mar. 2015, doi: 10.1016/j.mattod.2014.07.007.

[4] I. Mesquita, L. Andrade, and A. Mendes, "Perovskite solar cells: materials, configurations and stability," *Renewable and Sustainable Energy Reviews*, vol. 82, pp. 2471–2489, Feb. 2018, doi: 10.1016/j.rser.2017.09.011.

[5] T. Ibn-Mohammed *et al.*, "Perovskite solar cells: An integrated hybrid lifecycle assessment and review in comparison with other photovoltaic technologies," *Renewable and Sustainable Energy Reviews*, vol. 80, pp. 1321–1344, Dec. 2017, doi: 10.1016/j.rser.2017.05.095.

[6] T.-B. Song *et al.*, "Perovskite solar cells: film formation and properties," *Journal of Materials Chemistry A*, vol. 3, no. 17, pp. 9032–9050, 2015, doi: 10.1039/C4TA05246C.

[7] J. S. Shaikh *et al.*, "Perovskite solar cells: In pursuit of efficiency and stability," *Materials & Design*, vol. 136, pp. 54–80, Dec. 2017, doi: 10.1016/j.matdes.2017.09.037.

[8] N. Ahn, D.-Y. Son, I.-H. Jang, S. M. Kang, M. Choi, and N.-G. Park, "Highly reproducible perovskite solar cells with average efficiency of 18.3% and best efficiency of 19.7% fabricated via lewis base adduct of lead(II) Iodide," *Journal of the American Chemical Society*, vol. 137, no. 27, pp. 8696–8699, Jul. 2015, doi: 10.1021/jacs.5b04930.

[9] J.-H. Im, H.-S. Kim, and N.-G. Park, "Morphology-photovoltaic property correlation in perovskite solar cells: One-step versus two-step deposition of CH3NH3PbI3," *APL MATERIALS*, vol. 2, no. 8, Aug. 2014, doi: 10.1063/1.4891275.

[10] M. Ozaki *et al.*, "How to make dense and flat perovskite layers for >20% efficient solar cells: Oriented, crystalline perovskite intermediates and their thermal conversion," *Bulletin of the Chemical Society of Japan*, vol. 92, no. 12, pp. 1972–1979, Dec. 2019, doi: 10.1246/bcsj.20190241.

[11] Peng *et al.*, "High-quality perovskite CH3NH3PbI3 thin films for solar cells prepared by single-source thermal evaporation combined with solvent treatment," *Materials*, vol. 12, no. 8, p. 1237, Apr. 2019, doi: 10.3390/ma12081237.

[12] M. I. Ahmed, Z. Hussain, M. Mujahid, A. N. Khan, S. S. Javaid, and A. Habib, "Low resistivity ZnO-GO electron transport layer based CH3NH3PbI3 solar cells," *AIP Advances*, vol. 6, no. 6, Jun. 2016, doi: 10.1063/1.4953397.

[13] H. J. Snaith *et al.*, "Anomalous hysteresis in perovskite solar cells," *The Journal of Physical Chemistry Letters*, vol. 5, no. 9, pp. 1511–1515, May 2014, doi: 10.1021/jz500113x.

[14] Q. Chen *et al.*, "Planar heterojunction perovskite solar cells via vapor-assisted solution process," *Journal of the American Chemical Society*, vol. 136, no. 2, pp. 622–625, Jan. 2014, doi: 10.1021/ja411509g.

[15] F. Hajipour *et al.*, "Developing a fluorescent hybrid nanobiosensor based on quantum dots and azoreductase enzyme formethyl red monitoring," *Iranian Biomedical Journal*, vol. 25, no. 1, pp. 8–20, Jan. 2021, doi: 10.29252/ibj.25.1.8.

[16] E. A. Al-Oubidy and F. J. Kadhim, "Photocatalytic activity of anatase titanium dioxide nanostructures prepared by reactive magnetron sputtering technique," *Optical and Quantum Electronics*, vol. 51, no. 1, p. 23, Jan. 2019, doi: 10.1007/s11082-018-1738-z.

[17] B. R. Sankapal, M. C. Lux-Steiner, and A. Ennaoui, "Synthesis and characterization of anatase-TiO2 thin films," *Applied Surface Science*, vol. 239, no. 2, pp. 165–170, Jan. 2005, doi: 10.1016/j.apsusc.2004.05.142.

[18] S. El-Sherbiny, F. Morsy, M. Samir, and O. A. Fouad, "Synthesis, characterization and application of TiO2 nanopowders as special paper coating pigment," *Applied Nanoscience*, vol. 4, no. 3, pp. 305–313, Mar. 2014, doi: 10.1007/s13204-013-0196-y.

[19] G. Gohari *et al.*, "Titanium dioxide nanoparticles (TiO2 NPs) promote growth and ameliorate salinity stress effects on essential oil profile and biochemical attributes of Dracocephalum moldavica," *Scientific Reports*, vol. 10, no. 1, p. 912, Jan. 2020, doi: 10.1038/s41598-020-57794-1.
[20] A. Sharma and N. B. Chaure, "Studies on CH3NH3PbI3 prepared by low-cost wet chemical technique," *Applied Physics A*, vol. 125, no. 11, p. 767, Nov. 2019, doi: 10.1007/s00339-019-3047-1.
[21] A. Mishra, Z. Ahmad, F. Touati, R. A. Shakoor, and M. K. Nazeeruddin, "One-dimensional facile growth of MAPbI 3 perovskite micro-rods," *RSC Advances*, vol. 9, no. 20, pp. 11589–11594, 2019, doi: 10.1039/C9RA00200F.
[22] Y. Bouachiba *et al.*, "TiO2 thin films studied by FTIR, AFM and spectroscopic ellipsometry," *International Journal of Nanoparticles*, vol. 6, no. 2/3, p. 169, 2013, doi: 10.1504/IJNP.2013.054992.
[23] W. Zhang *et al.*, "Solvent-induced textured structure and improved crystallinity for high performance perovskite solar cells," *Optical Materials Express*, vol. 7, no. 7, p. 2150, Jul. 2017, doi: 10.1364/OME.7.002150.
[24] Y. Yu *et al.*, "Ultrasmooth perovskite film via mixed anti-solvent strategy with improved efficiency," *ACS Applied Materials & Interfaces*, vol. 9, no. 4, pp. 3667–3676, Feb. 2017, doi: 10.1021/acsami.6b14270.
[25] S. Wang *et al.*, "Smooth perovskite thin films and efficient perovskite solar cells prepared by the hybrid deposition method," *Journal of Materials Chemistry A*, vol. 3, no. 28, pp. 14631–14641, 2015, doi: 10.1039/C5TA03593G.
[26] S. Casaluci *et al.*, "A simple approach for the fabrication of perovskite solar cells in air," *Journal of Power Sources*, vol. 297, pp. 504–510, Nov. 2015, doi: 10.1016/j.jpowsour.2015.08.010.
[27] M. Jaysankar *et al.*, "Minimizing voltage loss in wide-bandgap perovskites for tandem solar cells," *ACS Energy Letters*, vol. 4, no. 1, pp. 259–264, Jan. 2019, doi: 10.1021/acsenergylett.8b02179.

BIOGRAPHIES OF AUTHORS

Dwayne Jensen Reddy is a Lecturer in the Department of Electrical Power Engineering at the Durban University of Technology in Kwa–Zulu Natal, South Africa where he has been a faculty member since 2010. He joined the South African Technology Network PHD enhancement program in 2020. He completed his Master's in Engineering and undergraduate studies at the Durban University of Technology. His research interests lie in the area of renewable energy generation, ranging from development of energy generation devices, material fabrication and characterization, PV design and implementation. He is currently a Ph.D. candiate in Engineering at the Durban University of Technology. The provisional title of his research is 'The effects of Ion doping on the electron transfer layer of Perovskite solar cells'. He can be contacted at email: dwayner@dut.ac.za.

Prof. Ian Joseph Lazarus is an Associate Professor of Physics. He completed his Master's degree in Nuclear Physics and his doctoral degree focused on linear and nonlinear wave phenomena in electron-positron plasmas. He has a Diploma in Wind Energy Use (Sweden) and has completed courses in advanced renewable energy, advanced energy management, energy optimization and measurement and verification professional. He managers the Energy Technology Station, which focuses on research and innovation in energy and commercialization of energy related products. He also manages a number of community engagement and university projects in the energy field. He conducts research in Renewable Energy and Plasma Physics and supervises masters and doctoral students. His specific field of interest is in solar photovoltaics and solar thin-films, solar thermal, biogas, energy efficiency, figure and building energy. He can be contacted at email: lazarusi@dut.ac.za.

Effects of Zn Doped TiO_2 on the Performance of Perovskite Solar Cells

D. J. Reddy[1], I. J. Larzarus[2*]
[1]Faculty of Engineering and the Built Environment, Department of Electrical Power Engineering, Durban University of Technology, Durban, South Africa
[2]Faculty of Engineering and the Built Environment, Department of Physics, Durban University of Technology, Durban, South Africa
[*]corresponding author's email: lazarusi@dut.ac.za

Abstract – *The work focuses on the effects of Zn-doped TiO_2 as the Electron Transport Layer in MAPbI3 based Perovskite Solar Cells with a carbon-based back electrode fabricated under controlled ambient conditions. Varying molar percentages of Zn-doped TiO_2 of 0, 0.5, 1, 2, and 5 mol% were successfully incorporated into the TiO_2 crystal structure using the sol-gel technique. Characterization through X-ray diffraction and Energy Dispersive X-ray spectroscopy confirmed the incorporation of Zn ions. The crystallite size ranged from 19.99 to 7.1 nm, depending on the Zn ion doping concentration. Fourier Transform Infrared spectroscopy verified the presence of the anatase phase of Zn-doped TiO_2 at wavenumber 438 cm^{-1}. Scanning Electron Microscope images exhibited fairly smooth and uniform surface coverage for the Zn-doped TiO_2 layers. The Rq values for surface roughness showed a decrease from 26.85 nm for undoped TiO_2 to 23.4 nm for the 5 mol% Zn-doped TiO_2 layer. UV-Vis spectroscopy demonstrated low light transmission loss characteristics from 300 to 790 nm, with the 2 mol% Zn-doped TiO_2 showing slightly improved light transmission between 550 and 800 nm. The bandgap energy of undoped and Zn-doped TiO_2 ranged from 3.53 to 3.38 eV. An optimum power conversion efficiency of 5.67% was achieved with a 2 mol% dopant concentration. However, increasing the Zn dopant to 5 mol% led to a slight deterioration in the PCE. According to the optimized ETL processing for the PSC, the Jsc increased from 12.2185 mA/cm^2 to 12.25594 mA/cm^2, the Voc increased slightly from 0.90569 V to 0.9231 V, and the PCE from 5.199% to 5.67%.*

Keywords: *Conduction Band (CB), Perovskite Solar Cells (PSC), Power Conversion Efficiency (PCE), Titanium dioxide, Zn doped*

Article History
Received 18 January 2024
Received in revised form 17 April 2024
Accepted 26 April 2024

I. Introduction

Perovskite, which has the general crystal structure ABX_3, is the absorber component used in perovskite solar cells (PSCs). The perovskite form of ABX_3 with methyl ammonium (CH_3NH_3) as (A), metal such as lead (Pb) or tin (Sn) as (B), and a halide bromide (Br_3), iodide (I_3), or chloride (Cl_3) as (X_3) has so far been used to make the most effective PSC devices [1]. Perovskite has the following advantages: a low band gap that permits greater light absorption, a high carrier charge mobility that enables the generated electron and hole to move through the substance with little resistance, and a high diffusion length that inhibits electron-hole pair recombination [2].

Metal oxides such as zinc oxide (ZnO) [3], aluminum oxide (Al_2O_3) [4], tin oxide (SnO_2) [5], and titanium dioxide (TiO_2) have been used as the ETL to improve electron transportation and the PCE. TiO_2 exhibits attractive characteristics such as chemical stability, low cost, and high transport ability [6]. This is attributed to the conduction band (CB) of TiO_2 being lower than the conduction band of the perovskite absorber layer, facilitating the electron transport from the perovskite layer to the TiO_2 layer [6].

For the PSC to function effectively, the energy levels for each layer, as shown in Fig. 1, must be carefully aligned. This is accomplished by having the lowest unoccupied molecular orbital (LUMO) of the ETLs

slightly lower than that of the active layers, which provides an electron with a more desirable path to travel.

The same applies to the HTLs HOMO (highest occupied molecular orbital), which must be slightly higher than the active layers HOMO to offer a more attractive path for holes. This is similar for each layer in the cell; each layer must have either a greater HOMO or a lower LUMO in order for the charge carriers' transportation chain to function [7].

Materials are doped to increase charge carrier conductivity by adding an extra molecule to their structure. Doping changes the band structure and trap states of TiO_2, altering important properties such as conduction band energy, charge transport, recombination, and collection [8]. TiO_2 doped with Mg, Nb, Y, Al, and Zr has previously been used in perovskite solar cells. Mg-doped HBL/ ETL has improved V_{OC} because of its strong conduction band and low recombination [9]. Nb doping boosted electron injection and transport, resulting in greater JSC [10], and Y doping improved performance due to increased perovskite loading, resulting in significant increases in JSC and marginally reduced recombination [11]. It has been found that Al-doping reduces the number of oxygen vacancies and the associated deep trap states, lowering recombination and increasing film conductivity. As a result, J_{SC} increased overall [12]. Doping TiO_2 with Zr^{4+} reduced hysteresis while pushing the CB upward and reducing recombination, resulting in an increase in VOC [13, 14].

These results suggest that doping is important in lowering surface trap states, reducing hysteresis, and enhancing current density. Overall, these results suggest that TiO_2 doping and co-doping are expected to play an important role in lowering surface trap states, reducing hysteresis, enhancing current density, and improving PSC efficiencies. Doping causes the CB to shift, hence increasing charge transfer and decreasing recombination. Additionally, it has the ability to increase perovskite loading, lengthen device lifetimes, and play a vital role in reducing hysteresis [15].

Recent advancements in perovskite solar cell technology have highlighted the need for improved electron transport layers. This research focuses on the use of Zn-doped TiO_2 compact layer with variable doping concentrations of 0, 0.5, 1, 2 and 5 mol % as an electron transport layer. A number of n-i-p structure perovskite solar cells were developed. The Zn-doped TiO_2 compact layers' structural, morphological and optical properties are also analyzed and discussed. The photovoltaic properties of perovskite solar cells with various Zn-doped TiO_2 compact layers as electron transport layers are discussed. The research addresses the need to improve the electron compact layer, which will aid in developing future highly efficient perovskite solar cells using carbon-based electrodes.

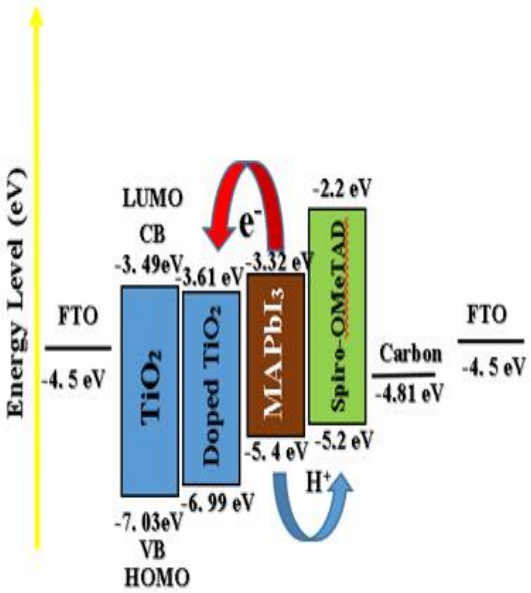

Fig. 1. Energy level band diagram

II. Materials

All chemicals used in the fabrication of the ETL, perovskite and HTL are listed in Table I and were purchased from Sigma-Aldrich Co.

TABLE I
LIST OF CHEMICALS

Layer	Chemicals
Electron Transport Layer Zn-doped TiO_2	Titanium isopropoxide (TTIP), ethanol (EtOH, super dehydrated,), hydrochloric acid (HCL), zinc chloride
Absorber Layer Perovskite	Methyl ammonium iodide (MAI, 99%), Lead (II) Iodide (PbI_2, 99.9%), dimethylformamide (DMF, super hydrated), dimethyl-sulfoxide (DMSO, super hydrated), di-ethyl Ether
Hole Transport Layer Spiro- OMeTAD	2, 2', 7, 7'-Tetrakis (N, N-di-p-methoxyphenylamino)-9, 9'-Spirobifluorene (Spiro- OMeTAD powder), 4- Tert – Butylpyridine (TBP, 96%), Bis (triflouromethane sulfonimide lithium salt (LiTFSI), chlorobenzene

III. Device Fabrication

A. Substrate Preparation

Fluorine-doped tin oxide (FTO) coated glass substrates of 25 mm x 25 mm with a thin film thickness of 100 nm and sheet resistance of 8.3 Ω were cleaned in a beaker containing detergent and deionized water. Each substrate was then rinsed in an acetone before being placed in the ultrasonic cleaner. The substrates were then immersed for 20 minutes at 80 °C in the ultrasonic cleaner containing ethanol. The substrates were removed and placed into a beaker containing deionized water before being placed on a hotplate at 60 °C for 10 minutes or until totally dry. The substrates were then placed for 20 minutes in an Ultra Violet Ozone (UVO) cleaner to break down organic surface impurities and provide an ultra-clean surface for the deposition of the ETL layer.

B. Zn – doped ETL layer preparation and deposition

In a volumetric flask, 40 ml di-ionized water was combined with 7.29 ml HCL and mixed for 3 minutes before adding additional de-ionized water up to 100 ml to obtain a 2M HCL stock solution. To prepare the 0.22 M TiO_2 precursor solution with Zn doping of 0.5, 1, 2, 5 mol%, the required amount of Zinc Chloride was added to 14.29 ml ethanol and stirred vigorously at 6000 rpm for 30 minutes, then 0.28 ml of the 2M HCL stock solution was slowly added and stirred vigorously at 6000 rpm for an additional 30 minutes, after which 1 ml of TTIP was slowly added and stirred for 2 hours. The resulting solution was then filtered using a 0.45 µm Teflon filter before spin coating to ensure the removal of small particles to obtain a smooth and uniform surface coverage. The FTO substrates were then pre-heated to 60 °C before dynamically spin coating 300 µl of the Zn-doped ELT precursor solution at 1000 rpm for 15 seconds and annealed on a ceramic digital hotplate at 550 °C for 30 minutes to form the Zn-doped ETL thin film layer. This layer was then UVO treated for 15 minutes prior to the deposition of the methyl ammonium lead iodide precursor solution.

C. Perovskite layer preparation and deposition

To prepare the perovskite precursor solution, 0.16 g of methyl ammonium iodide and 0.46 g of lead iodide were added to 0.08 ml of dimethyl sulfoxide (DMSO) and 0.6 ml of dimethylformamide (DMF) and magnetically stirred at 3000 rpm for 24 hours. Then 250 µl of the perovskite solution was statically spin-coated at 5000 rpm for 15 seconds, with 350 µl of di-ethyl ether slowly dripped from a distance of about 2 cm from the revolving substrate during the final 5 seconds. To develop the dark brown and semitransparent perovskite layer, the coated surface was placed on a digital hotplate at 65 °C for 1 minute, then slowly ramped up to 100 °C and annealed for 2 minutes. This was then placed in a vacuum desiccator for 3 hours before deposition of the hole transport layer to minimize exposure to oxygen and humidity.

D. HTL preparation and deposition

The hole transport layer was prepared by dissolving 0.52 g of LiTFSI in 1 ml acetonitrile and stirring vigorously for 10 minutes to form the LiTFSI stock solution. Then, 0.07 g of Spiro-OMeTAD powder was added to 1 ml chlorobenzene and stirred vigorously for 10 minutes to form the Spiro-OMeTAD solution. After this 0.03 ml of tBP and 0. 02 ml of the LiTFSI solution was added to the Spiro-OMeTAD solution and stirred for 30 minutes. Thereafter, 200 µl was dynamically spin-coated at 1000 rpm for 15 seconds and placed in a vacuum desiccator overnight before applying ~8 mg of activated carbon powder and FTO to form a metal-free back conductive electrode.

E. Synthesis Zn- doped TiO_2 nanoparticles

To synthesize the zinc-doped TiO_2 nanoparticles, the Zn-doped ETL precursor solution was aged for 72 days to form a clear and transparent gel. The gel was then dried for 12 hours at 80 °C in a hot air dryer to obtain dry TiO_2 powder. After drying, the TiO_2 powder is heated for 30 minutes at 550 °C in a furnace to produce anatase TiO_2 nanoparticles for FTIR, XRD, and TEM investigation.

IV. Characterization Equipment

The functional groups were identified using an Agilent Cary 630 ATR-FTIR with a diamond crystal operating between 400 and 4000 cm^{-1}. The X-ray diffractometer, type D8 Advanc, manufactured by M/s Bruker AXS, Germany was used to determine the Zn doped- TiO_2 crystal structure and orientation. The surface morphological qualities and elemental percentage concentration were determined using a Zeiss scanning electron microscope at 40 kV and 40 mA. The size of the particles was determined using a Transmission Electron Microscope and Image J software. The Agilent Cary 60 UV-Vis-NIR spectrometer was used to measure the optical characteristics. The photoluminescence intensity measurements were carried out using the Perkin Elmer Lambda 35 UV/ Vis spectrometer. The TAUC plot with a direct bandgap power factor was used to calculate bandgaps. The photovoltaic characteristics were measured using a Keithley 2460 source measurement instrument and an AM 1.5 (1000 W/ m^2) LED light source.

V. Results and Discussion

A. X-Ray Diffraction

For nanoparticles, XRD is typically employed to identify the crystal phase structure and estimate crystallite size and crystallinity [16]-[17]. The XRD diffraction patterns of zinc-doped titanium dioxide powder samples are shown in Fig. 2. Fig. 2 shows the XRD patterns of Zn-TiO_2 powder samples doped with 0.5%, 1%, 2%, and 5% Zn. The XRD peaks at 2θ = 25.1° (101), 37.8° (004), 47.1° (200), 53.4° (105), 54.5° (211), and 61.8° (204) are typically characterized as the typical diffraction peaks of the anatase crystal phase of tetragonal titanium dioxide structure (JCPDS No. 21-1272) with excellent surface performance[18]. All Zn-TiO_2 samples show a pure anatase phase with no rutile phase or zinc ions. Due to the low Zn content, no additional diffraction peaks associated to ZnO develop even at the greatest Zn dopant concentration (5 mol %).

Fig. 3 shows the EDX spectroscopy confirming the weight percentage composition of Zn-doped TiO_2. Furthermore, Fig 2 shows that the sample doped with 0.5 % Zn was largely amorphous, and the half-width of the peak (101) plane increases slightly as the doped Zn amount increases, indicating that the degree of crystallinity of samples as well as crystallite size decreases while the surface defect content increases. This could be attributed to the slight inhibition of TiO_2 crystal formation by Zn doping during the heat treatment process [19]. Furthermore, the peak intensity of the (101) plane increases with increasing Zn doping up to 5 %, which can be attributed to the influence of Zn^{2+} into the TiO_2 lattice structure, as previously found by Arunachalam et al. [20]. Additionally, with Zn ion insertion, XRD patterns exhibited a slight shift to lower angles because the ionic radius of Zn^{2+} (i.e., 0.074 nm) is greater than that of Ti^{4+} (i.e., 0.061 nm). It suggests that Zn^{2+} may enter the TiO_2 lattice or interstitial site [21]. The phase composition of Zn-doped TiO_2 films is shown to be dependent on dopant concentration. The crystallite size (D) for the samples containing 1%, 2%, and 5% Zn was approximately 12.7, 10.8, and 7.1 nm, respectively, as determined by the Debye Scherrer's formula in (1) [22] from the half width (β) of the peak at 2θ = 25.1°.

$$D = k\lambda / (\beta \cos\theta) \quad (1)$$

where k is the shape factor (0.9), D is the average crystallite size, β is the half-width of the measured diffraction peak, θ is the diffraction angle, and λ is the X-ray wavelength (0.154 nm).

B. Fourier Transform Infrared

The FTIR measurement of undoped and Zn doped TiO_2 nanoparticles calcined at 550° C was performed using an Agilent Cary 60. The absence of O-H hydroxyl groups in the wavenumber range 3100-3600 cm^{-1} presented in Fig. 4 can be explained by the high calcination temperature of 550 °C and the elimination of hydroxyl groups. The interactions of the hydroxyl groups with the NH_4 and CH_3 in the perovskite could reduce the performance of the PSC, resulting in the breakdown of $CH_3NH_3PbI_3$ into PbI_2 and CH_3NH_3I [23]. Sharp peaks related to O-Ti-O bonding between 528 and 408 cm^{-1} indicate that the thin layer is crystalline. The prominent peak at 438 cm^{-1} is typical of Zn doped- TiO_2 anatase phase nanoparticles [19]-[25].

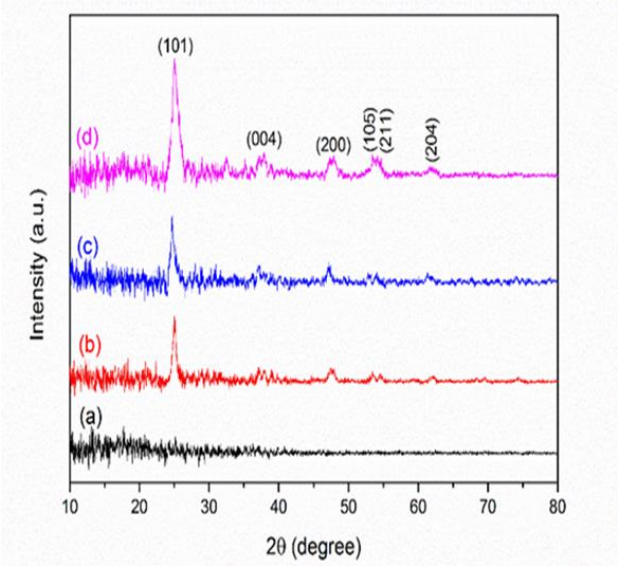

Fig. 2. XRD patterns of Zn-TiO_2 powder samples doped with (a) 0.5%, (b) 1%, (c) 2%, and (d) 5%

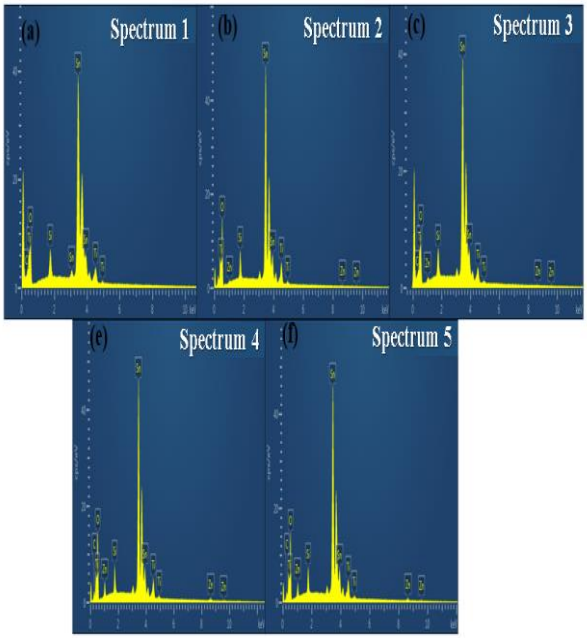

Fig. 3. Elemental weight percentage compositions of (a) undoped TiO_2 (b) 0.5 mol% (c) 1 mol% (d) 2 mol% (e) 5 mol%

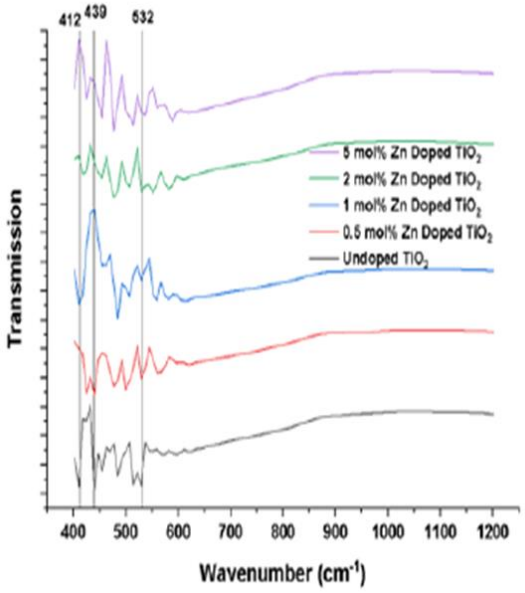

Fig. 4. FTIR results of planar Zn doped TiO_2 nano particles annealed at 550 °C

C. Scanning Electron Microscope

SEM was used to examine the morphology of the TiO_2 and Zn-doped TiO_2 nanoparticles after annealing at 550° C for 30 minutes. The top view of the SEM images of the TiO_2 and Zn-doped TiO_2 layers is shown in Fig. 5. Fig. 5(a) shows a porous and fairly uniform surface covering with no discernible pinholes created on the surface for the undoped TiO_2 sample. The Zn-doped TiO_2 nanoparticles on the surface exhibit an irregular morphology and a conical shape as shown if Fig. 5(b)-(e). According to the SEM images, TiO_2 nanoparticle instability results in agglomeration, which causes the particles to bond. The aggregation of the nanoparticles is further illustrated by the SEM images showing the formation of clusters which appears to reduce upon increasing Zn doping concentration. This could also be attributed to the decrease in crystallite size upon increasing Zn doping observed by the XRD characterization. The surface profiles and Root Mean Square (Rq) values shown in Fig. 6 indicates the surface roughness values of the samples. Fig. 6(a) shows the highest surface roughness of 26.85 nm for the undoped TiO_2 sample and lowest surface roughness of 23.4 nm for the 5 mol% Zn doped TiO_2 layer is shown Fig. 6(e).

It can be seen in Fig. 6(f) that the surface roughness rate decreased gradually from 26.85 to 23.4 nm with increasing Zn doping concentration from 0 to 5 mol %. The reason for the decrease in surface roughness and smoother surfaces could be due to less aggregation due to the dispersion of TiO_2 upon Zn doping [26]-[28]. The surface smoothness of Zn doped TiO_2 compact layer has a critical role in the electron transport behaviour by providing an improved surface interface for the deposition and annealing of the perovskite layer which is critical for improving the performance of PSC [29].

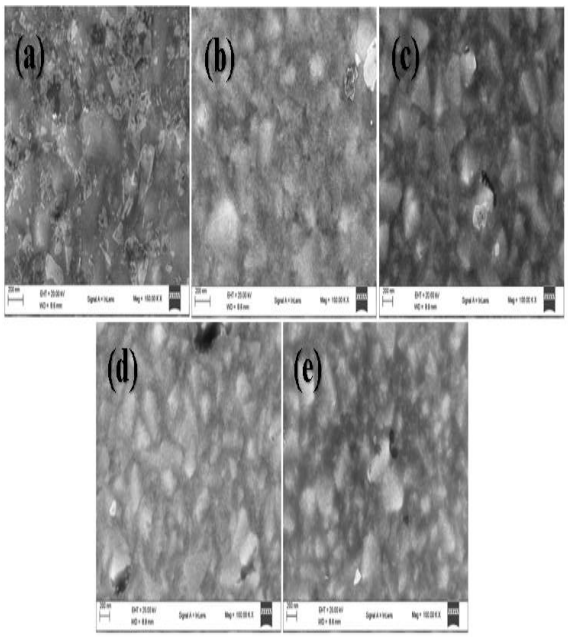

Fig. 5. SEM images of the (a) undoped TiO_2 (b) 0.5 mol% Zn (c) 1 mol% (d) 2 mol% (e) 5 mol%

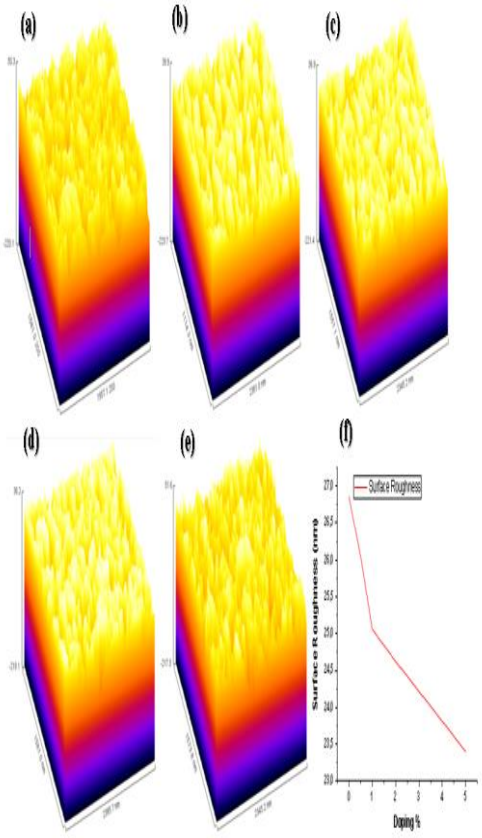

Fig. 6. Surface roughness of (a) undoped TiO_2 (b) 0.5 mol% (c) 1 mol% (d) 2 mol% (e) 5 mol% (f) surface roughness vs doping %

D. Transmission Electron Microscope

The synthesized nano particles size and shape was further investigated by TEM and are shown in Fig. 7 which shows the morphology and size distribution of the TiO_2 nanoparticles ranging from 15 to 20 nm. The Zn doped TiO_2 exhibits a homogenous spherical morphology. The TEM results show an increase in the particle size from 15.91 nm for undoped TiO_2 to 20.31 nm for 5 mol % Zn doped TiO_2, this could be attributed to the incorporation of Zn ions into the TiO_2 lattice structure [30]-[31]. The larger particle size reduces the bandgap and recombination sites in the ETL layer as the space between the valence and conduction bands narrows and electron – hole pairs are further apart and effect of the coulomb interaction between them is reduced [32]-[33]. This is confirmed by the TAUC plot in Fig. 8, which shows bandgap narrowing as the particle size increases from 0 to 5 mol % Zn doping.

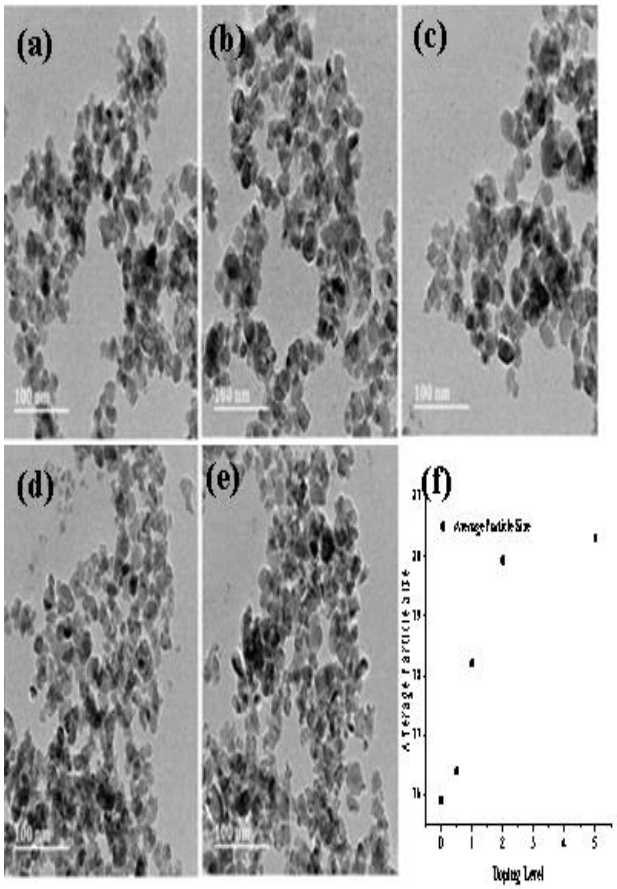

Fig. 7. TEM images of (a) undoped TiO_2 (b) 0.5 mol% (c) 1 mol% (d) 2 mol% (e) 5 mol% (f) average particle size vs doping %

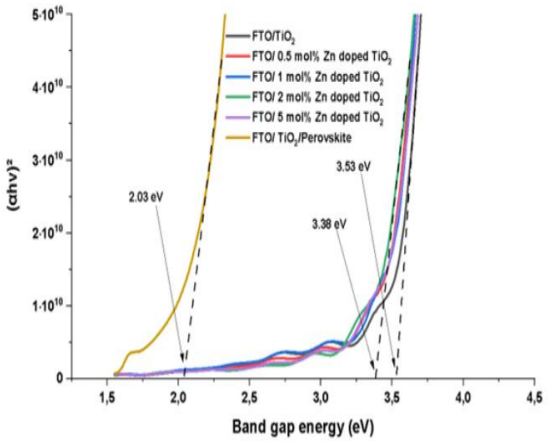

Fig. 8 Tauc Plot

E. Energy Dispersive X-Ray

Energy dispersive X ray spectrometry analysis of TiO_2 thin films was performed using a Zeiss scanning electron microscope to determine and identify the elemental composition and concentrations of the FTO\Zn-TiO_2 layers and is shown below in Table II. It can be seen that the wt % of Zn increases from 0 to 1.08 as the molar percentage concentration increases from 0 to 5 mol %.

Fig. 3 (a)-(e) previously shows peaks for Ti, O, Zn, Sn and Si. The spectra include small peaks of carbon which may be due to the carbon tape fixed on the SEM stub during characterization, no other impurities are seen. Overall, the EDX spectra indicates crystalline synthesis of Zn doped TiO_2 nanoparticles.

TABLE II
ELEMENTAL COMPOSITION AND CONCENTRATIONS OF THE FTO\ ZN- TiO2 LAYERS

Sample	C	O	Si	Ti	Zn	Sn
Spectrum 1 Undoped TiO_2	0	27.2	2.75	3.05	0	66.9
Spectrum 2 0.5 mol%-Zn Doped TiO_2	2.11	29.1	2.33	3.95	0.29	62.3
Spectrum 3 1 mol%-Zn Doped TiO_2	2.56	27.1	2.50	3.85	0.38	63.5
Spectrum 4 2 mol%-Zn Doped TiO_2	2.02	27.9	2.79	3.82	0.49	62.9
Spectrum 5 5 mol%-Zn Doped TiO_2	1.74	28.8	2.22	3.24	1.08	62.8

F. UV-Vis Spectroscopy

The Cary 60 UV-Vis was used to collect UV-Vis transmission and absorption spectra. The UV-Vis transmission spectra of various TiO_2 and Zn-doped TiO_2 thin films coated on FTO substrates are shown in Fig. 9. The transmission intensity of the Zn doped TiO_2 thin film samples decreased between 380 and 550 nm when compared to the undoped TiO_2 sample; between 550 and 800 nm a slight increase is observed for the 2 mol % Zn doped sample, either than that, there is no discernible variation in transmission intensity. The transmission spectra of between 65 – 70 % over this region show a slight light loss when compared to the transmittance of the FTO substrate of between 70 – 80 %. The slight increase in optical transmission exhibited by the 2 mol % Zn doped TiO_2 could be due to a decrease in surface roughness by the incorporation of Zn ion into the TiO_2 lattice structure [34]-[35], this slight improvement in optical transmission will directly increase the light absorption of the perovskite film.

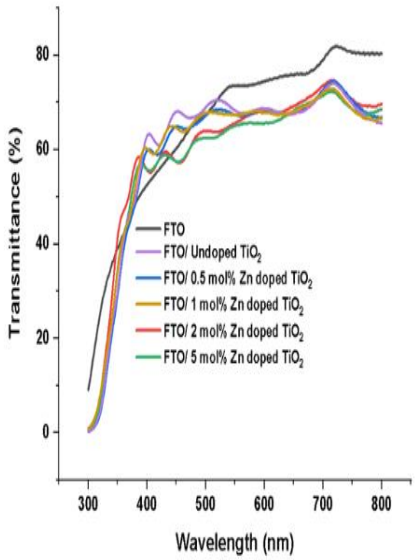

Fig. 9. Transmission spectra of undoped and Zn-doped TiO_2

The absorption spectra of TiO_2 and Zn-doped TiO_2 samples are shown in Fig 10, as can be seen from the results there is a clear improvement in the optical absorption from a range of 300 nm to 790 nm with the introduction of Zn ions into TiO_2, this also has a direct influence on the bandgap of the TiO_2 and the Zn doped TiO_2 layers and is shown in Fig. 8 utilizing the TAUC plot.

The band gap of the undoped TiO_2, Zn doped TiO_2, and the perovskite layer was determined by plotting $(a/hv)^2$ as a function of photon energy and extrapolating the linear region of the absorption curve as shown in Fig. 8. The bandgap of the perovskite layer was determined to be 2.03 eV. The bandgaps of undoped TiO_2 and 0.5, 1, 2, 5 mol % Zn doped TiO_2 are respectively 3.53, 3.48, 3.45, 3.38, and 3.41 eV. As the mol% Zn doping concentration increased from 0 % to 5 %, the band gap gradually decreased from 3.53 eV for the undoped TiO_2 down to 3.38 eV for 2 mol%, then increased by 0.03 eV for the 5 mol% when compared to 2 mol%. By increasing Zn doping concentration, the band gap of Zn-doped TiO_2 compact layers decreased and introduced a new band in the TiO_2 bandgap. Previous results indicate that bandgap narrowing can shift the Fermi energy level up and lower the position of the conduction band, which can improve electron injection from the perovskite layer to the Zn-doped TiO_2 compact layer [36].

G. Photoluminescence

To gain insight into the charge transfer kinetics within the TiO_2 and Zn-doped TiO_2 thin films, photoluminescence intensity measurements recorded at room temperature (300 K) was done using the Perkin Elmer Lambda 35 UV/Vis spectrometer at an excitation wavelength of 525 nm.

The excitation wavelength of 525 nm produced a photoluminescence peak at 735 nm (1.69 eV) corresponding closely to the bandgap of the perovskite film. The peak position is slightly lower (0.37 eV) than the bandgap value (2.06 eV) estimated from the Tauc plot but relatively close to the bandgap value of 1.6 eV reported by Kong et al for the tetragonal structure of $CH_3NH_3PbI_3$ [37].

According to the corresponding shape on the PL spectra for the undoped and doped TiO_2 films, Zn doping does not introduce additional PL signals. The broad photoluminescence peak observed at 735 nm is a result of the radiative recombination of electrons and holes near the band edges [38]. This depicts the direct bandgap nature of the $CH_3NH_3PbI_3$ film.

In materials with a direct bandgap, the recombination of charge carriers leads to the emission of photons and in this case, it occurs at 735 nm. Additionally, Fig. 10 shows a decrease in PL intensity from the undoped TiO_2 to the Zn doped TiO_2, with 2 mol% and 5 mol% Zn doped TiO_2 showing the strongest PL quenching indicating electrons can be effectively transferred to the perovskite layer to TiO_2 thus resulting in faster charge transfer kinetics and less recombination. The low emission intensities of the Zn-doped TiO_2 films confirm that Zn doping can reduce electron-hole recombination reactions.

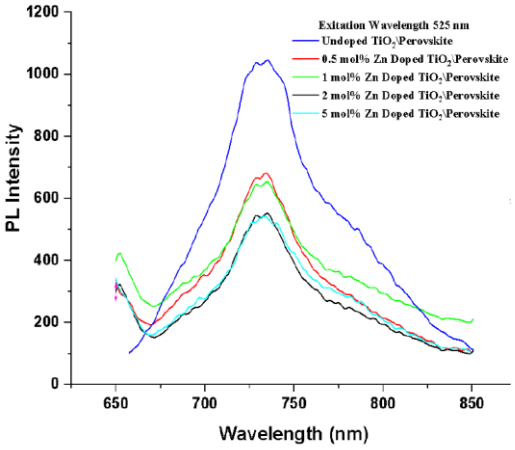

Fig. 10. Photoluminescence spectra of undoped and Zn doped TiO_2

H. PSC Performance

The J-V curves and best performance of the various PSCs developed are shown in Fig. 11. The open circuit voltage slightly improved from 0.90569 V to 0.92774 V when the Zn doping concentration increased from 0 up to 2 mol%, possibly due to the lower conduction band position. Adding Zn ions into the TiO_2 lattice structure raises the CB toward the absorber's LUMO level and enables electron injection from the absorber into the compact layer. When compared to undoped TiO_2, the lower conduction band of Zn-doped TiO_2 improves electron injection from the perovskite to the ETL layer and electron transport rate. Due to bandgap narrowing and improved charge transport, the J_{SC} increased from 12.21851 mA/ cm^2 to 12.25594 mA/cm^2 when Zn doping concentration increased from 0 to 2 mol%.

The PCE of the perovskite solar cell with undoped TiO_2 has a PCE of 5.199 %. As Zn doping concentrations were increased to 2 mol%, the PCE increased to 5.675 % and FF from 48.05 to 49.4823. The PSC with 5 mol% Zn doped TiO_2 has a slightly lower V_{OC}, J_{SC}, FF and PCE. The PCE decreased slightly to 5.5648% compared to 2 mol% Zn-doped TiO_2. A possible reason for the reduction in the efficiency of cells with a doping level of 5 mol% is that this doping level moves the CB of the ETL by ~0.03 eV upward. The electron injection from the absorber layer toward the ETL may be made easier by the proximity of the CB of the ETL to the LUMO of the absorber layer. When the CB goes higher, it moves away from the CB of the FTO layer. As a result, it would raise the recombination rate within the ETL while decreasing electron injection from the CB of the ETL to the CB of the FTO layer [39]. Additionally, the efficiencies are lower than reported values because the PSC performance could have been affected by the humidity under the ambient conditions of fabrication and characterization including the instability of the single cation of perovskite $CH_3NH_3PbI_3$.

Doping (%)	Voc (V)	Jsc (mA/cm²)	FF (%)	PCE (%)
0	0.90569	12.21851	48.0502	5.199
0.5	0.90981	12.22852	48.4989	5.3266
1	0.91082	12.23811	48.7714	5.4364
2	0.92774	12.25594	49.4823	5.675
5	0.9231	12.2387	49.226	5.5648

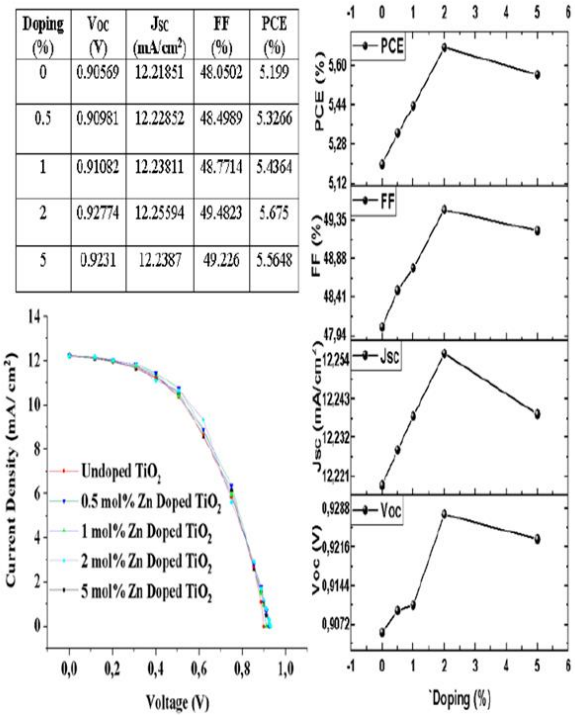

Fig. 11. PV characteristics of Zn-TiO_2 PSC's

VI. Conclusion

Finally, using the sol-gel technique followed by thermal annealing, several Zn-doped TiO_2 compact layers with variable Zn doping concentrations are successfully produced. The impact of Zn doping concentration on changes in structural, morphological, optical, and performance photovoltaic properties was studied systemically. The data indicates an improvement in surface smoothness, particle morphology, and optical properties and induces band gap narrowing. This correspondingly improves the bandgap alignment with the perovskite absorber layer and the PCE. With a Zn doping concentration of 2 mol%, the structural, morphological, optical, and performance properties are optimum. The *Jsc* of perovskite solar cells increased from 12.2185 mA/cm^2 to 12.25594 mA/cm^2, V_{OC} decreased from 0.90569 to 0.92774 V and the PCE increased from 5.199 % to 5.675 %. Importantly, the Zn-doped TiO_2 PSCs developed under the mentioned controlled conditions allow for reasonable reproducibility and reliability without using an expensive glovebox and thermal evaporation equipment for the back metal contacts.

Further study to investigate the influence of process conditions on the structure of TiO_2 is a good starting point to further improve TiO_2 at an ETL in PSC's.

understanding how defects in the materials are created during fabrication is vital, as this significantly affects the material's properties. Synthesized anatase phase TiO_2 nanoparticles at 550 ℃ consume high electrical energy during annealing and limit device fabrication to solid substrates. Investigation and optimization into low temperature annealing for TiO_2 will allow annealing onto more flexible substrates such as Polyethylene (PET) and provide a way to develop flexible PSC, allowing for numerous applications. Annealing the TiO_2 thin films at varying temperatures and studying their influence on crystallinity, trap states, conduction band position, elemental composition, and recombination will allow linking of annealing temperature, material composition, and device performance.

Acknowledgments

The authors gratefully acknowledge the financial support from the South African National Research Foundation grant reference TTK200309508592.

Declaration on Conflict of Interest

The authors have no conflict of interest in the publication process of the research article.

Statement on Author contributions

D. J. Reddy's contributions included conception, device fabrication, data collection, analysis and interpretation. I. J. Lazarus's contributions included drafting of the article, critical revision of the article and final approval of the version to be submitted.

References

[1] I. Mesquita, L. Andrade, and A. Mendes, "Perovskite solar cells: Materials, configurations and stability," Renewable and Sustainable Energy Reviews, vol. 82, pp. 2471–2489, Feb. 2018, doi: 10.1016/j.rser.2017.09.011.

[2] J. Bisquert, The Physics of Solar Cells: Perovskites, Organics, and Photovoltaic Fundamentals, 1st ed. Boca Raton, FL : CRC Press, Taylor & Francis Group, [2018]: CRC Press, 2017. doi: 10.1201/b22380.

[3] A. K. Chandiran, M. Abdi-Jalebi, M. Nazeeruddin, and M. Graetzel, "Analysis of Electron Transfer Properties of ZnO and TiO_2 Photoanodes for Dye-Sensitized Solar Cells," *ACS nano*, vol. 8, Feb. 2014, doi: 10.1021/nn405535j.

[4] Y.-N. Zhang, B. Li, L.-Y. Zhang, and L.-W. Yin, "Efficient electron transfer layer based on Al_2O_3 passivated TiO_2 nanorod arrays for high performance evaporation-route deposited $FAPbI_3$ perovskite solar cells," *Solar Energy Materials and Solar Cells*, vol. 170, pp. 187–196, Oct. 2017, doi: 10.1016/j.solmat.2017.05.072.

[5] Z. Cao *et al.*, "Metal Oxides Alternatives for Efficient Electron Transport in Perovskite Solar Cells: Beyond TiO_2 and SnO_2," *Journal of Materials Chemistry A*, vol. 8, Aug. 2020, doi: 10.1039/D0TA07282F.

[6] T. Kim, J. Lim, and S. Song, "Recent Progress and Challenges of Electron Transport Layers in Organic–Inorganic Perovskite Solar Cells," Energies, vol. 13, no. 21, p. 5572, Oct. 2020, doi: 10.3390/en13215572.

[7] N. Marinova, S. Valero and J. L. Delgado, "Organic and perovskite solar cells: Working principles, materials and interfaces," *Journal of Colloid and Interface Science*, vol. 488, pp. 373-389, November 2016.

[8] B. Roose, S. Phathak and U. Steiner, "Doping of TiO_2 for sensitized solar cells," *Royal Society of Chemistry*, 28 April 2015.

[9] J. Wang, M. Qin, H. Tao, W. Ke, Z. Chen, J. Wan, P. Qin, L. Xiong, H. Lei, H. Yu and G. Fang, "Performance enhancement of perovskite solar cells with Mg-doped TiO_2 compact film as the hole-blocking layer," Applied Physics Letters, vol. 106, no. 12, p. 121104, 2015.

[10] G. Yin, J. Ma, H. Jiang, J. Li, D. Yang, F. Gao, H. J. Zeng, Z. Lui and S. Liu, "Enhancing Efficiency and Stability of Perovskite Solar Cells through Nb-Doping of TiO_2 at Low Temperature," *ACS Applied Materials & Interfaces*, vol. 9, 2017.

[11] X. Deng, Y. Wang, Z. Cui, L. Li, and C. Shi, "Y-doping TiO_2 nanorod arrays for efficient perovskite solar cells," *Superlattices and Microstructures*, vol. 117, pp. 283–287, May 2018, doi: 10.1016/j.spmi.2018.03.051.

[12] S. K. Pathak, A. Abate, P. Ruckdeschel, B. Roose, K. C. Godel, Y. Vaynzof, A. Santhala, S.-I. Wantanabe, D. J. Hollman, N. Noel, A. Sepe, U. Weisner, R. Friend, H. J. Snaith and U. Steiner, "Performance and Stability Enhancement of Dye-Sensitized and Perovskite Solar Cells by Al Doping of TiO_2," *Advanced Functional Materials*, vol. 24, no. 38, pp. 6046-6055, 2014.

[13] H. Nagaoka, F. Ma, D. W. deQuilettes, S. M. Vorpahl, M. S. Glaz, A. E. Colbert, M. E. Ziffer and D. S. Ginger, "Zr Incorporation into TiO_2 Electrodes Reduces Hysteresis and Improves Performance in Hybrid Perovskite Solar Cells while Increasing Carrier Lifetimes," Journal of Physical Chemistry Letters, vol. 6, no. 4, pp. 669-675, 2015.

[14] N. H et al., "Zr Incorporation into TiO_2 Electrodes Reduces Hysteresis and Improves Performance in Hybrid Perovskite Solar Cells while Increasing Carrier Lifetimes.," J Phys Chem Lett, vol. 6, no. 4, pp. 669–675, Feb. 2015, doi: 10.1021/jz502694g.

[15] D.-Y. Son et al., "Universal Approach toward Hysteresis-Free Perovskite Solar Cell via Defect Engineering," J. Am. Chem. Soc., vol. 140, no. 4, pp. 1358–1364, Jan. 2018, doi: 10.1021/jacs.7b10430.

[16] Roshanghias, A., G. Sodeifian, A.A. Javidparvar, and S. Tarashi, "Construction of a novel polytetrafluoroethylene-based sealant paste: The effect of polyvinyl butyral (PVB) and nano-alumina on the sealing performance and construction formulations", *Results in Engineering 14*, 2022, pp. 100460.

[17] Bunaciu, A.A., E. Gabriela Udriştioiu, and H.Y. Aboul-Enein, "X-Ray Diffraction: Instrumentation and Applications", *Critical Reviews in Analytical Chemistry 45*(4), 2015, pp. 289–299.

[18] Aware, D. V., and S.S. Jadhav, "Synthesis, characterization and photocatalytic applications of Zn-doped TiO_2 nanoparticles by sol–gel method", Applied *Nanoscience 6*(7), 2016, pp. 965–972.

[19] Chauhan, R., A. Kumar, and R.P. Chaudhary, "Structural and optical characterization of Zn doped TiO_2 nanoparticles prepared by sol–gel method", *Journal of Sol-Gel Science and Technology 61*(3), 2012, pp. 585–591.

[20] Arunachalam, A., S. Dhanapandian, C. Manoharan, and G. Sivakumar, "Physical properties of Zn doped TiO_2 thin films with spray pyrolysis technique and its effects in antibacterial activity", *Spectrochimica Acta Part A: Molecular and Biomolecular Spectroscopy 138*, 2015, pp. 105–112.

[21] Ghanbari Niaki, A.H., A.M. Bakhshayesh, and M.R. Mohammadi, "Double-layer dye-sensitized solar cells based on Zn-doped TiO_2 transparent and light scattering layers: Improving electron injection and light scattering effect", *Solar Energy 103*, 2014, pp. 210–222.

[22] Hajipour, F., S. Asad, M.A. Amoozegar, et al., "Developing a fluorescent hybrid nanobiosensor based on quantum dots and azoreductase enzyme formethyl red monitoring", *Iranian Biomedical Journal 25*(1), 2021.

[23] M. Shirayama et al., "Degradation mechanism of $CH_3NH_3PbI_3$ perovskite materials upon exposure to humid air," Journal of

Applied Physics, vol. 119, no. 11, p. 115501, Mar. 2016, doi: 10.1063/1.4943638.
[24]E. Al-Oubidy and F. Kadhim, "Photocatalytic activity of anatase titanium dioxide nanostructures prepared by reactive magnetron sputtering technique," Optical and Quantum Electronics, vol. 51, Jan. 2019, doi: 10.1007/s11082-018-1738-z.
[25]"Titanium dioxide (anatase)." https://webbook.nist.gov/cgi/cbook. (Accessed Sep. 06, 2022).
[26]A. M. Alturki, Department of Chemistry, Faculty of Science, University of Tabuk, Saudi Arabia;, R. Ayad, and Department of Physics, Faculty of Science, University of Tabuk, Saudi Arabia;, "Synthesis and Characterization of Titanium Dioxide Nanoparticles with a Dosimetry Study of their Ability to Enhance Radiation Therapy using a Low Energy X-ray Source," Indian Journal of Science and Technology, vol. 12, no. 9, pp. 1–5, Mar. 2019, doi: 10.17485/ijst/2019/v12i9/140977.
[27]S. Myat, T. Htay, S. N. Khine and K. P. P. Tun, "XRD and SEM Analysis, and Semiconductor Type Determination of TiO_2 for Dye-sensitized Solar Cell," vol. 4, no. 2.
[28]Yu *et al.*, "Ultrasmooth Perovskite Film via Mixed Anti-Solvent Strategy with Improved Efficiency," *ACS Appl. Mater. Interfaces*, p. 11, 2017.
[29]M. K. Tariq et al., "Comparative study of Ag, Sn or Zn doped TiO_2 thin films for photocatalytic degradation of methylene blue and methyl orange," Mater. Res. Express, vol. 6, no. 10, p. 106435, Sep. 2019, doi: 10.1088/2053-1591/ab3efd.
[30]R. S. Dubey, S. R. Jadkar, and A. B. Bhorde, "Synthesis and Characterization of Various Doped TiO_2 Nanocrystals for Dye-Sensitized Solar Cells," ACS Omega, vol. 6, no. 5, pp. 3470–3482, Feb. 2021, doi: 10.1021/acsomega.0c01614.
[31]M. M. Karkare, "Estimation of band gap and particle size of TiO_2 nanoparticle synthesized using sol-gel technique," in 2014 International Conference on Advances in Communication and Computing Technologies (ICACACT 2014), Aug. 2014, pp. 1–5. doi: 10.1109/EIC.2015.7230747.
[32]T. Moore and B. Bartlett, "Lowering the Band Gap of Anatase-Structured TiO_2 by Coalloying with Nb and N: Electronic Structure and Photocatalytic Degradation of Methylene Blue Dye," The Journal of Physical Chemistry C, vol. 116, pp. 5986–5994, Feb. 2012, doi: 10.1021/jp2078456.
[33]X. Liu, Z. Wu, Y. Zhang, and C. Tsamis, "Low temperature Zn-doped TiO_2 as electron transport layer for 19% efficient planar perovskite solar cells," Applied Surface Science, vol. 471, pp. 28–35, Mar. 2019, doi: 10.1016/j.apsusc.2018.11.237.
[34]M. I. Khan *et al.*, "300 keV cobalt ions irradiations effect on the structural, morphological, optical and photovolatic properties of Zn doped TiO_2 thin films based dye-sensitized solar cells," *Ceramics International*, vol. 46, Mar. 2020, doi: 10.1016/j.ceramint.2020.03.256.
[35]B. Ünlü, S. Çakar, and M. Özacar, "The effects of metal-doped TiO_2 and dithizone-metal complexes on DSSCs performance," *Solar Energy*, vol. 166, pp. 441–449, May 2018, doi: 10.1016/j.solener.2018.03.064.
[36]Xiaotao Liu, Zhenhua Wu, Yiqiang Zhang, and Christos Tsamis. Low temperature zn-doped TiO_2 as electron transport layer for 19% efficient planar perovskite solar cells. Applied Surface Science, 471:28–35, 2019.
[37]Weiguang Kong, Zhenyu Ye, Zhen Qi, Bingpo Zhang, Miao Wang, Arash Rahimi-Iman, and Huizhen Wu. Characterization of an abnormal photoluminescence behavior upon crystal-phase transition of perovskite $CH_3NH_3PbI_3$. Physical Chemistry Chemical Physics, 17(25):16405–16411, 2015.
[38]Yasuhiro Yamada, Toru Nakamura, Masaru Endo, Atsushi Wakamiya, and Yoshihiko Kanemitsu. Near-band-edge optical responses of solution-processed organic–inorganic hybrid perovskite ch3nh3pbi3 on mesoporous tio2 electrodes. Applied Physics Express, 7(3):032302, 2014.
[39]A. Baktash, O. Amiri, and A. Sasani, "Improve efficiency of perovskite solar cells by using Magnesium doped ZnO and TiO_2 compact layers," *Superlattices and Microstructures*, vol. 93, pp. 128–137, May 2016, doi: 10.1016/j.spmi.2016.01.026.